Dynamical multi-configuration generalized coherent states approach to many-body bosonic quantum systems

Dissertation

zur Erlangung des wissenschaftlichen Grades
Doctor rerum naturalium

vorgelegt von

Yulong Qiao

geboren am 01.08.1994 in Linyi, China

Institut für Theoretische Physik
Fakultät für Physik
Bereich Mathematik und Naturwissenschaften
Technische Universität Dresden

2024

Eingereicht am 26.01.2024

1. Gutachter: Prof. Dr. Frank Grossmann
2. Gutachter: Prof. Dr. Steven Tomsovic

Abstract

This doctoral thesis presents an extensive study on the applications of generalized coherent states (GCS) for the quantum dynamics of many-body systems. The research starts with exploring the fundamental properties of generalized coherent states, which are created by generators of the SU(M) group acting on an extreme state, and demonstrating their role in representing ideal quantum condensates. A significant feature is the relationship between generalized coherent states and the more standard Glauber coherent states (CS). Similarities in their overcomplete and non-orthogonal nature are shown, alongside crucial differences with respect to $U(1)$ symmetry and entanglement properties, which generalized coherent states solely adhere to.

Furthermore, this thesis delves into the nonequilibrium dynamics of GCS as well as Glauber CS under nonlinear interactions. Combining analytical analysis and numerical calculations, it is found that while their two-point correlation functions are equivalent in the thermodynamic limit, their autocorrelation functions exhibit distinctly different characteristics. It is proven analytically that the autocorrelation functions of the evolved GCS relate to the ones of the corresponding Glauber CS through a Fourier series relation, which arises due to the $U(1)$ symmetry of the GCS.

A substantial part of this thesis is dedicated to investigating the dynamics of the Bose-Hubbard model, incorporating both nonlinear interaction and tunneling term. This investigation introduces a novel approach which employs an Ansatz for the wave function in terms of a linear combination of GCS, where the differential equations of all the variables are determined by the time-dependent variational principle without truncation. This innovative method is adeptly applied to the nonequilibrium dynamics in various scenarios, from the bosonic Josephson Junction model where some fundamental quantum effects can be revealed by a handful of GCS basis functions, to large system size implementations of the Bose-Hubbard model, where the phenomenon of thermalization can be observed. The proposed variational approach provides an alternative way to study the time-dependent dynamics in many-body quantum systems conserving particle number.

The final focus of this thesis is on the boson sampling problem within a linear optical network framework. Again adapting a linear combination of GCS, an exact analytical formula for the output state in standard boson sampling scenarios is derived by means of Kan's formula, showcasing a computational complexity that increases less severely with particle and mode number than the super-exponential scaling of the Fock state Hilbert space. The reduced density matrix of the output state is obtained by tracing out one subsystem. This part of the study extends to examining the properties of the subsystem entanglement creation, and offering novel perspectives on entanglement entropy differences between global and local optical networks.

This thesis makes several contributions to the field of quantum many-body systems, particularly highlighting the potential applications of GCS. The presented research offers a new variational method to the nonequilibrium dynamics, and paves the way for future explorations and applications in quantum simulations, quantum computing and beyond.

Table of contents

1 Introduction **1**

2 Properties of generalized coherent states **5**

- 2.1 Definition of generalized coherent states 5
  - 2.1.1 A simple example 6
  - 2.1.2 Group theoretical background 7
  - 2.1.3 Momentum space 8
- 2.2 Relation with Glauber coherent states 8
- 2.3 Completeness of coherent state bases 11
  - 2.3.1 Glauber CS 11
  - 2.3.2 GCS 13
- 2.4 Entanglement entropy of GCS 14

3 Dynamics driven by strong interaction **19**

- 3.1 Dynamics of Glauber CS in deep lattice 19
- 3.2 Two-point correlation function 21
- 3.3 Autocorrelation function of the evolved GCS 25
  - 3.3.1 Exact solution for autocorrelation function 26
  - 3.3.2 Dynamical free energy density 28
  - 3.3.3 General Hamiltonian 35

4 Variational dynamics of multiple generalized coherent states **37**

- 4.1 Variational basis function based on Glauber CS 38
- 4.2 Bose-Hubbard model 39
- 4.3 Linear combination of GCS 40
- 4.4 Equations of motion for the GCS basis 43
  - 4.4.1 Variational principles 43
  - 4.4.2 TDVP applied to the GCS basis function 46

4.5 A first numerical appetizer: the bosonic Josephson junction 52
4.5.1 Classical description of the bosonic Josephson junction 53
4.5.2 Beyond mean-field theory 58
4.6 Numerical appetizer II:Three-mode BH model 68

5 Variational multi-layer GCS and thermalization 75
5.1 Variational multi-layer GCS 75
5.2 Truncated Wigner approximation 79
5.3 Thermalization: classical and quantum 81
5.3.1 Eigenstate Thermalization Hypothesis 81
5.3.2 Numerical results 83

6 Entanglement in boson sampling 91
6.1 Introduction to Boson sampling 92
6.2 Boson Sampling as a unitary evolution 94
6.3 Application of the GCS bases 96
6.3.1 Exact representation of the initial state: Kan summation formula . . 96
6.3.2 Unitary evolution 99
6.4 The entanglement entropy 100
6.4.1 Bipartitioning and Rényi entropies 100
6.4.2 Numerical results for the case $t = 1$ 103
6.4.3 Build-up of entanglement 108
6.4.4 Linear optical network with layers 111

7 Summary and Outlook 113

Appendix A Some properties of generalized coherent states 117

Appendix B Variational principles 121

Appendix C Detailed convergence study with respect to grid spacing 127

Appendix D Rederivation of Glynn’s formula for the permanent 131

Appendix E Derivation of the purity in terms of the unitary 133

References 135

Publications 149

List of Abbreviations

CS	coherent states
vMCG	variational multi-configurational Gaussian
CCS	coupled coherent states
GCS	generalized coherent states
BH	Bose-Hubbard
TWA	truncated Wigner approximation
BS	boson sampling
TDVP	time-dependent variational principle
DFVP	Dirac-Frenkel variational principle
MCVP	McLachlan's variational principle
TDSE	time-dependent Schrödinger equation
RHS	right hand side
LHS	left hand side
BJJ	bosonic Josephson junction
SSB	spontaneous symmetry-breaking
SPDM	single particle density matrix
ETH	eigenstate thermalization hypothesis
MPS	matrix product states
HRU	Haar random unitary matrix
CFS	collision-free subspace

Chapter 1

Introduction

In his seminal 1972 paper "More is Different" [1], P.W.Anderson argued that the behavior of complex systems markedly differs from that of their simple constituents, which are governed by fundamental laws. This concept is exemplified in the contrast between the behavior of a single electron, deeply understood through quantum electrodynamics, and the collective behavior of numerous electrons in crystals, which cannot be simply deduced by summing the behaviors of individual electrons. Such many-body systems, involving more than a handful of interacting particles, necessitate tailored concepts and methods for their study. Over recent decades, experimental progress in many-body physics has unveiled a plethora of novel phenomena, including high-temperature superconductivity, topological materials, many-body localization, and quantum simulation in ultra-cold atomic systems [2–9]. These discoveries have significantly enhanced our understanding of many-body systems and propelled the development of new materials.

However, the theoretical exploration of these systems presents formidable challenges. A prime example are qubit systems, where the complexity grows exponentially with the number of spins, rendering fully quantum simulations on classical computers for even moderately sized systems extremely challenging [10]. Further complicating matters, the ineffectiveness of perturbation theory in strongly correlated systems precludes straightforward analytical solutions. Recently, methods leveraging quantum information concepts such as tensor networks, have shown that the rapid increase in entanglement entropy poses significant barriers to efficient numerical simulations [11]. The exponential growth of computational requirements with entanglement entropy renders simulations of higher-dimensional systems or non-equilibrium dynamics even in one-dimensional systems particularly intractable, symbolizing an "exponential wall" for efficient many-body system simulations.

Despite these challenges, various numerical methods like mean-field theory, exact diagonalization, quantum Monte Carlo, density matrix renormalization group as well as the above mentioned tensor networks have been developed [12–17]. These methods, based on various approximations, have been instrumental in advancing our understanding of quantum phase transitions, critical phenomena, non-equilibrium dynamics, and quantum simulations [18–21].

In the realm of quantum chemistry, novel approaches for solving time-dependent Schrödinger equations in molecular systems have been developed based on Gaussian basis functions, which correspond to the Glauber CS in quantum optics. Eric J. Heller originally used a single Gaussian wavepacket incorporating several time-dependent parameters to model the dynamics of the molecular nuclei [22]. This method's validity stems from the fact that Gaussian wavepackets yield precise results for harmonic potentials. For more complex scenarios, a more adaptable solution has been suggested: instead of using a single Gaussian basis function, a set of basis functions should be employed [23]. In this method, each basis function follows its own classical trajectory, and the overall state is represented by a collective summation of these individual trajectories. Similarly, the renowned Herman-Kluk method is constructed by approximating the quantum mechanical propagator using a collection of independent Gaussian basis functions and including the correct semiclassical prefactor [24]. These time-dependent coefficients in front of each Gaussian basis function were introduced by Herman and Kluk to enhance the solution's effectiveness. The coefficients, alongside the Gaussian basis functions' characteristic parameters form the total set of variables.

By retaining the linear combination of Gaussian basis functions but employing fully quantum variational principles, including the Dirac-Frenkel [25], McLachlan's [26], and time-dependent variational principles [27], one can derive optimal differential equations for these variables, which leads to the so-called variational multi-configurational Gaussian (vMCG) method, where a good view for this method can be found in [28]. Crucially, the coefficients interconnect all trajectories, enabling the uncovering of quantum effects, which could possibly be missed by uncoupled trajectories. In principle, using a sufficient number of Gaussian basis functions should yield the exact quantum results which is granted by the overcompleteness of Glauber CS and the fully quantum variational principles. However, vMCG's requirement to solve a complex set of mutually coupled nonlinear differential equations presents a significant challenge. To overcome this, the Coupled Coherent State (CCS) method was proposed [29]. CCS simplifies the process by allowing the coefficients to follow the fully quantum variational principle, while propagating the Gaussian basis functions along classical trajectories. While CCS offers a simpler set of equations to solve, its effectiveness heavily depends on the sampling of the initial basis function parameters [30].

In our study, we will adopt the spirit of the vMCG approach adapted to a new set of basis functions, tailored for many-body systems. Rather than using standard Gaussian basis functions, we will employ the generalized coherent states (GCS) developed through group theory [31, 32], and leverage their advantages to facilitate numerical simulations.

The second chapter introduces the GCS concept, providing a physical interpretation in quasi-momentum space. We will also explore the nuanced connection between multimode Glauber CS and GCS, delineating their similarities and differences. This includes examining the expansion of CS in terms of GCS, the impact of the annihilation operator on these states, their correlation functions, the overlap between two CS or two GCS, and their overcompleteness properties. Additionally, we will investigate the entanglement properties of GCS that Glauber CS lack.

In the third chapter we will delve into the comparison between Glauber CS and GCS with regard to the description of nonequilibrium dynamics. The model we study is a multimode nonlinear system which only involves on-site interaction among bosons. We begin by analyzing the Husimi function of the temporal state initiated as a multimode Glauber CS to highlight nonlinear effects. Due to the factorization of the Hamiltonian and the multimode Glauber CS, our focus will be on the dynamics of a single mode. We then derive two-point correlation functions from the GCS-initiated temporal state. This analytical expression reveals that the GCS solution becomes equivalent to the CS one in the thermodynamic limit of large particle numbers. Another key topic in this chapter is the survival probability and the related concept of dynamical free-energy as well as dynamical phase transitions. Employing the generating function approach, we obtain exact numerical results for the evolved GCS's survival probability. Most notably, we demonstrate that in the thermodynamic limit, the survival probability of the evolved GCS correlates to that of the evolved Glauber CS through a Fourier series, providing a framework to interpret our numerical findings.

In the forth chapter, we will investigate the non-equilibrium dynamics in the more generic so-called Bose-Hubbard (BH) model. The key point of this part is our basis function employed to solve the time-dependent Schrödinger equation. The initial state is formulated as a linear combination of a set of GCS. Analogous to the vMCG, we integrate both the expansion coefficients and the characteristic parameters of the basis functions. Their differential equations are derived using the time-dependent variational principle. We will apply these basis functions to various scenarios to validate our methodology. The first scenario we thoroughly investigate is the bosonic Josephson junction, described by a two-mode BH model. Initially, we use a single GCS to derive mean-field equations for the relative phase and site population imbalance, examining their stability properties using the Jacobi matrix. Then, we implement our Ansatz composed of different GCS to replicate some quantum effects, including plasma oscillation and spontaneous symmetry breaking. A notable discovery is that employing just a few GCS can significantly surpass mean-field theory predictions. Our second case study focuses on the three-site BH model, whose classical counterpart exhibits traces of chaotic behavior. This model serves to explore the dynamics of site-specific populations and the condensate fraction, both of which are of experimental interest. Additionally, we aim to show how interaction strength influences the efficacy of our method.

In the fifth chapter, a multi-layer GCS basis function method is developed to analyze dynamics initiated by multimode Glauber CS in an 11-site system. The study examines thermalization using both quantum variational methods and the classical Truncated Wigner Approximation (TWA), revealing that interaction strength (J/U) and average particle number ($\tilde{N}$) significantly influence the approach to thermal equilibrium.

In the sixth chapter, our focus shifts to the application of our basis functions to the Boson sampling (BS) problem. A typical BS setup comprises three components: 1) the input state, which is usually a Fock state; 2) a linear optical network; and 3) detectors at the output ports. This system adheres to particle number conservation, which is advantageous for the application of GCS. The primary challenge is to devise a method for representing Fock states in terms of GCS, a problem addressed by Kan's formula. This representation allows us to obtain the output state through a straightforward, analytical unitary transformation. Once the exact output state is determined, its corresponding density matrix can be readily calculated. By dividing the output state into two parts, we obtain the reduced density matrix by tracing out one part of the total state. This reduced density matrix will be our tool to study the entanglement properties of the output state.

To maintain the clarity and flow of the main text, more intricate derivations and discussions have been relegated to the appendix.

Chapter 2

Properties of generalized coherent states

In this chapter, the concept of a GCS will be introduced along with a comprehensive discussion of its fundamental properties, which include a physical explanation of the state, some fundamental properties, and an analysis of its entanglement entropy. The understanding of these properties will establish a solid foundation for subsequent sections of this thesis. Additionally, a key focus of this chapter is to build up the relationship between the generalized coherent states and the more standard, so-called Glauber CS. This relationship will be elucidated by highlighting their similarities and differences across various scenarios.

2.1 Definition of generalized coherent states

In fact, there exist several different kinds of GCS which are obtained by generalizing the concept of Glauber CS via group theory [33]. In this thesis, we focus on one class of them, which are known as SU(M) CS. The most widely accepted representations of the GCS we used is given by [31, 32]:

$$|S,\vec{\xi}\rangle = \frac{1}{\sqrt{S!}} \left(\sum_{j=1}^{M} \xi_j \hat{a}_j^\dagger \right)^S |0,0,\cdots,0\rangle, \tag{2.1}$$

where $\hat{a}_j^\dagger$ represents the bosonic creation operator acting on the j-th mode or site in a lattice system and the bosonic commutator relation

$$[\hat{a}_i, \hat{a}_j^\dagger] = \delta_{ij} \tag{2.2}$$

is fulfilled by the ladder operators, which act on the number states as follows

$$\hat{a}|n\rangle = \sqrt{n}|n-1\rangle, \tag{2.3}$$

$$\hat{a}^{\dagger}|n\rangle = \sqrt{n+1}|n+1\rangle. \tag{2.4}$$

Furthermore, the ket $|0,0,\cdots,0\rangle$ denotes the multi-mode vacuum state, and S is the number of bosons in the GCS. The set of complex numbers $\{\xi_j\}$ are characteristic parameters of the GCS, satisfying the normalization condition

$$\sum_{j=1}^{M} |\xi_j|^2 = 1, \tag{2.5}$$

where M is the number of different modes. The physical interpretation of $|\xi_j|^2$ is the normalized population density or probability for the particles to be located on the j-th site. With the general binomial (or multinomial) theorem from Equation (A.5), a GCS can be expanded in terms of the Fock states

$$|S,\vec{\xi}\rangle = \sum_{[n_i]=S} \sqrt{S!}\prod_{i=1}^{M}\frac{1}{n_i!}(\xi_i\hat{a}_i^{\dagger})^{n_i}|0,0,\cdots,0\rangle, \tag{2.6}$$

where the sum $\sum_{[n_i]=S}$ is the short-hand notation of $\sum_{n_1+n_2+\cdots+n_M=S}$, which accounts for all possible configurations satisfying the constraint on the total particle number. The parameters S and M characterizing the system size determine the dimension of the Hilbert space

$$C_{M+S-1}^{M-1} = \begin{pmatrix} M+S-1 \\ M-1 \end{pmatrix}, \tag{2.7}$$

spanned by the Fock states. This is the same as the number of configurations produced by placing S identical balls into M different boxes.

2.1.1 A simple example

It is instructive to write out the definition in Eq. (2.1) explicitly for small numbers such as $M = 2 \leq S$ to convince oneself of the fact that the GCS is a superposition of Fock states with coefficients to be determined from a generalized binomial formula. For instance, we can consider the GCS $|2,\frac{1}{\sqrt{2}},\frac{1}{\sqrt{2}}\rangle$ where 2 modes are occupied by 2 particles, and this state can be expanded within the Fock state basis as

$$|2,\frac{1}{\sqrt{2}},\frac{1}{\sqrt{2}}\rangle = \frac{1}{2}|20\rangle + \frac{1}{\sqrt{2}}|11\rangle + \frac{1}{2}|02\rangle \tag{2.8}$$

where all possible Fock states with same particle number are involved. It is also evident that this state is an entangled state, since it cannot be factorized.

2.1.2 Group theoretical background

Alternatively, the GCS can be generated by applying an element of the SU(M) group to an extreme state in which all the particles occupy a single mode [31, 33]. To show that, we define the operator

$$A^\dagger = \sum_{j=1}^{M} \xi_j \hat{a}_j^\dagger \tag{2.9}$$

with the help of which the GCS can be written as $\frac{1}{\sqrt{S!}}(A^\dagger)^S|0,0,\cdots,0\rangle$. The operator $A^\dagger$ can be generated by a unitary transformation such as

$$A^\dagger = T\hat{a}_j^\dagger T^\dagger, \tag{2.10}$$

where T is a unitary operator. We note that the choice of $\hat{a}_j^\dagger$ is arbitrary; without loss of generality, we can set $\hat{a}_j^\dagger = \hat{a}_1^\dagger$. Since $A^\dagger$ is just a linear combination of creation operators, using the Baker-Haussdorff formula, it can be proven that the unitary operator of the form

$$T = \mathrm{e}^{\mathrm{i}\sum_{l=2}^{M}(\eta_l^* \hat{a}_1^\dagger \hat{a}_l + \eta_l \hat{a}_l^\dagger \hat{a}_1)} \tag{2.11}$$

leads to the required $A^\dagger$, where the vector $\vec{\eta}$ contains the information of the characteristic parameters $\vec{\xi}$. Now the form of the GCS becomes

$$\frac{1}{\sqrt{S!}}(A^\dagger)^S|0,0,\cdots,0\rangle = \frac{1}{\sqrt{S!}}T^\dagger(\hat{a}_1^\dagger)^S T|0,0,\cdots,0\rangle = \frac{1}{\sqrt{S!}}T^\dagger|S,0,\cdots,0\rangle, \tag{2.12}$$

where the second equality is due to the fact that $T|0,0,\cdots,0\rangle = |0,0,\cdots,0\rangle$, and $|S,0,\cdots,0\rangle$ is the extreme state mentioned before. As the generator of T is a traceless Hermitian operator $\sum_{l=2}^{M}(\eta_l^* \hat{a}_1^\dagger \hat{a}_l + \eta_l \hat{a}_l^\dagger \hat{a}_1)$, T is an element of the SU(M) group. In the literature, the GCS is therefore also called SU(M) coherent state. Although Eq. (2.12) encompasses the symmetry information of GCS, in practice, the equivalent form given by Eq. (2.1) is much more useful to facilitate numerical implementations, as we will see in the remainder of this thesis.

2.1.3 Momentum space

From the definition in Eq. (2.1), a GCS can be understood as a special form of condensate, where all particles macroscopically occupy a single-particle state given by $\sum_{j=1}^{M}\xi_j\hat{a}_j^\dagger|0,0,\cdots,0\rangle$. This non-local nature of the single-particle state implies that any particle can be found at any site, with probabilities determined by $|\xi_i|^2$.

To further illustrate the concept of a condensate, we can represent the GCS in the quasi-momentum frame. To this end, we consider a 1D lattice characterized by a lattice constant a. Next, we introduce a set of creation operators $\hat{b}_k^\dagger$, which act on the quasi-momentum k, and are related to the $\hat{a}_j^\dagger$ through a Fourier transformation:

$$\hat{b}_k^\dagger = \frac{1}{\sqrt{M}}\sum_{j=1}^{M}\hat{a}_j^\dagger \mathrm{e}^{\mathrm{i}jka}, \tag{2.13}$$

with k ranging from $-\frac{\pi}{a}$ to $\frac{\pi}{a}$. Particularly noteworthy is the case of zero quasi-momentum, for which we have

$$\hat{b}_{k=0}^\dagger = \frac{1}{\sqrt{M}}\sum_{j=1}^{M}\hat{a}_j^\dagger. \tag{2.14}$$

Homogeneous characteristic parameters of the GCS, i.e., $\xi_j = \frac{1}{\sqrt{M}}$ for all sites will cause all the particles to condense into the zero-momentum state

$$\frac{1}{\sqrt{S!}}\Big(\sum_{j=1}^{M}\frac{1}{\sqrt{M}}\hat{a}_j^\dagger\Big)^S|0,0,\cdots,0\rangle = \frac{1}{\sqrt{S!}}(\hat{b}_{k=0}^\dagger)^S|0,0,\cdots,0\rangle, \tag{2.15}$$

which is the so-called Bose-Einstein condensate [34].

2.2 Relation with Glauber coherent states

The GCS described above exhibit a close connection with the Glauber CS, which are defined through the action of the displacement operator on the ground state of the harmonic oscillator [35]

$$\hat{H} = \frac{\hat{p}^2}{2} + \frac{\omega^2}{2}\hat{x}^2 \tag{2.16}$$

and read

$$|\alpha\rangle = \mathrm{e}^{-\frac{|\alpha|^2}{2}}\mathrm{e}^{\alpha\hat{a}^\dagger}|0\rangle = \mathrm{e}^{-\frac{|\alpha|^2}{2}}\sum_{n=0}^{\infty}\frac{\alpha^n}{\sqrt{n!}}|n\rangle. \tag{2.17}$$

As can be inferred from its definition above, the Glauber CS is the eigenstate of the annihilation operator

$$\hat{a}|\alpha\rangle = \alpha|\alpha\rangle \tag{2.18}$$

where the eigenvalue α is a complex number

$$\alpha = \frac{\omega^{1/2}q + \mathrm{i}\omega^{-1/2}p}{\sqrt{2}} \tag{2.19}$$

in terms of the expectation values of position and momentum, denoted by q, respectively p, and also the width parameter ω, which determines the uncertainty of position and momentum. We note that the mass of the oscillator as well as the reduced Plank constant $\hbar$ are set to unity here and in the remainder of this thesis.

The wavefunction of the Glauber CS in position representation is given by

$$\langle x|\alpha\rangle = \left(\frac{\omega}{\pi}\right)^{\frac{1}{4}}\exp\left[-\frac{\omega}{2}(x-q)^2 + \mathrm{i}p(x-\frac{q}{2})\right]. \tag{2.20}$$

The corresponding probability distribution $|\langle x|\alpha\rangle|^2$ is a Gaussian function as shown in Fig. 2.1.

The concept can be further extended to the multimode Glauber CS, which is represented as the product state of individual single-mode Glauber CSs. As demonstrated in [31] and corroborated by the Taylor expansion of the exponential function, the multimode Glauber CS denoted by $|\vec{\alpha}\rangle = \prod_{i=1}^{M}|\alpha_i\rangle$, is linked to the GCS through the following expression:

$$\begin{aligned}
|\vec{\alpha}\rangle &= \mathrm{e}^{-\frac{1}{2}\sum_{i=1}^{M}|\alpha_i|^2}\mathrm{e}^{\sum_{i=1}^{M}\alpha_i\hat{a}_i^\dagger}|0,0,\cdots,0\rangle \\
&= \mathrm{e}^{-\frac{1}{2}\sum_{i=1}^{M}|\alpha_i|^2}\sum_{S=0}^{\infty}\frac{1}{S!}(\sum_{i=1}^{M}\alpha_i\hat{a}_i^\dagger)^S|0,0,\cdots,0\rangle \\
&= \mathrm{e}^{-\frac{\tilde{N}}{2}}\sum_{S=0}^{\infty}\frac{\tilde{N}^{\frac{S}{2}}}{\sqrt{S!}}\frac{1}{\sqrt{S!}}\left(\sum_{i=1}^{M}\frac{\alpha_i}{\sqrt{\tilde{N}}}\hat{a}_i^\dagger\right)^S|0,0,\cdots,0\rangle \\
&= \mathrm{e}^{-\frac{\tilde{N}}{2}}\sum_{S=0}^{\infty}\frac{\tilde{N}^{\frac{S}{2}}}{\sqrt{S!}}|S,\vec{\xi}\rangle.
\end{aligned} \tag{2.21}$$

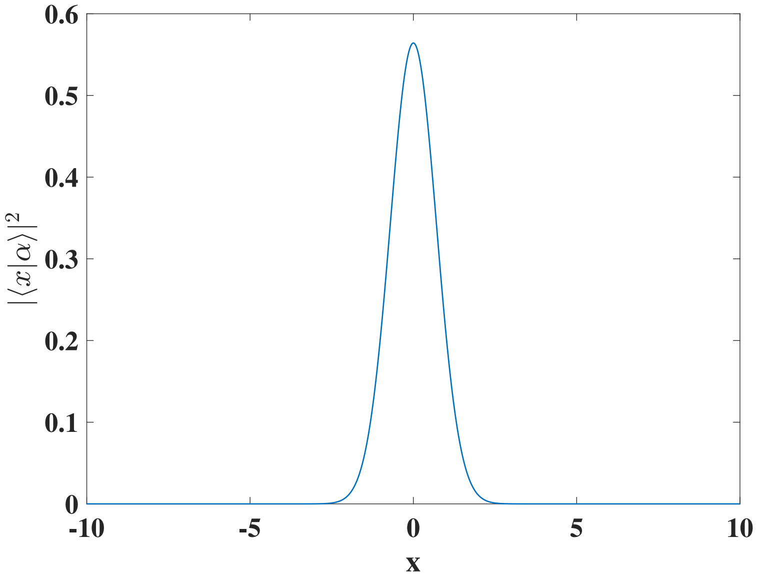

Fig. 2.1 The probability distribution $|\langle x|\alpha\rangle|^2$ in position representation. ω is set to be 1 and $(q,p)=(0,1)$.

Here, $\tilde{N}=\sum_{i=1}^{M}|\alpha_i|^2$ denotes the average number of bosons in $|\vec{\alpha}\rangle$. We note that the relationship between ξ_i and α_i is given by

$$\xi_i=\frac{\alpha_i}{\sqrt{\tilde{N}}},$$

which is reasonable, because $|\alpha_i|^2$ denotes the average number of particles while $|\xi_i|^2=\frac{|\alpha_i|^2}{\tilde{N}}$ corresponds to the normalized population density as shown in Sec.2.1. Furthermore, we note that if all the α_i share the same phase, the corresponding parameter $\xi_i=\frac{|\alpha_i|}{\sqrt{\tilde{N}}}$ as the phase is treated as a global one in GCS. Finally, the expansion coefficient

$$\mathrm{e}^{-\frac{\tilde{N}}{2}}\tilde{N}^{\frac{S}{2}}/\sqrt{S!}$$

proves that the total number of particles follows the Poisson distribution with the mean $\tilde{N}$. Eq. (2.21) establishes that the multimode Glauber CS is a superposition of GCS with varying particle numbers S, or equivalently speaking, one GCS with particle number S can be acquired by projecting the Glauber CS onto the S-particle subspace. Consequently, it is natural to construct a one-to-one mapping between the GCS and multimode Glauber CS.

The similarities and difference are summarized in Table 2.1, while some results for the GCS case are proven in Appendix. A. The definitions of multimode Glauber CS and GCS are presented in the second line of the table, where it becomes evident that the Glauber CS is a product state, while the GCS cannot generally be factorized. In the third line, we examine the impact of annihilation operators on the two states. The Glauber CS emerges as an eigenstate

Multi-mode Glauber CS	GCS
$\vert\vec{\alpha}\rangle = \prod_{i=1}^{M} \mathrm{e}^{-\frac{\vert\alpha_i\vert^2}{2}} \mathrm{e}^{\alpha_i \hat{a}_i^\dagger} \vert\mathrm{vac}\rangle = \otimes_{i=1}^{M} \vert\alpha_i\rangle$	$\vert S,\vec{\xi}\rangle = \frac{1}{\sqrt{S!}} \left(\sum_{i=1}^{M} \xi_i \hat{a}_i^\dagger\right)^S \vert\mathrm{vac}\rangle$
$\hat{a}_i\vert\vec{\alpha}\rangle = \alpha_i\vert\vec{\alpha}\rangle$	$\hat{a}_i\vert S,\vec{\xi}\rangle = \sqrt{S}\xi_i\vert S-1,\vec{\xi}\rangle$
$\langle\vec{\alpha}\vert\hat{a}_i^\dagger \hat{a}_j\vert\vec{\alpha}\rangle = \alpha_i^* \alpha_j$	$\langle S,\vec{\xi}\vert\hat{a}_i^\dagger \hat{a}_j\vert S,\vec{\xi}\rangle = S\xi_i^*\xi_j$
$\langle\vec{\alpha}\vert\vec{\beta}\rangle = \exp\left[\sum_{i=1}^{M} \alpha_i^*\beta_i - \frac{1}{2}(\vert\alpha_i\vert^2 + \vert\beta_i\vert^2)\right]$	$\langle S',\vec{\xi}\vert S,\vec{\eta}\rangle = \left(\sum_{i=1}^{M} \xi_i^*\eta_i\right)^S \delta_{S,S'}$
overcomplete in whole Hilbert space	overcomplete in S-particle subspace

Table 2.1 Comparison between multi-mode Glauber CS and GCS

of the annihilation operator $\hat{a}_i$ with the eigenvalue α_i. In contrast, $\hat{a}_i$ annihilates a particle from the original GCS and generates a new GCS with the particle number $S-1$. Moving to the fourth line, the computation of the two-point correlation function is facilitated by the insights from the third line. The correlation functions of both states remain independent of the spatial separation between points i and j, which proves that Glauber CS and GCS have long-range coherence. In the next line, we present the inner product between two Glauber CS and two GCS, respectively, both of which are non-orthogonal. The overlap of two different Glauber CSs has an exponential form, and for GCS, the overlap is expressed as a polynomial.

2.3 Completeness of coherent state bases

In the following, we highlight that both sets of states can serve as overcomplete bases, despite GCS being limited to the S-particle subspace, which implies that a large number of Glauber CS or GCS can be employed to represent an arbitrary state. We will make extensive use of this fact in later parts of this thesis.

2.3.1 Glauber CS

The well-established overcompleteness of CS is reflected in the expansion of the identity operator,

$$I = \frac{1}{\pi}\int_{-\infty}^{\infty} \mathrm{d}^2\alpha|\alpha\rangle\langle\alpha|. \tag{2.22}$$

Eq. (2.22) is tailored for the single-mode case, and the generalization to the multimode case is straightforward with the direct product of sets of identities acting on different modes. However, this expansion expressed by continuous integration, is not a favorable form for the numerical application. It is worth noting that a subset of an overcomplete basis may still retain completeness. In last century, two independent contributions have proven the statement that a discretized version of the identity operator is given by

$$\sum_{k,l} |\alpha_k\rangle (\mathbf{\Omega}^{-1})_{kl} \langle \alpha_l| = \hat{I}, \tag{2.23}$$

with the overlap matrix $\mathbf{\Omega}$ with elements

$$\mathbf{\Omega}_{kl} = \langle \alpha_k | \alpha_l \rangle, \tag{2.24}$$

if the requirement

$$\alpha_k = \beta(m + \mathrm{i}n), \tag{2.25}$$

with $k = (m, n)$ where m, n are integers and $0 < \beta \leq \sqrt{\pi}$, for the spacing of the grid points is met [36, 37]. Physically, this means that the cells in (p, q) phase space defined in Eq. (2.19) that are spanned by the grid points must have an area less than or equal to the Planck cell area of 2π in the present units (where $\hbar = 1$, $\omega = 1$), such cell is display by the shadow area in Fig. 2.2. The limiting case of $\beta = \sqrt{\pi}$ for the spacing of the grid points has already been postulated long before by von Neumann [38, 39].

The discrete version of the identity operator in terms of multimode Glauber CS is written as

$$\sum_{k,l} |\vec{\alpha}_k\rangle (\mathbf{\Omega}^{-1})_{kl} \langle \vec{\alpha}_l| = \hat{I}. \tag{2.26}$$

Here, the parameters of Glauber CSs are vectorized as $\vec{\alpha}_k = \{\alpha_{k1}, \cdots, \alpha_{kj}, \cdot, \alpha_{kM}\}$ to handle various degrees of freedom, where k is the vector index. Each element α_{kj} is sampled from the independent grids displayed in Fig. 2.2. The matrix $\mathbf{\Omega}$ is an overlap matrix consisting of the elements $\mathbf{\Omega}_{kl} = \langle \vec{\alpha}_k | \vec{\alpha}_l \rangle$.

A heuristic examination of the closure relation can be obtained in the following way: Given any two coherent $|\vec{\alpha}_m\rangle$ and $|\vec{\alpha}_m\rangle$ and inserting unity in the multi degree of freedom case yields

$$\langle \vec{\alpha}_m | \vec{\alpha}_n \rangle = \sum_{k,l} \langle \vec{\alpha}_m | \vec{\alpha}_k \rangle (\mathbf{\Omega}^{-1})_{kl} \langle \vec{\alpha}_l | \vec{\alpha}_n \rangle \tag{2.27}$$

where the equation is justified by the matrix multiplication $\mathbf{\Omega} = \mathbf{\Omega}\mathbf{\Omega}^{-1}\mathbf{\Omega}$.

2.3.2 GCS

Inspired by the one-to-one mapping between multimode Glauber CS and GCS, it is natural to infer that a set of discrete GCS could also serve as a complete basis. This intuition is substantiated by considering two arbitrary states, $|\psi_S\rangle$ and $|\phi_S\rangle$ both of which contain S particles. From Eq. (2.21), it is evident that only the GCS with S particles have non-zero contribution to the overlap with the state $|\psi_S\rangle$ or $|\phi_S\rangle$. Consequently,

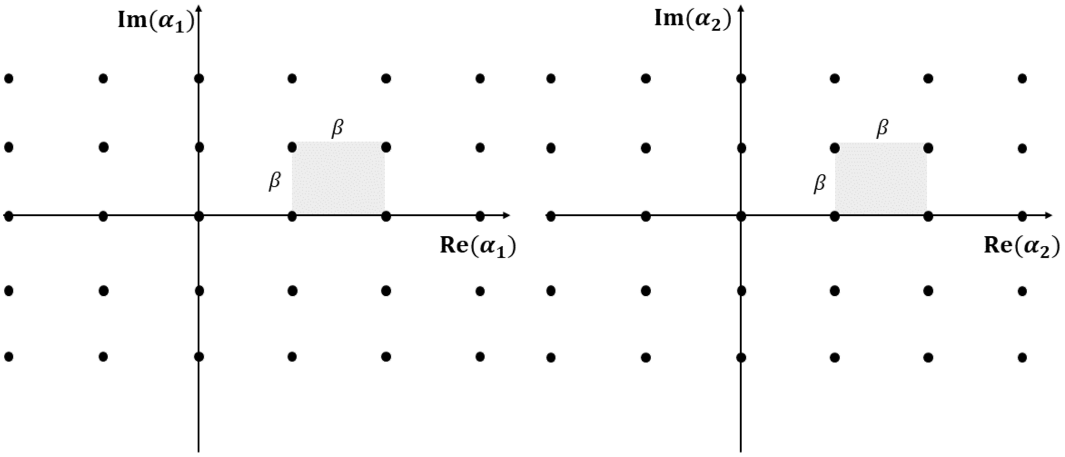

Fig. 2.2 The two independent complex grids for α_{k1} and α_{k2}.

$$\begin{aligned}\langle\psi_S|\phi_S\rangle &= \langle\psi_S|\sum_{k,l}|\vec{\alpha}_k\rangle(\mathbf{\Omega}^{-1})_{kl}\langle\vec{\alpha}_l|\cdot|\phi_S\rangle \\ &= \langle\psi_S|\sum_{k,l}|S,\vec{\xi}_k\rangle(\tilde{\mathbf{\Omega}}^{-1})_{kl}\langle S,\vec{\xi}_l|\cdot|\phi_S\rangle,\end{aligned} \tag{2.28}$$

where the expansion coefficients in Eq. (2.21) are incorporated into the $\tilde{\mathbf{\Omega}}^{-1}$, so $\tilde{\mathbf{\Omega}}^{-1}$ is written as follows

$$(\tilde{\mathbf{\Omega}}^{-1})_{kl} = \mathrm{e}^{-\frac{\tilde{N}_k+\tilde{N}_l}{2}}\frac{\tilde{N}_k^{\frac{S}{2}}\tilde{N}_l^{\frac{S}{2}}}{S!}(\mathbf{\Omega}^{-1})_{kl} \tag{2.29}$$

where $\tilde{N}_k = \sum_{i=1}^{M} |\alpha_{ki}|^2$ and $\mathbf{\Omega}^{-1}$ is defined by Eq. (2.26).

Eq. (2.28) underscores that the discrete GCS derived from corresponding Glauber CSs can indeed constitute a complete basis within the S-particle subspace, leading to the expression:

$$\sum_{k,l} |S, \vec{\xi}_k\rangle (\tilde{\mathbf{\Omega}}^{-1})_{kl} \langle S, \vec{\xi}_l| = \hat{I}. \tag{2.30}$$

We now consider the two-mode case as an instructive example. Taking samples from these two grids for α_{k1} and α_{k2} randomly from Fig. 2.2, every produced pair of $\{\alpha_{k1}, \alpha_{k2}\}$ forms a two-mode Glauber coherent state $|\alpha_{k1}, \alpha_{k2}\rangle$. The $\{\alpha_{k1}, \alpha_{k2}\}$ correspond to a set of couples of parameters $\{\xi_{k1}, \xi_{k2}\} = \{\frac{\alpha_{k1}}{\sqrt{|\alpha_{k1}|^2+|\alpha_{k2}|^2}}, \frac{\alpha_{k2}}{\sqrt{|\alpha_{k1}|^2+|\alpha_{k2}|^2}}\}$ for the SU(2) GCS, but due to the normalization condition ξ_{k1} and ξ_{k2} adhere to, they cannot be presented on two independent complex planes. We are now rewriting the GCS parameters in the form

$$\xi_{k1} = \cos\left(\frac{\theta_k}{2}\right) \tag{2.31}$$

$$\xi_{k2} = \sin\left(\frac{\theta_k}{2}\right) e^{i\phi_k}, \tag{2.32}$$

where $0 \leq \theta_k \leq \pi$ and $0 \leq \phi_k \leq 2\pi$ are the angles and the relative phases, respectively. Because we have just two angles for every k and because of the factor of 1/2 that comes along with the angle θ_k, this allows us to represent the GCS parameters as points on the northern hemisphere of the Bloch sphere.

For a visualization, we first generated 50 random pairs of $\{\alpha_{k1}, \alpha_{k2}\}$. Using the angles $\{\theta_k, \phi_k\}$, the corresponding 50 pairs of $\{\xi_{k1}, \xi_{k2}\}$ can be expressed via

$$\{\cos(\theta_k/2)\cos(\phi_k), \cos(\theta_k/2)\sin(\phi_k), \sin(\theta_k/2)\}, \tag{2.33}$$

as displayed in Fig. 2.3.

2.4 Entanglement entropy of GCS

In this section, we will explore some entanglement properties of the GCS. In many-body systems such as a 1D chain of sites, we can divide the system into two parts, and trace out one part to get the bipartition entanglement which can be used to account for the quantum correlation between the subsystems depicted in Fig. 2.4.

The following derivation is based on the Schmidt decomposition [40] and focuses on single GCS with M sites and S particles. The same result can be obtained by using the reduced

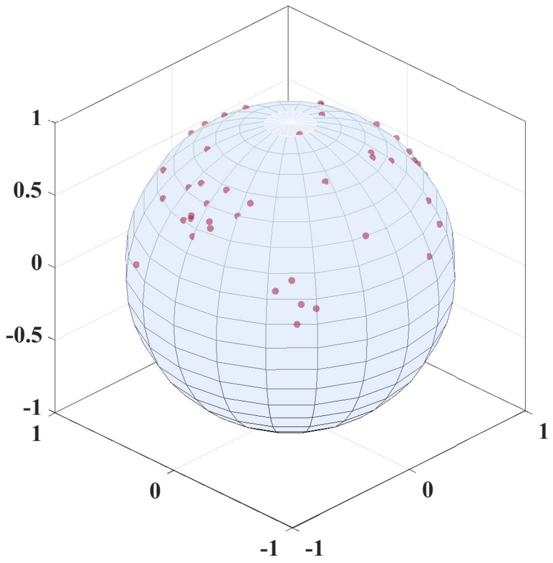

Fig. 2.3 Some of the 50 grid points $\{\xi_{k1}, \xi_{k2}\}$ on the surface of the unit sphere. There are more points on the back, which are invisible from the present perspective.

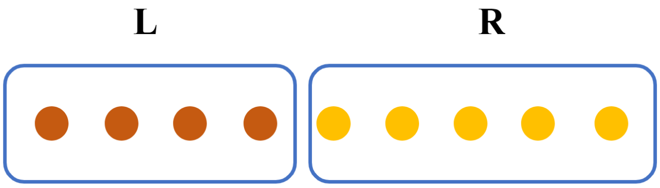

Fig. 2.4 Bipartite system consisting of left part and right part.

density matrix [41]. The single GCS in one dimension can be divided into a left and a right part via the binomial theorem

$$\begin{aligned}|S,\vec{\xi}\rangle &= \frac{1}{\sqrt{S!}}\left(\sum_{i=1}^{M}\xi_i\hat{a}_i^\dagger\right)^S|00\cdots0\rangle \\ &= \frac{1}{\sqrt{S!}}\left(\sum_{i=1}^{M_L}\xi_i\hat{a}_i^\dagger + \sum_{i=M_L+1}^{M}\xi_i\hat{a}_i^\dagger\right)^S|00\cdots0\rangle \\ &= \frac{1}{\sqrt{S!}}\sum_{n=0}^{S}\binom{S}{n}\left(\sum_{i=1}^{M_L}\xi_i\hat{a}_i^\dagger\right)^{S-n}\left(\sum_{i=M_L+1}^{M}\xi_i\hat{a}_i^\dagger\right)^n|00\cdots0\rangle \\ &= \frac{1}{\sqrt{S!}}\sum_{n=0}^{S}\binom{S}{n}\sqrt{n!(S-n)!}|S-n,\vec{\xi}_{\tilde{L}}\rangle\otimes|n,\vec{\xi}_{\tilde{R}}\rangle,\end{aligned} \tag{2.34}$$

where the two non-normalized GCSs are given by

$$|S-n,\vec{\xi}_{\tilde{L}}\rangle = \frac{1}{\sqrt{(S-n)!}}\left(\sum_{i=1}^{M_L}\xi_i\hat{a}_i^\dagger\right)^{S-n}|00\cdots 0\rangle, \tag{2.35}$$

$$|n,\vec{\xi}_{\tilde{R}}\rangle = \frac{1}{\sqrt{n!}}\left(\sum_{i=M_L+1}^{M}\xi_i\hat{a}_i^\dagger\right)^{n}|00\cdots 0\rangle. \tag{2.36}$$

The norms of the two states are expressed as

$$\langle S-n,\vec{\xi}_{\tilde{L}}|S-n,\vec{\xi}_{\tilde{L}}\rangle = \left(\sum_{i=1}^{M_L}|\xi_i|^2\right)^{S-n}, \tag{2.37}$$

$$\langle n,\vec{\xi}_{\tilde{R}}|n,\vec{\xi}_{\tilde{R}}\rangle = \left(\sum_{i=M_L+1}^{M}|\xi_i|^2\right)^{n}, \tag{2.38}$$

and by introducing the normalization factors $1/\sqrt{\left(\sum_{i=1}^{M_L}|\xi_i|^2\right)^{S-n}}$ and $1/\sqrt{\left(\sum_{i=M_L+1}^{M}|\xi_i|^2\right)^{n}}$, we can rewrite the GCS as

$$\begin{aligned}|S,\vec{\xi}\rangle &= \frac{1}{\sqrt{S!}}\sum_{n=0}^{S}\binom{S}{n}\sqrt{n!(S-n)!}\sqrt{\left(\sum_{i=1}^{M_L}|\xi_i|^2\right)^{S-n}\left(\sum_{i=M_L+1}^{M}|\xi_i|^2\right)^{n}}\,|S-n,\vec{\xi}_L\rangle\otimes|n,\vec{\xi}_R\rangle\\ &= \sum_{n=0}^{S}\lambda_n|S-n,\vec{\xi}_L\rangle\otimes|n,\vec{\xi}_R\rangle\end{aligned} \tag{2.39}$$

where the states $|S-n,\vec{\xi}_L\rangle$ and $|n,\vec{\xi}_R\rangle$ denote the normalized GCSs as well as orthonormal bases with respect to the index n because of the inner products $\langle S-n',\vec{\xi}_L|S-n,\vec{\xi}_L\rangle = \delta_{n'n}$, $\langle n',\vec{\xi}_R|n,\vec{\xi}_R\rangle = \delta_{n'n}$.

The parameters λ_n, known as Schmidt coefficients, are given by

$$\begin{aligned}\lambda_n &= \frac{1}{\sqrt{S!}}\binom{S}{n}\sqrt{n!(S-n)!}\sqrt{\left(\sum_{i=1}^{M_L}|\xi_i|^2\right)^{S-n}\left(\sum_{i=M_L+1}^{M}|\xi_i|^2\right)^{n}}\\ &= \sqrt{\binom{S}{n}\left(\sum_{i=1}^{M_L}|\xi_i|^2\right)^{S-n}\left(\sum_{i=M_L+1}^{M}|\xi_i|^2\right)^{n}}.\end{aligned} \tag{2.40}$$

The von Neumann entropy which is a widely used measure of entanglement between the left and right system is expressed as [42]

$$S_{\mathrm{vN}} = -\sum_{n=0}^{S} \lambda_n^2 \ln(\lambda_n^2). \tag{2.41}$$

In the homogeneous case with $\xi_1 = \xi_2 = \cdots = \xi_M = \frac{1}{\sqrt{M}}$, we have

$$\lambda_n^2 = \binom{S}{n} \frac{M_L^{S-n}(M-M_L)^n}{M^S} \tag{2.42}$$

and it is easy to check the normalization condition is satisfied:

$$\sum_{n=0}^{S} \lambda_n^2 = \sum_{n=0}^{S} \binom{S}{n} \frac{M_L^{S-n}(M-M_L)^n}{M^S} = \frac{(M_L+M-M_L)^S}{M^S} = 1. \tag{2.43}$$

For the equal bipartition $M_L = \frac{M}{2}$ where the maximal entropy is reached, $\lambda_n^2 = \frac{1}{2^S}\binom{S}{n}$ and this result suggests that the maximal entropy is solely dependent on the total particle number S. In thermodynamic limit $S \to \infty$ and $M \to \infty$, with filling factor

$$\lambda = \frac{S}{M}, \tag{2.44}$$

we have $|\xi_i|^2 = \frac{\lambda}{S}$. Using the approximation strategy in [41], λ_n^2 can be rederived from Eq. (2.40) as

$$\begin{aligned}
\lambda_n^2 &= \binom{S}{n} \left(\frac{M_L\lambda}{S}\right)^n \left(1 - \frac{M_L\lambda}{S}\right)^{S-n} \\
&= \frac{S!}{(S-n)!n!} \frac{1}{S^n} \left(1 - \frac{M_L\lambda}{S}\right)^S \left(\frac{M_L\lambda}{1 - \frac{M_L\lambda}{S}}\right)^n \\
&= \frac{1}{n!} \mathrm{e}^{-M_L\lambda} \left(M_L\lambda\right)^n,
\end{aligned} \tag{2.45}$$

where for convenience, we have replaced n with $S-n$, and the normalization condition is still satisfied. Correspondingly, the entanglement entropy in the thermodynamic limit is

$$\begin{aligned}
S_{\mathrm{vN}} &= -\sum_{n=0}^{S} \frac{1}{n!} \mathrm{e}^{-M_L\lambda} (M_L\lambda)^n \ln \left[\frac{1}{n!} \mathrm{e}^{-M_L\lambda} (M_L\lambda)^n \right] \\
&= -\mathrm{e}^{-M_L\lambda} \sum_{n=0}^{S} \frac{1}{n!} (M_L\lambda)^n [-\ln n! - M_L\lambda + n\ln(M_L\lambda)] \\
&= \mathrm{e}^{-M_L\lambda} M_L\lambda \sum_{n=0}^{S} \frac{(M_L\lambda)^n}{n!} - \mathrm{e}^{-M_L\lambda} \ln(M_L\lambda) \sum_{n=0}^{S} \frac{(M_L\lambda)^n}{(n-1)!} + \mathrm{e}^{-M_L\lambda} \sum_{n=0}^{S} \frac{(M_L\lambda)^n}{n!} \ln n! \\
&= M_L\lambda[1-\ln(M_L\lambda)] + \mathrm{e}^{-M_L\lambda} \sum_{n=0}^{S} \frac{(M_L\lambda)^n}{n!} \ln n!. \qquad (2.46)
\end{aligned}$$

From Eq. (2.46), we find that the scaling behavior of the entanglement entropy depends on the combined parameter $M_L\lambda$, which represents the ratio of the subsystem size to the inverse of the filling factor. Specifically, if $M_L\lambda$ is much less than 1, the entropy is dominated by the term $M_L\lambda[1-\ln(M_L\lambda)]$. Otherwise the value of the entropy is influenced by both terms.

In Fig. 2.5 (a), we plot S_{vN} as a function of the bipartition M_L with different particle numbers S, and M_L only ranging up to $\frac{M}{2}$, as the curve is symmetric with respect to equal bipartition. We can see that the entropy grows slowly, and increasing S leads to larger entropy. Fig. 2.5 (b) shows the maximal values of entropy as a function of S with fixed $M = 100$, and it can be observed that for small S and larger S, the entropy will grow in different ways.

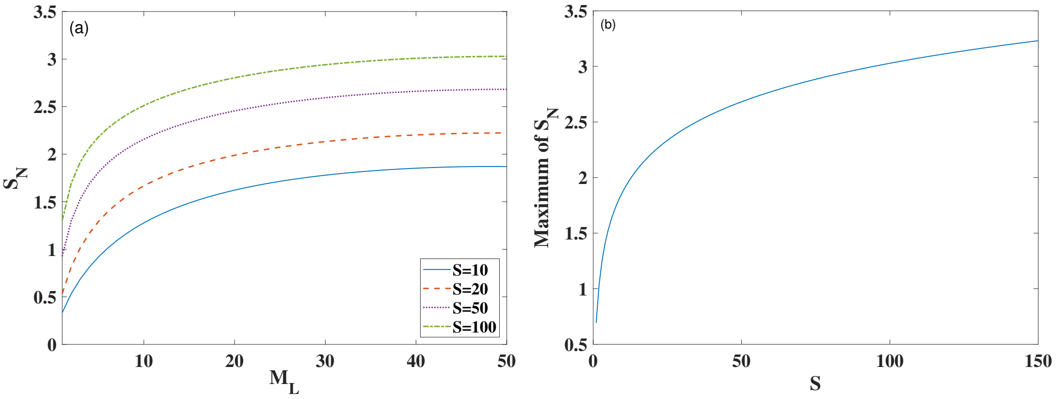

Fig. 2.5 (a) The Von Neumann entropy of the homogeneous GCS as a function of the bipartition, the number of modes is $M = 100$. (b) The maximum entropy as a function of the total particle number inside the interval $[1, 150]$.

Chapter 3

Dynamics driven by strong interaction

In this section, we will discuss various dynamical phenomena induced by strong interaction in quantum many-body systems, which involves the evolution of Husimi functions, population dynamics in quasi-momentum space, and the autocorrelation function. These results can reveal the relationships between CS and GCS initial states and contain some interesting physics related to dynamical phase transitions which can be observed in the quench dynamics governed by Bose-Hubbard type Hamiltonian.

3.1 Dynamics of Glauber CS in deep lattice

For simplicity, let's consider a nonlinear Hamiltonian

$$\hat{H} = \frac{U}{2}\sum_{i=1}^{M} \hat{a}_i^{\dagger 2}\hat{a}_i^2 = \frac{U}{2}\sum_{i=1}^{M} \hat{n}_i(\hat{n}_i - 1) = \sum_{i=1}^{M} \hat{h}_i \tag{3.1}$$

where $\hat{n}_i$ is the number operator $\hat{a}_i^\dagger \hat{a}_i$ acting on the i-th site and $\hat{h}_i$ stands for the local Hamiltonian $\frac{U}{2}\hat{n}_i(\hat{n}_i - 1)$ with on-site interaction strength U. This Hamiltonian is the limiting case of vanishing inter-site hopping of the Bose-Hubbard model to be considered in Chapter. 4 and can be realized in experiment by increasing the intensity of the optical lattice laser beams [43, 44].

If the initial state is a Glauber CS as given in Eq. (2.21), taking advantage of the factorization of the state and Hamiltonian, the time-evolved state can be obtained as follows:

$$
\begin{aligned}
|\psi(t)\rangle &= \exp\left(-\mathrm{i}\sum_{i=1}^{M}\hat{h}_i t\right)|\vec{\alpha}\rangle \\
&= \otimes_{i=1}^{M}\exp(-\mathrm{i}\hat{h}_i t)|\alpha_i\rangle \\
&= \otimes_{i=1}^{M}\mathrm{e}^{-\frac{|\alpha_i|^2}{2}}\sum_{n_i=0}^{\infty}\frac{\alpha^{n_i}}{\sqrt{n_i!}}\mathrm{e}^{-\mathrm{i}\frac{U}{2}n_i(n_i-1)t}|n_i\rangle .
\end{aligned} \tag{3.2}
$$

This result highlights that it is possible to concentrate on the dynamics of a single mode in the homogeneous case $\alpha_i = \alpha$ for $\forall i$. In Fig. 3.1, we present the time evolution of the Husimi function for a single mode state $|\alpha\rangle$ as also shown in [44], defined as

$$
\Omega(\beta,t) = \langle\beta|\exp\left[-\mathrm{i}\frac{U}{2}\hat{n}(\hat{n}-1)t\right]|\alpha\rangle\langle\alpha|\exp\left[\mathrm{i}\frac{U}{2}\hat{n}(\hat{n}-1)t\right]|\beta\rangle, \tag{3.3}
$$

where $|\beta\rangle$ is an arbitrary CS characterized by the complex number $\beta = \mathrm{Re}(\beta) + \mathrm{i}\mathrm{Im}(\beta)$. Due to the factor $n_i(n_i-1)$ in Eq. (3.2) always being an even number, the Husimi function evolves periodically with period $T = 2\pi/U$. For times symmetric around $\frac{\pi}{U}$, like, e.g, $Ut = 0.4\pi$ and $Ut = 1.6\pi$ the results are symmetric along the real part of the β (as are the results for $Ut = 0.8\pi$ and $Ut = 1.2\pi$).

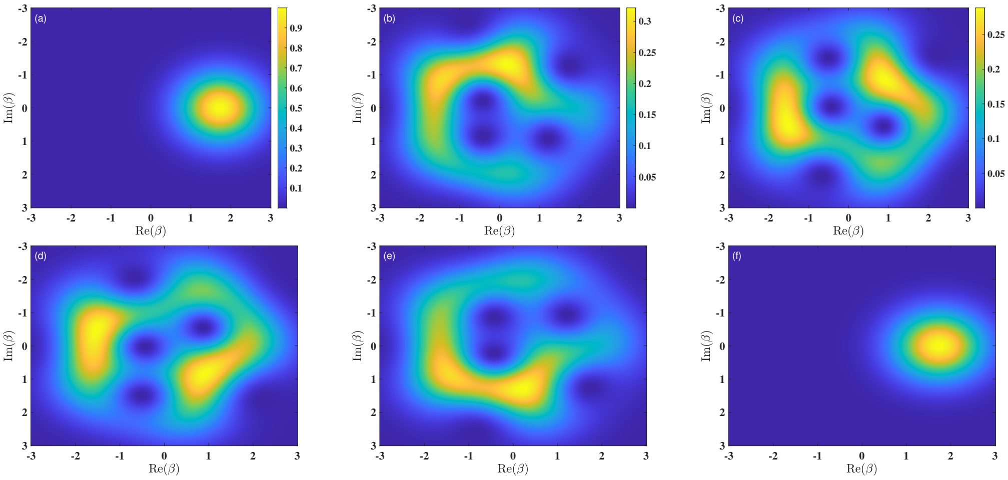

Fig. 3.1 Husimi function of the evolved coherent states for different times : (a) $Ut = 0$, (b) $Ut = 0.4\pi$, (c) $Ut = 0.8\pi$, (d) $Ut = 1.2\pi$, (e) $Ut = 1.6\pi$, (f) $Ut = 2\pi$. The initial condition is $\alpha = \sqrt{3}$. The cutoff for the particle number summation is $n = 20$. The system parameters are the same as in [44].

It is worth noting that when $Ut = \pi$ displayed in Fig. 3.2, the evolved state manifests as a superposition of two macroscopically distinguished states, also known as a Schrodinger cat state, which can be seen by splitting the sum in Eq. (3.2) into even and odd contributions

$$
\begin{aligned}
\exp\left[-\mathrm{i}\frac{\pi}{2}\hat{n}(\hat{n}-1)\right]|\alpha\rangle &= \mathrm{e}^{-\frac{|\alpha|^2}{2}}\sum_{n=0}^{\infty}\frac{\alpha^n}{\sqrt{n!}}\mathrm{e}^{-\mathrm{i}\frac{\pi}{2}n(n-1)}|n\rangle \\
&= \mathrm{e}^{-\frac{|\alpha|^2}{2}}\sum_{n=0,2,\ldots}^{\infty}\frac{(\alpha\mathrm{e}^{\mathrm{i}\frac{\pi}{2}})^n}{\sqrt{n!}}\mathrm{e}^{-\mathrm{i}\frac{\pi}{2}n^2}|n\rangle \\
&+ \mathrm{e}^{-\frac{|\alpha|^2}{2}+\mathrm{i}\frac{\pi}{2}}\sum_{n=1,3,\ldots}^{\infty}\frac{(\alpha\mathrm{e}^{\mathrm{i}\frac{\pi}{2}})^n}{\sqrt{n!}}\mathrm{e}^{-\mathrm{i}\frac{\pi}{2}(n-1)^2-\mathrm{i}\pi n}|n\rangle \\
&= \mathrm{e}^{-\frac{|\alpha|^2}{2}}\sum_{n=0,2,\ldots}^{\infty}\frac{(\alpha\mathrm{e}^{\mathrm{i}\frac{\pi}{2}})^n}{\sqrt{n!}}|n\rangle + \mathrm{i}\mathrm{e}^{-\frac{|\alpha|^2}{2}}\sum_{n=1,3,\ldots}^{\infty}\frac{(\alpha\mathrm{e}^{-\mathrm{i}\frac{\pi}{2}})^n}{\sqrt{n!}}|n\rangle. \qquad (3.4)
\end{aligned}
$$

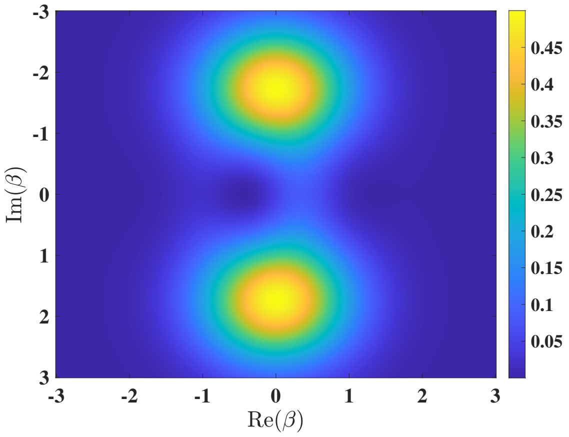

Fig. 3.2 Schrödinger cat state for $Ut = \pi$.

3.2 Two-point correlation function

Another quantity we pay attention to is the two-point correlation function. The analytical results to be derived for the cases of Glauber CS and GCS provide an insight for the connection between these two states. Moreover, this quantity is also the key to calculate the population distribution in quasi-momentum space as shown below. We emphasize that the primary work in this section is to revisit the results from [45], as their findings offer a comprehensive understanding of the relationship between Glauber CS and GCS. We also provide a more concise derivation for the case of GCS than the one in [45], by using some of the properties listed in Table. 2.1.

In the deep-lattice case, the two-point correlation function of Glauber CS can be derived as follows:

$$
\begin{aligned}
\langle\vec{\alpha}|\mathrm{e}^{\mathrm{i}\hat{H}t}\hat{a}_i^\dagger\hat{a}_j\mathrm{e}^{-\mathrm{i}\hat{H}t}|\vec{\alpha}\rangle &= \langle\alpha_i|\langle\alpha_j|\mathrm{e}^{\mathrm{i}(\hat{h}_i+\hat{h}_j)t}\hat{a}_i^\dagger\hat{a}_j\mathrm{e}^{-\mathrm{i}(\hat{h}_i+\hat{h}_j)t}|\alpha_i\rangle|\alpha_j\rangle \\
&= \langle\alpha_i|\mathrm{e}^{\mathrm{i}\hat{h}_it}\hat{a}_i^\dagger\mathrm{e}^{-\mathrm{i}\hat{h}_it}|\alpha_i\rangle\langle\alpha_j|\mathrm{e}^{\mathrm{i}\hat{h}_jt}\hat{a}_j\mathrm{e}^{-\mathrm{i}\hat{h}_jt}|\alpha_j\rangle \\
&= \langle\alpha_i|\hat{a}_i^\dagger\mathrm{e}^{\mathrm{i}U\hat{n}_it}|\alpha_i\rangle\langle\alpha_j|\mathrm{e}^{-\mathrm{i}U\hat{n}_jt}\hat{a}_j|\alpha_j\rangle \\
&= \alpha_i^*\alpha_j\langle\alpha_i|\alpha_i\mathrm{e}^{\mathrm{i}Ut}\rangle\langle\alpha_j|\alpha_j\mathrm{e}^{-\mathrm{i}Ut}\rangle \\
&= \alpha_i^*\alpha_j\exp\left[|\alpha_i|^2(\mathrm{e}^{\mathrm{i}Ut}-1)\right]\exp\left[|\alpha_j|^2(\mathrm{e}^{-\mathrm{i}Ut}-1)\right] \\
&= |\alpha|^2\mathrm{e}^{2|\alpha|^2[\cos(Ut)-1)]} \qquad (3.5)
\end{aligned}
$$

where in the third line, we have used the formulas $\hat{a}_kf(\hat{n}_k) = f(\hat{n}_k+1)\hat{a}_k$ and $\hat{a}_k^\dagger f(\hat{n}_k) = f(\hat{n}_k-1)\hat{a}_k^\dagger$, and we obtain the result in the fourth line via the fact

$$
\mathrm{e}^{\mathrm{i}\varphi\hat{n}_k}|\alpha_k\rangle = \sum_{n=0}^{\infty}\frac{\alpha_k^n}{\sqrt{n!}}\mathrm{e}^{\mathrm{i}\varphi n}|n\rangle_k = |\alpha_k\mathrm{e}^{\mathrm{i}\varphi}\rangle. \qquad (3.6)
$$

For the last line, the system is assumed to be homogeneous: $\alpha_i = \alpha_j = \alpha$. From the final result, it is clear that the evolution of the correlation function is also driven by the on-site interaction effect, exhibiting a periodic behavior with a period of $2\pi/U$.

We can also choose the GCS defined in Eq. (2.1) as the initial state. Physically, this choice appears more reasonable compared to the Glauber CS, given the fact that the ground state of the free boson system (only the hopping term is present, see Chapter. 4) with a finite number of particles is described by a GCS. This particular setup corresponds to a quench dynamics: the lattice is initially shallow where particles can move freely among different sites, and the system is prepared in the ground state. At $t = 0$ the lattice is abruptly deepened as shown schematically in Fig. 3.3, so the initial state which is no longer an eigenstate will start to evolve.

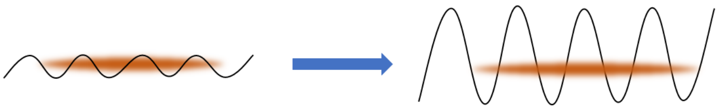

Fig. 3.3 Transition from the shallow lattice (almost free boson model) to deep lattice (on-site interaction only).

The time-evolved two-point correlation function of evolved GCS is derived as follows:

$$\begin{aligned}
\langle S,\vec{\xi}|\mathrm{e}^{\mathrm{i}\hat{H}t}\hat{a}_i^\dagger\hat{a}_j\mathrm{e}^{-\mathrm{i}\hat{H}t}|S,\vec{\xi}\rangle &= \langle S,\vec{\xi}|\mathrm{e}^{\mathrm{i}(\hat{h}_i+\hat{h}_j)t}\hat{a}_i^\dagger\hat{a}_j\mathrm{e}^{-\mathrm{i}(\hat{h}_i+\hat{h}_j)t}|S,\vec{\xi}\rangle \\
&= \langle S,\vec{\xi}|\hat{a}_i^\dagger\mathrm{e}^{\mathrm{i}U\hat{n}_it}\mathrm{e}^{-\mathrm{i}U\hat{n}_jt}\hat{a}_j|S,\vec{\xi}\rangle \\
&= S\xi_i^*\xi_j\langle S-1,\vec{\xi}|\mathrm{e}^{\mathrm{i}U\hat{n}_it}\mathrm{e}^{-\mathrm{i}U\hat{n}_jt}|S-1,\vec{\xi}\rangle \\
&= S\xi_i^*\xi_j\Big(|\xi_i|^2\mathrm{e}^{\mathrm{i}Ut}+|\xi_j|^2\mathrm{e}^{-\mathrm{i}Ut}+\sum_{k\neq i,j}^{M}|\xi_k|^2\Big)^{S-1}, \qquad (3.7)
\end{aligned}$$

where we have used the intermediate result

$$\begin{aligned}
\mathrm{e}^{\mathrm{i}\varphi\hat{n}_k}|S,\vec{\xi}\rangle &= \mathrm{e}^{\mathrm{i}\varphi\hat{n}_k}\frac{1}{\sqrt{S!}}\Big(\sum_{i=1}^{M}\xi_i\hat{a}_i^\dagger\Big)^S|\mathrm{vac}\rangle \\
&= \sum_{[n_i]=S}\frac{\sqrt{S!}}{n_1!n_2!\cdots n_M!}(\xi_1\hat{a}_1^\dagger)^{n_1}\cdots(\xi_k\mathrm{e}^{\mathrm{i}\varphi}\hat{a}_k^\dagger)^{n_k}\cdots(\xi_M\hat{a}_M^\dagger)^{n_M}\mathrm{e}^{\mathrm{i}\varphi(\hat{n}_k+n_k)}|\mathrm{vac}\rangle \\
&= |S,\vec{\xi}'\rangle \qquad (3.8)
\end{aligned}$$

where $\vec{\xi}'=\{\xi_1,\xi_2,\cdots,\xi_k\mathrm{e}^{\mathrm{i}\varphi},\cdots,\xi_M\}$, $\langle S,\vec{\xi}|S,\vec{\xi}'\rangle=\big(|\xi_k|^2\mathrm{e}^{\mathrm{i}\varphi}+\sum_{i\neq k}^{M}|\xi_i|^2\big)^S$. This result illustrates that the time effect of the number operator $\hat{n}_j$ is to imprint a phase factor on the j-th site, similar to the case of Glauber CS displayed in Eq. (3.6). We note that the result in Eq. (3.7) can also be obtained with the help of projection operator techniques [45].
For the special case where $i=j$, the correlation function simplifies to

$$\begin{aligned}
\langle S,\vec{\xi}|\mathrm{e}^{\mathrm{i}\hat{H}t}\hat{a}_i^\dagger\hat{a}_i\mathrm{e}^{-\mathrm{i}\hat{H}t}|S,\vec{\xi}\rangle &= \langle S,\vec{\xi}|\mathrm{e}^{\mathrm{i}\hat{h}_it}\hat{a}_i^\dagger\hat{a}_i\mathrm{e}^{-\mathrm{i}\hat{h}_it}|S,\vec{\xi}\rangle \\
&= \langle S,\vec{\xi}|\hat{a}_i^\dagger\hat{a}_i|S,\vec{\xi}\rangle \\
&= S|\xi_i|^2 \qquad (3.9)
\end{aligned}$$

For simplicity, let's move to the homogeneous state $\xi_1=\xi_2=\cdots=\xi_M=\frac{1}{\sqrt{M}}$ which corresponds to the zero quasi-momentum state of Eq. (2.14). Under this condition, the correlation function Eq. (3.7) simplifies to

$$\langle\hat{a}_i^\dagger\hat{a}_j\rangle=\frac{S}{M}\left[1+\frac{2}{M}\cos(Ut)-\frac{2}{M}\right]^{S-1} \qquad (3.10)$$

In the thermodynamic limit, defined just before Eq. (2.44), Eq. (3.7) converges to

$$\begin{aligned}\lim_{S\to\infty}\langle \hat{a}_i^\dagger \hat{a}_j\rangle &= \lim_{S\to\infty}\frac{S}{M}\left[1+\frac{S}{M}\frac{2}{S}\cos(Ut)-\frac{S}{M}\frac{2}{S}\right]^{S-1}\\ &= \frac{S}{M}\mathrm{e}^{\frac{S}{M}[-2+2\cos(Ut)]}. \end{aligned} \tag{3.11}$$

The similarity between Eq. (3.5) and Eq. (3.11) reveals that the relationship between Glauber CS and GCS can be established by setting $\alpha=\lambda=\frac{S}{M}$, which is also corroborated by Eq. (2.21). This demonstrates that the correlation function of GCS is identical to that of the Glauber CS in the thermodynamic limit. As proved in [45] and also reproduced in Fig. 3.4, this identity is achieved already for rather small values of S.

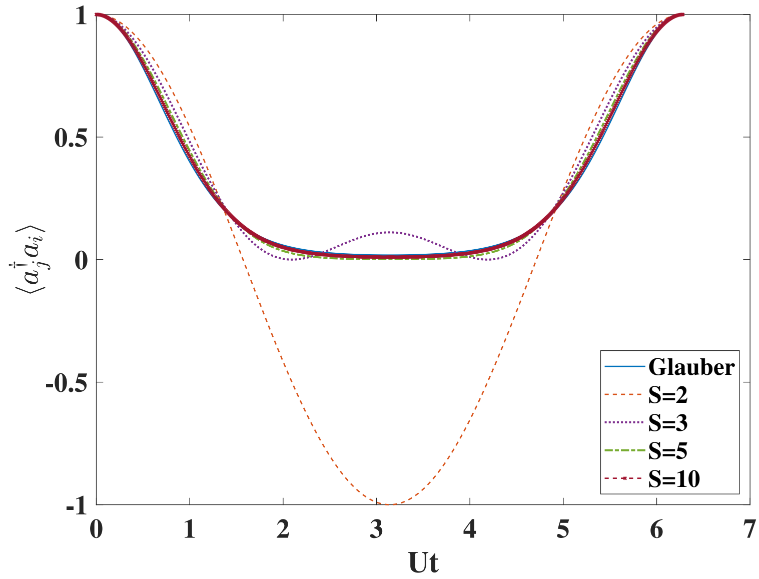

Fig. 3.4 Evolution of the two-point correlation function. The blue line stands for the result given by Eq (3.5) for $\alpha=1$. Other lines are from Eq. (3.11) with different particle numbers $S=M=2,3,5,10$.

Furthermore, the quasi-momentum distribution can be obtained through a summation over two-point correlation functions. Using Eq. (2.13), the distribution for a quasi-momentum k is given by

$$n_k(t)=\frac{1}{M}\sum_{i,j}^{M}\langle \hat{a}_i^\dagger \hat{a}_j\rangle \mathrm{e}^{\mathrm{i}k(i-j)a}=\frac{S}{M^2}\mathrm{e}^{\frac{S}{M}[-2+2\cos(Ut)]}\sum_{i,j}^{M}\mathrm{e}^{\mathrm{i}k(i-j)a} \tag{3.12}$$

where the k takes the values $-\frac{\pi}{a}, -\frac{\pi}{a}+\frac{2\pi}{Ma}, \cdots, \frac{\pi}{a}$. In Fig. 3.5, we present the periodical time evolution of the distribution of each quasi-momentum. The initial state is condensed into zero momentum and the short time evolution presents a sharp distribution around zero momentum. After $Ut = \frac{\pi}{2}$, the distribution is broadened over the entire momentum range. Subsequently, the distribution gradually reconverges to zero again after $Ut = \frac{3\pi}{2}$. The reason can be explained by Eq. (3.12) as follows: when the value of $\cos(Ut)$ is below zero, which corresponds to the time region $Ut = [\frac{\pi}{2}, \frac{3\pi}{2}]$, the exponent in Eq. (3.12) is decreased rapidly. As a result, the distribution gets smeared out in this time region.

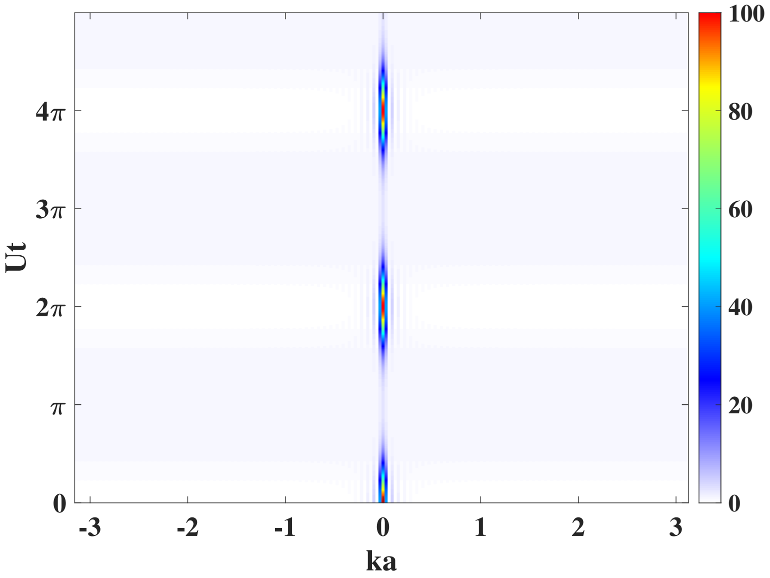

Fig. 3.5 Quasi-momentum distribution as a function of time. Ut is from 0 to 5π, and ka varies in the region $-\pi$ to π. The system size is $S = M = 100$. The same figure can also be found in [45].

3.3 Autocorrelation function of the evolved GCS

Although GCS and Glauber CS share some similarities, differences between them still exist in some aspects of their behavior. To prove that, we will investigate the time-dependent survival probability of the GCS in the subsequent part of this section and compare the results with those for the Glauber CS.

3.3.1 Exact solution for autocorrelation function

The first step in this comparison is to explicitly calculate the time evolution of the GCS driven by the interaction (as defined in Eq. 3.1), which can be derived as follows:

$$
\begin{aligned}
\mathrm{e}^{-\mathrm{i}\hat{H}t}|S,\vec{\xi}\rangle &= \mathrm{e}^{-\mathrm{i}\left(\sum_{i=1}^{M}\hat{h}_i\right)t}\frac{1}{\sqrt{S!}}\left(\sum_{i=1}^{M}\xi_i\hat{a}_i^{\dagger}\right)^{S}|\mathrm{vac}\rangle \\
&= \sqrt{S!}\sum_{[n_i]=S}\prod_{i=1}^{M}\frac{1}{n_i!}\mathrm{e}^{-\mathrm{i}\hat{h}_i t}(\xi_i\hat{a}_i^{\dagger})^{n_i}|\mathrm{vac}\rangle \\
&= \sqrt{S!}\sum_{[n_i]=S}\prod_{i=1}^{M}\frac{1}{n_i!}(\xi_i\hat{a}_i^{\dagger})^{n_i}\mathrm{e}^{-\mathrm{i}\frac{U}{2}(\hat{n}_i+n_i)(\hat{n}_i+n_i-1)t}|\mathrm{vac}\rangle \\
&= \sqrt{S!}\sum_{[n_i]=S}\prod_{i=1}^{M}\frac{1}{n_i!}\left[\xi_i\mathrm{e}^{-\mathrm{i}\frac{U}{2}(n_i-1)t}\hat{a}_i^{\dagger}\right]^{n_i}|\mathrm{vac}\rangle \\
&= \sqrt{S!}\sum_{[n_i]=S}\mathrm{e}^{\mathrm{i}\frac{U}{2}St}\prod_{i=1}^{M}\frac{1}{n_i!}\left(\xi_i\mathrm{e}^{-\mathrm{i}\frac{U}{2}n_i t}\hat{a}_i^{\dagger}\right)^{n_i}|\mathrm{vac}\rangle \\
&= \sqrt{S!}\sum_{[n_i]=S}\prod_{i=1}^{M}\frac{1}{n_i!}\left(\xi_i\mathrm{e}^{-\mathrm{i}\frac{U}{2}n_i t}\hat{a}_i^{\dagger}\right)^{n_i}|\mathrm{vac}\rangle,
\end{aligned}
$$

where in the second line we expand the GCS in terms of the Fock states as shown in Eq. (2.6) and apply the factorized operator $\mathrm{e}^{-\mathrm{i}\hat{h}_i t}$ to the corresponding mode. In the third line we utilize the formula

$$\hat{a}_i^{\dagger}f(\hat{n}_i) = f(\hat{n}_i+1)\hat{a}_i^{\dagger}. \tag{3.13}$$

The result in the fourth line is given by the fact that

$$\mathrm{e}^{-\mathrm{i}\frac{U}{2}(\hat{n}_i+n_i)(\hat{n}_i+n_i-1)t}|\mathrm{vac}\rangle = \mathrm{e}^{-\mathrm{i}\frac{U}{2}n_i(n_i-1)t}|\mathrm{vac}\rangle, \tag{3.14}$$

and the global phase factor $\mathrm{e}^{\mathrm{i}\frac{U}{2}St}$ in the second last line stems from $\mathrm{e}^{\mathrm{i}\frac{U}{2}St} = \prod_{i=1}^{M}\mathrm{e}^{\mathrm{i}\frac{U}{2}n_i t}$. The autocorrelation function which is also called Loschmidt amplitude [46] is given by

$$\langle S,\vec{\xi}|\mathrm{e}^{-\mathrm{i}\hat{H}t}|S,\vec{\xi}\rangle = S!\sum_{[n_i]=S}\prod_{i=1}^{M}\frac{|\xi_i|^{2n_i}}{n_i!}\mathrm{e}^{-\mathrm{i}\frac{U}{2}n_i^2 t} \tag{3.15}$$

where the orthogonality of the Fock states is used. This result is distinct from the Glauber CS result

$$\begin{aligned}\langle\vec{\alpha}|\mathrm{e}^{-\mathrm{i}\hat{H}t}|\vec{\alpha}\rangle &= \otimes_{i=1}^{M}\langle\alpha_i|\exp(-\mathrm{i}\hat{h}_i t)|\alpha_i\rangle \\ &= \prod_{i=1}^{M}\mathrm{e}^{-|\alpha_i|^2}\sum_{n_i=0}^{\infty}\frac{|\alpha_i|^{2n_i}}{n_i!}\mathrm{e}^{-\mathrm{i}\frac{U}{2}n_i(n_i-1)t}. \end{aligned}\tag{3.16}$$

Notably, the expression for Glauber CS is factorized and does not impose constraints on the total number of particles.

The summation in Eq. (3.15) has no obvious closed solution for $U \neq 0$. However, the numerical solution is accessible via the concept of generating functions [47] that allows for a relatively straightforward evaluation of the restricted summation in Eq. (3.15), which would otherwise be impossible to tackle, already for moderate particle and site numbers. The general idea of the generating function method is to design a polynomial in the variable x with the constraint that the coefficient for the term x^S is related to Eq. (3.15). This method turns the problem into calculating the polynomial coefficients which can be done by efficient convolution algorithm. For instance, if the generating function is the product of two polynomials, represented as $\left(\sum_{i=1}^{\infty} a_i x^i\right)\left(\sum_{j=1}^{\infty} b_j x^j\right)$, the coefficient in front of the x^n can be expressed as

$$\sum_{i=1}^{\infty} a_i b_{n-i} \tag{3.17}$$

which is the convolution between two series $\{a_i\}$ and $\{b_i\}$.

Let's first consider the homogeneous situation $\xi_1 = \xi_2 = \cdots = \xi_M = \frac{1}{\sqrt{M}}$, simplifying Eq. (3.15) to

$$\langle S,\vec{\xi}|\mathrm{e}^{-\mathrm{i}\hat{H}t}|S,\vec{\xi}\rangle = \frac{S!}{M^S}\sum_{[n_i]=S}\prod_{i=1}^{M}\frac{1}{n_i!}\mathrm{e}^{-\mathrm{i}\frac{U}{2}n_i^2 t} \tag{3.18}$$

We define a polynomial

$$F(x) = \left[\sum_{k=0}^{M}\phi(k)x^k\right]^M, \qquad \phi(k) = \frac{\mathrm{e}^{-\mathrm{i}\frac{U}{2}k^2 t}}{k!} \tag{3.19}$$

which plays the role of generating function, so the result in Eq. (3.18) is given by $\frac{S!}{M^S}[x^S]F(x)$, where $[x^S]F(x)$ denotes the coefficient for term x^S in the polynomial $F(x)$. In the general situation, a series of independent polynomials are needed

$$\tilde{F}(x) = f_1(x) f_2(x) \cdots f_M(x), \qquad f_i(x) = \sum_{k=0}^{M} \frac{|\xi_i|^{2k} \mathrm{e}^{-\mathrm{i}\frac{U}{2}k^2 t}}{k!} x^k \tag{3.20}$$

and Eq. (3.15) is given by $S![x^S]\tilde{F}(x)$.

3.3.2 Dynamical free energy density

Given the similarity between the autocorrelation function $\langle \psi(0) | \mathrm{e}^{-\mathrm{i}\hat{H}t} | \psi(0) \rangle$ and the partition function in equilibrium statistical mechanics

$$\mathrm{Z} = \mathrm{tr}(\mathrm{e}^{-\beta \hat{H}}) = \mathrm{e}^{-\beta N f} \tag{3.21}$$

where β is the inverse of temperature, N denotes the number of degrees of freedom and f is the free-energy density, a set of counterparts in the realm of non-equilibrium statistics are introduced to understand a possible phase transition in the quantum dynamics [48].

In Fig. 3.6, we study the evolution of the dynamical free-energy density, the dynamical analog of the free energy density f, which is defined by

$$\mathscr{L} \equiv -\frac{1}{M} \log(|\langle \psi(0) | \psi(t) \rangle|^2) \tag{3.22}$$

where the initial state in our case

$$|\psi(0)\rangle = |S, \vec{\xi}\rangle \tag{3.23}$$

is the GCS with homogeneous parameters, and the survival probability $|\langle \psi(0) | \psi(t) \rangle|^2$ is thus solvable via Eq. (3.18). We fix the value of the particle number to $S = 100$ and vary the ratio $\lambda = \frac{S}{M}$ to investigate the dynamics. From Fig. 3.6, we can observe that for large values of λ, the dynamical free-energy density has several peaks within one period. As λ is decreased, these peaks gradually disappear, leaving just one peak occurring at $Ut = \pi$ when $\lambda = 0.5$. Due to the definition of the dynamical free-energy density in Eq. (3.22), these peaks correspond to the minimal values of the survival probability. When the survival probability completely vanishes, non-analytical kinks appear in the curves. This phenomenon is recognized as a quantum dynamical phase transition (QDPT) in the literature [49–51]. The authors in [46] have studied the QDPT of the non-equilibrium dynamics induced by the quench from the superfluid phase to the Mott-insulator phase present in the full Bose-Hubbard model, to be introduced in Chapter. 4.

In order to gain some understanding of the peak structure seen in Fig. 3.6, we will now

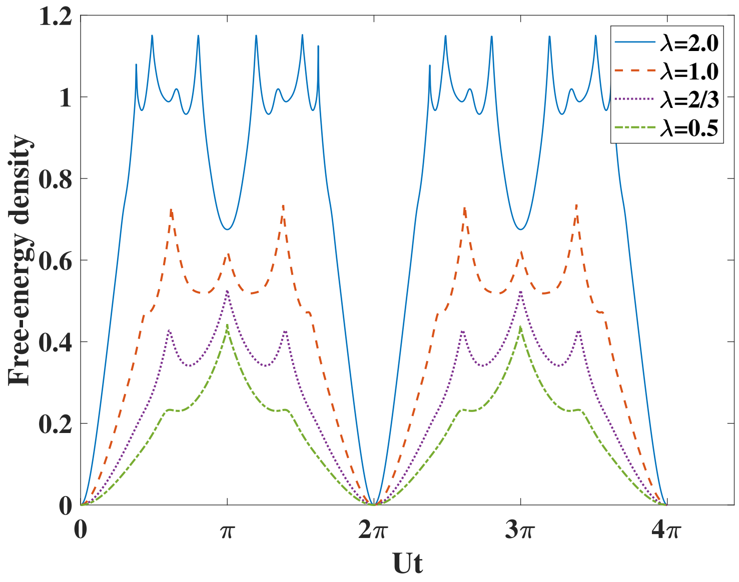

Fig. 3.6 Free-energy density as a function of time Ut which ranges from 0 to 4π. The total number of particles is fixed to be $S = 100$, and results are shown for different values of $\lambda = S/M$

.

elucidate the connection of the survival probability with the Glauber CS's case. First we rewrite Eq. (3.18) as follows:

$$
\begin{aligned}
\langle S,\vec{\xi}|\mathrm{e}^{-\mathrm{i}\hat{H}t}|S,\vec{\xi}\rangle &= S! \sum_{[n_i]=S}\prod_{i=1}^{M}\frac{1}{n_i!}\frac{1}{M^{n_i}}\mathrm{e}^{-\mathrm{i}\frac{U}{2}n_i(n_i-1)t} \\
&= S! \sum_{n_1=0}^{\infty}\sum_{n_2=0}^{\infty}\cdots\sum_{n_M=0}^{\infty}\delta_{S,\sum_{i=1}^{M}n_i}\prod_{i=1}^{M}\frac{1}{n_i!}\frac{1}{M^{n_i}}\mathrm{e}^{-\mathrm{i}\frac{U}{2}n_i(n_i-1)t} \\
&= S! \sum_{n_1=0}^{\infty}\sum_{n_2=0}^{\infty}\cdots\sum_{n_M=0}^{\infty}\int_0^1 \mathrm{d}x\mathrm{e}^{-\mathrm{i}2\pi x(S-\sum_{i=1}^{M}n_i)}\prod_{i=1}^{M}\frac{1}{n_i!}\frac{1}{M^{n_i}}\mathrm{e}^{-\mathrm{i}\frac{U}{2}n_i(n_i-1)t} \\
&= S! \sum_{n_1=0}^{\infty}\sum_{n_2=0}^{\infty}\cdots\sum_{n_M=0}^{\infty}\int_0^1 \mathrm{d}x\mathrm{e}^{-\mathrm{i}2\pi xS}\prod_{i=1}^{M}\frac{1}{n_i!}\frac{1}{M^{n_i}}\mathrm{e}^{-\mathrm{i}\frac{U}{2}n_i(n_i-1)t+\mathrm{i}2\pi x n_i} \\
&= S! \int_0^1 \mathrm{d}x\mathrm{e}^{-\mathrm{i}2\pi xS}\left(\sum_{n=0}^{\infty}\frac{1}{n!}\frac{1}{M^n}\mathrm{e}^{-\mathrm{i}\frac{U}{2}n(n-1)t+\mathrm{i}2\pi xn}\right)^M \\
&= \frac{S!}{S^S}\int_0^1 \mathrm{d}x\mathrm{e}^{-\mathrm{i}2\pi xS}\left(\sum_{n=0}^{\infty}\frac{1}{n!}\frac{S^n}{M^n}\mathrm{e}^{-\mathrm{i}\frac{U}{2}n(n-1)t+\mathrm{i}2\pi xn}\right)^M
\end{aligned}
\tag{3.24}
$$

where in the first line, the global phase factor $\mathrm{e}^{\mathrm{i}\frac{U}{2}St} = \mathrm{e}^{\mathrm{i}\frac{U}{2}\sum_{i=1}^{M}n_i t}$ is incorporated again in order to compare with the Glauber CS case. In the second line the Kronecker function $\delta_{S,\sum_{i=1}^{M}n_i}$

is introduced to impose the constraint on the total particle number and meanwhile lift the restriction on the particle number of the single mode. The third line is reached by replacing the Kronecker function with an integral

$$\delta_{S,\sum_{i=1}^{M} n_i} = \int_0^1 \mathrm{d}x \mathrm{e}^{-\mathrm{i}2\pi x(S-\sum_{i=1}^{M} n_i)}. \tag{3.25}$$

Furthermore, by incorporating the factor $\frac{S!}{S^S}$ into the bracket, we are able to define a function $G(x,t)$

$$G(x,t) = \left[\sum_{n=0}^{\infty} \frac{1}{n!}\left(\frac{S!}{S^S}\right)^{1/M} \frac{S^n}{M^n} \mathrm{e}^{-\mathrm{i}\frac{U}{2}n(n-1)t+\mathrm{i}2\pi xn}\right]^M \tag{3.26}$$

Considering the large number of particle limit, we are able to use Stirling's approximation $S! \approx \sqrt{2\pi S}(\frac{S}{\mathrm{e}})^S$ of the factorial to simplify the factor $\left(\frac{S!}{S^S}\right)^{1/M}$ as

$$\left(\frac{S!}{S^S}\right)^{1/M} \approx \sqrt[2M]{2\pi S}\left(\frac{S}{S\mathrm{e}}\right)^{\frac{S}{M}} = \sqrt[2M]{2\pi S}\mathrm{e}^{-\lambda}, \tag{3.27}$$

Combining Eq. (3.24), Eq. (3.26) and Eq. (3.27), we have

$$\langle S,\vec{\xi}|\mathrm{e}^{-\mathrm{i}\hat{H}t}|S,\vec{\xi}\rangle = \sqrt{2\pi S}\int_0^1 \mathrm{d}x\mathrm{e}^{-\mathrm{i}2\pi xS}G(x,t) \tag{3.28}$$

where the $G(x,t)$ is expressed as

$$G(x,t) = \left[\sum_{n=0}^{\infty} \frac{\lambda^n \mathrm{e}^{-\lambda}}{n!} \mathrm{e}^{-\mathrm{i}\frac{U}{2}n(n-1)t+\mathrm{i}2\pi xn}\right]^M. \tag{3.29}$$

Inspired by the form of Eq. (3.28), we can interpret the survival probability amplitude of the evolved GCS as the Fourier coefficient of $G(x,t)$ at a specific "frequency" denoted by S. The function $G(x,t)$ has the exact meaning of the overlap between two coherent states $\langle\vec{\alpha}'|\mathrm{e}^{-\mathrm{i}\hat{H}t}|\vec{\alpha}\rangle$ where $|\vec{\alpha}\rangle$ is a multimode Glauber CS with $\alpha_i = \sqrt{\lambda}$ for $\forall i$, and $|\vec{\alpha}'\rangle$ is a similar CS with a phase shift characterized by

$$\alpha_j' = \sqrt{\lambda}\mathrm{e}^{-\mathrm{i}2\pi x} \tag{3.30}$$

for $\forall j$ with

$$0 \le x < 1. \tag{3.31}$$

Despite the phase shift, $|\vec{\alpha}\rangle$ and $|\vec{\alpha}'\rangle$ are expanded by the same GCS as discussed below Eq. (2.21). Essentially, this phase shift is rooted in the $U(1)$ symmetry of GCS which Glauber CS does not follow. Another significant insight gained from Eq. (3.28) is that if the value of $G(x,t)$ is zero, the survival probability will consequently be zero as well.

The case of the thermodynamic limit

Particularly, let's consider the case of unit filling factor $\lambda = 1$ which corresponds to the thermodynamic limit when S and M are large. In this case, the function

$$G(x,t) = \left[\sum_{n=0}^{\infty} \frac{\mathrm{e}^{-1}}{n!} \mathrm{e}^{-\mathrm{i}\frac{U}{2}n(n-1)t + \mathrm{i}2\pi xn} \right]^M \tag{3.32}$$

represents the overlap function of $\mathrm{e}^{-\mathrm{i}\hat{H}t}|\vec{\alpha}\rangle$ with the CS distributed along the unit circle due to $\alpha = \lambda = 1$ in phase space.

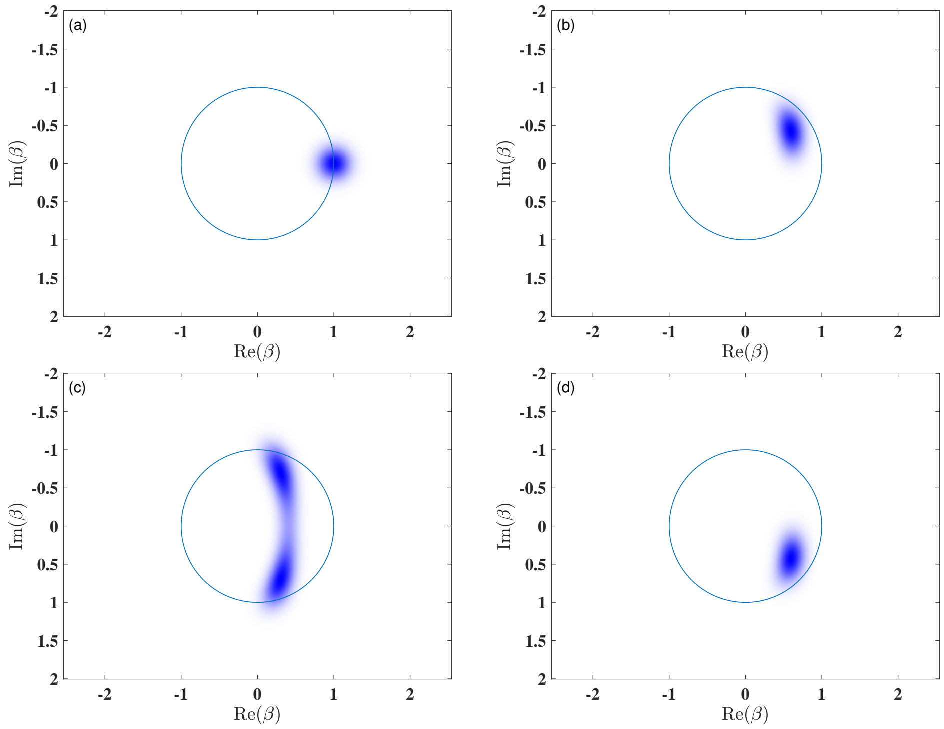

Fig. 3.7 The distribution function $|\langle\beta|\mathrm{e}^{-\mathrm{i}\hat{H}t}|\alpha\rangle|^M$ in phase space $(\mathrm{Re}(\beta), \mathrm{Im}(\beta))$ at different time points: (a) $Ut = 0$, (b) $Ut = \frac{\pi}{2}$, (c) $Ut = \pi$ and (d) $Ut = \frac{3\pi}{2}$. The characteristic parameter of the CS is $\alpha = 1$ and the system parameter is $M = 50$. The colors range from white to dark blue, indicating an increase from low to high values of the function displayed.

In Fig. 3.7, we present the dynamics of the function $|\langle\beta|\mathrm{e}^{-\mathrm{i}\hat{H}t}|\alpha\rangle|^M$ for system size $S =$

$M = 50$. The value of $|G(x,t)|$ is determined by the distribution of $|\langle\beta|\mathrm{e}^{-\mathrm{i}\hat{H}t}|\alpha\rangle|^M$ on the unit circle. It can be inferred that this function similar with the Husimi function for $M = 1$ evolves around the unit circle, and the value of $|G(x,t)|$ is significantly influenced by the spot's relative position to the circle. Pictorially, when the circle does not intersect the spot, the survival probability vanishes, leading to the emergence of non-analytical kinks. Moreover, as M approaches infinity, the shape of the spot shrinks into a point, indicating that once the center of the point leaves the circle, the survival probability rapidly drops to zero.
Another noteworthy observation is the influence of the shape of the spot. For example, when λ is large the spot tends to split into two parts when $Ut = \pi$, possibly introducing extra intersections with the circle, as displayed in Fig. 3.7 (c), see also Fig. 3.2. Conversely, if λ is small such as the case $\lambda = \frac{2}{3}$, the spot will remain connected and the center remains distanced from the circle at $Ut = \pi$ displayed in Fig. 3.8, resulting in the gradual dominance of the central peak at $Ut = \pi$ for decreasing λ as shown in Fig. 3.6.

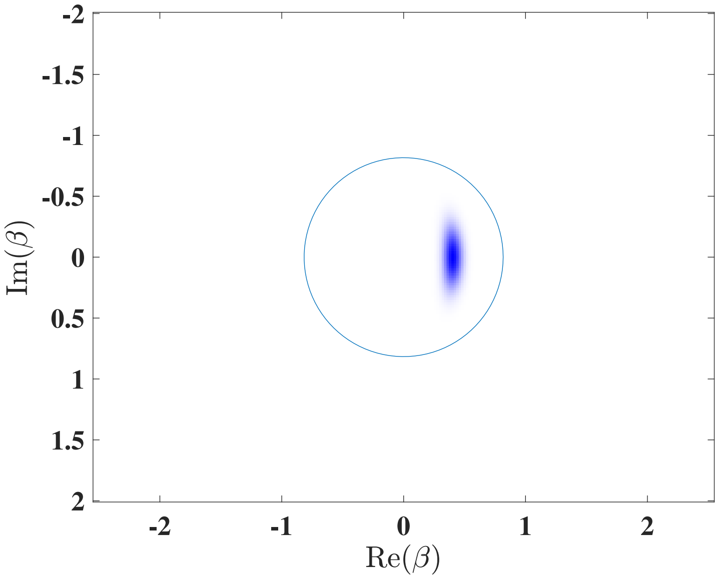

Fig. 3.8 The distribution function $|\langle\beta|\mathrm{e}^{-\mathrm{i}\hat{H}t}|\alpha\rangle|^M$ for $\lambda = \frac{2}{3}$ with $S = 100$ at $Ut = \pi$. The colors range from white to dark blue, indicating an increase from low to high values of the function displayed.

The case of large filling factor

Another noteworthy scenario occurs when $S \gg M$ where the Eq. (3.28) still holds. However, the underlying distribution in phase space and the corresponding free-energy density are much more complicated. Contrasted with the results in Fig. 3.6, the free-energy density in Fig. 3.9 for $S = 100$ and $M = 3$ contains more peaks, especially two pronounced spikes located around $x = 2.074$ and $x = 4.2$ within the first period. These peaks are associated with the local or global minimal values of the survival probability.

In Fig. 3.10, the corresponding distribution function $|\langle\beta|\mathrm{e}^{-\mathrm{i}\hat{H}t}|\alpha\rangle|^M$ for $\alpha = \sqrt{\lambda} = \sqrt{\frac{100}{3}}$ is depicted. This distribution splits into several spots which form multi-component cat states at different time slices, and all of their centers move along the circle with radius $\sqrt{\lambda}$, as the quantum fluctuation of the Glauber CS with large α is suppressed. Consequently, the vanishing of the survival probability can not be attributed to the deviation of $G(x,t)$ from the circle.

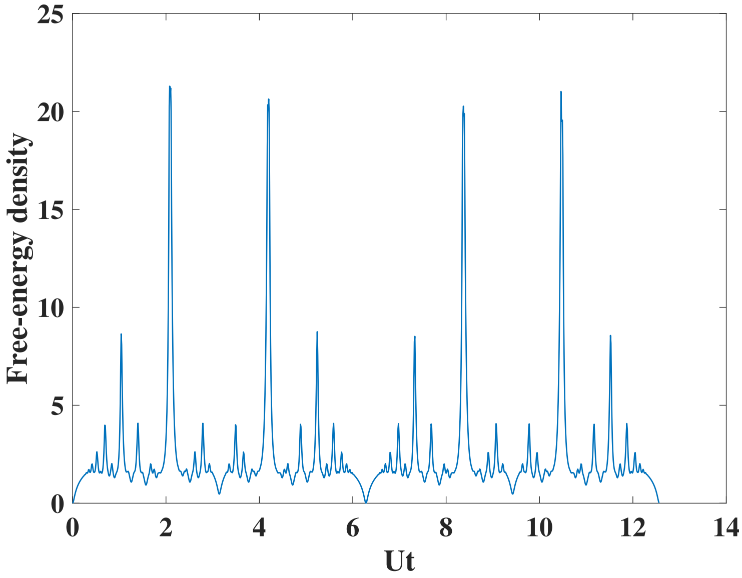

Fig. 3.9 Free-energy density as a function of time Ut ranging from 0 to 4π. The system size is set to be $S = 100$ and $M = 3$.

Instead, we should examine the integrand on the right hand side of Eq. (3.28)

$$F(x,t) = \mathrm{e}^{-\mathrm{i}2\pi xS}G(x,t). \tag{3.33}$$

In Fig. 3.11, we divide the $F(x,t)$ into real and the imaginary parts, and choose two typical time slices to observe how they vary with x ranging from 0 to 1. In the left figure, the time is fixed at $Ut = \frac{\pi}{2}$ corresponding to Fig. 3.10 (d) where the four spots manifest as four peaks. Because three peaks are negative and one is positive, all of them displaying similar heights, the integral of the real part with respect to the x is not zero resulting in a finite survival probability. In the right figure, however, the time is selected to be $Ut = 2.074$ identical with the position of the first main spike in Fig. 3.9. In this case, the integral of both real and imaginary components is very small, since the peaks manifest as either positive or negative.

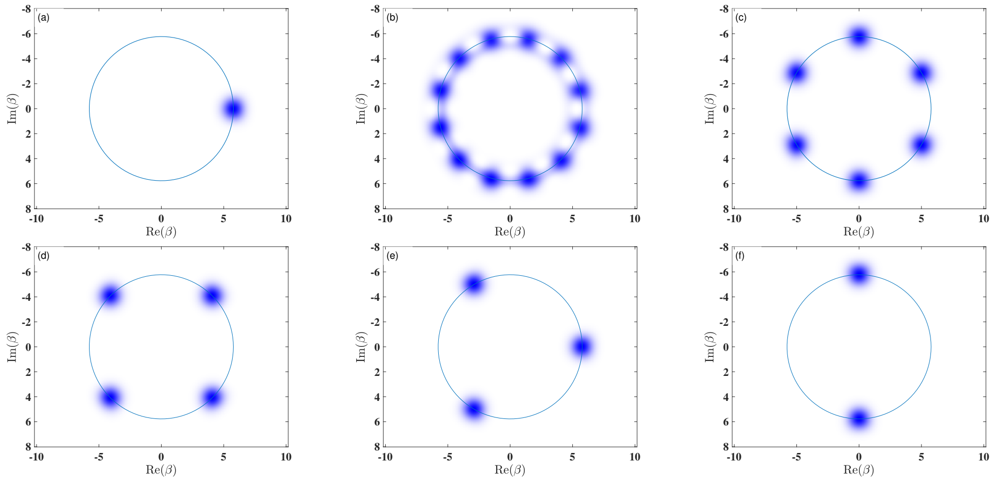

Fig. 3.10 The distribution function $|\langle\beta|\mathrm{e}^{-\mathrm{i}\hat{H}t}|\alpha\rangle|^M$ with $M=3$ in phase space $(\mathrm{Re}(\beta),\mathrm{Im}(\beta))$ at different time points: (a) $Ut=0$, (b) $Ut=\frac{\pi}{6}$, (c) $Ut=\frac{2\pi}{6}$, (d) $Ut=\frac{3\pi}{6}$, (e) $Ut=\frac{4\pi}{6}$ and (f) $Ut=\pi$,. The characteristic parameter of the CS is $\alpha=\sqrt{\frac{100}{3}}$ and the cutoff of the maximal particle number is set to be 50. The colors range from white to dark blue, indicating an increase from low to high values of the function displayed.

The contributions with opposing signs ultimately cancel each other out, giving rise to the vanishing of the overall integral. As a result, the survival probability will also be zero. In summary, when λ is large, the value of survival probability is a collective effect of all the spots.

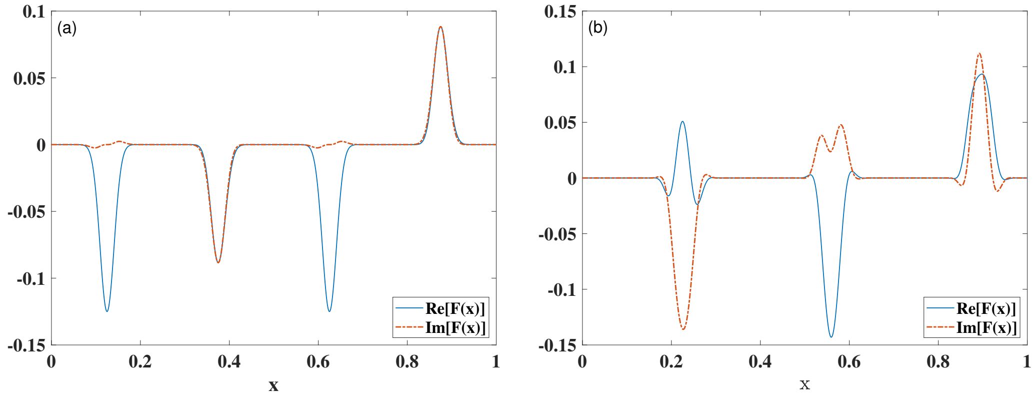

Fig. 3.11 The real part (solid blue) and the imaginary part (red dot-dash) of $F(x,t)$ as functions of x for two fixed time points: (a) $Ut=\frac{\pi}{2}$ and (b) $Ut=2.074$. The system parameters are the same as those in Fig. 3.10.

3.3.3 General Hamiltonian

The connection between the autocorrelations of the different types of CS can be generalized to a generic but number conserving Hamiltonian $\hat{H}$. To do that, we recall the Eq. (2.21), and the survival probability amplitude can be expanded as

$$\langle\vec{\alpha}|\mathrm{e}^{-\mathrm{i}\hat{H}t}|\vec{\alpha}\rangle = \mathrm{e}^{-\tilde{N}}\sum_{S'=0}^{\infty}\frac{\tilde{N}^{S'}}{S'!}\langle S',\vec{\xi}|\mathrm{e}^{-\mathrm{i}\hat{H}t}|S',\vec{\xi}\rangle. \tag{3.34}$$

The next step is to extract the term $\langle S',\vec{\xi}|\mathrm{e}^{-\mathrm{i}\hat{H}t}|S',\vec{\xi}\rangle$ from the sum. An enlightening way is to utilize the projection operator onto a specific particle number S, as defined in [45]

$$\hat{P} = \int_0^1 \mathrm{d}x\mathrm{e}^{\mathrm{i}2\pi x(S-\hat{N})} \tag{3.35}$$

where $\hat{N} = \sum_{i=1}^{M} a_i^{\dagger}\hat{a}_i$. It is clear that the operator $\hat{P}$ plays the role of $\delta_{S',S}$.
Applying the operator $\hat{P}$ to both sides of Eq. (3.34), we get

$$\begin{aligned}
&\int_0^1 \mathrm{d}x\mathrm{e}^{\mathrm{i}2\pi xS}\langle\vec{\alpha}|\mathrm{e}^{-\mathrm{i}2\pi x\hat{N}}\mathrm{e}^{-\mathrm{i}\hat{H}t}|\vec{\alpha}\rangle\\
&= \mathrm{e}^{-\tilde{N}}\int_0^1 \mathrm{d}x\mathrm{e}^{\mathrm{i}2\pi xS}\sum_{S'=0}^{\infty}\frac{\tilde{N}^{S'}}{S'!}\langle S',\vec{\xi}|\mathrm{e}^{-\mathrm{i}2\pi x\hat{N}}\mathrm{e}^{-\mathrm{i}\hat{H}t}|S',\vec{\xi}\rangle\\
&= \mathrm{e}^{-\tilde{N}}\frac{\tilde{N}^{S}}{S!}\langle S,\vec{\xi}|\mathrm{e}^{-\mathrm{i}\hat{H}t}|S,\vec{\xi}\rangle
\end{aligned} \tag{3.36}$$

which gives rise to the final result

$$\langle S,\vec{\xi}|\mathrm{e}^{-\mathrm{i}\hat{H}t}|S,\vec{\xi}\rangle = \mathrm{e}^{\tilde{N}}\frac{S!}{\tilde{N}^{S}}\int_0^1 \mathrm{d}x\mathrm{e}^{\mathrm{i}2\pi xS}\langle\vec{\alpha}\mathrm{e}^{\mathrm{i}2\pi x}|\mathrm{e}^{-\mathrm{i}\hat{H}t}|\vec{\alpha}\rangle \tag{3.37}$$

for the autocorrelation in complete analogy to Eq. (3.28), for the case of Hamiltonian (3.1). By setting $\tilde{N} = S$ and $\alpha_1 = \alpha_2 = \cdots = \sqrt{\frac{S}{M}}$, it can be verified that Eq. (3.37) will reproduce the Eq. (3.28)

$$\begin{aligned}\langle S,\vec{\xi}|\mathrm{e}^{-\mathrm{i}\hat{H}t}|S,\vec{\xi}\rangle &= \mathrm{e}^{\tilde{N}}\frac{S!}{\tilde{N}^S}\int_0^1 \mathrm{d}x\mathrm{e}^{-\mathrm{i}2\pi xS}\left[\mathrm{e}^{-|\alpha|^2}\sum_{n=0}^{\infty}\frac{|\alpha|^{2n}\mathrm{e}^{-\mathrm{i}2\pi xn}}{n!}\mathrm{e}^{-\mathrm{i}\frac{U}{2}n(n-1)t}\right]^M \\ &= \frac{S!}{\tilde{N}^S}\int_0^1 \mathrm{d}x\mathrm{e}^{-\mathrm{i}2\pi xS}\left[\sum_{n=0}^{\infty}\frac{|\alpha|^{2n}\mathrm{e}^{-\mathrm{i}2\pi xn}}{n!}\mathrm{e}^{-\mathrm{i}\frac{U}{2}n(n-1)t}\right]^M \\ &= \sqrt{2\pi S}\int_0^1 \mathrm{d}x\mathrm{e}^{-\mathrm{i}2\pi xS}\left[\sum_{n=0}^{\infty}\frac{\mathrm{e}^{-\lambda}\lambda^n\mathrm{e}^{-\mathrm{i}2\pi xn}}{n!}\mathrm{e}^{-\mathrm{i}\frac{U}{2}n(n-1)t}\right]^M \qquad (3.38)\end{aligned}$$

with the Hamiltonian Eq. (3.1). It remains to be seen if the general relation can be applied fruitfully in the future.

Chapter 4

Variational dynamics of multiple generalized coherent states

In modern quantum mechanics, the time-dependent dynamics of many-body systems is a long-standing problem due to the exponentially increasing Hilbert space even if the system size is only mildly increased. A lot of of effort has been put into this field to alleviate this difficulty, including dynamical mean-field theory, quantum Monte Carlo, time-dependent density matrix renormalization group, and exact diagonalization, etc. [52–55].

Another, however, less well-studied method is the time-dependent variational principle (TDVP). Its general idea is to employ tailored basis functions which contain a set of time-dependent variables, and the expansion in terms of these basis functions is assumed to be a good approximation of the exact solution. The next step is to derive the equations of motion of the variables that are governed by the variational principle, and from which we can obtain the evolution of the basis function. The core idea of TDVP is the selection of basis functions which heavily relies on the underlying Hamiltonian. In principle, a good selection can make the evolution stay in the dynamically important area and ease the problem dramatically. A typical example is the application of the Glauber CS in some physical situations, ranging from electron dynamics in atoms to nuclear dynamics in molecules as well as to non-adiabatic (combined electron-nuclear) motion, and the dynamics of the bath degrees of freedom in a spin boson model, as reviewed in [56–59, 28, 60, 61].

In the previous references, the well-studied molecular potentials, like the Morse potential and Henon-Heiles potential [60, 62], are close to the harmonic potential, where the Glauber CS provides an exact solution. Due to the overcompleteness of the Glauber CS, the CS based methods have attracted lots of attention in the last several decades. Besides, in [63], a generalization of the multi-configuration time-dependent Hartree method for bosons [64] based on McLachlan's variational principle has been given. The time-dependent variables used there are based on orthogonal orbitals, however. Most recently, the applications of TDVP in tensor networks has become a very promising direction as it can combine the advantages of both powerful tools [65–68].

4.1 Variational basis function based on Glauber CS

In previous applications of the variational method, the time evolution of the state vector for bosons is written as a linear combination of the multimode Glauber CS as follows

$$|\psi(t)\rangle = \sum_{k=1}^{N} A_k(t)|\vec{\alpha}_k(t)\rangle. \tag{4.1}$$

where N is the number of Glauber CS employed. The equations of motion of the coherent state parameters $\{\vec{\alpha}_k\}$, as well as of the coefficients A_k in the expansion of the wavefunction in terms of those states are usually derived from a variational principle and possibly undergo additional approximations [60]. It has turned out in numerical investigations that the use of a surprisingly small number of CS basis functions leads to converged results, e.g., in spin-boson type problems tackled by the so-called multi Davydov D2 basis function [69–71], or in the multi-configuration variational Gaussian method [72–76], as well as the coupled coherent states approach developed by Shalashilin and Child [77–79, 29, 80].

It has been worked out in [81, 82], that Glauber CS are promising basis functions also for full fledged dynamical calculations for some many-body systems such as Bose-Hubbard (BH) dynamics beyond the semiclassical or the Gross-Pitaevskii level [83]. This success as well as that of the CS basis functions alluded to above, leads us to investigate the question if also GCS are favorable basis functions for Hamiltonian with $U(1)$ symmetry, in the light of the fact that the GCS itself has a fixed particle number.

In fact, the potential merits of GCS for the BH model have already been realized by other authors. The mathematical foundation of the phase space formulation of physical systems with Lie group symmetries has been considerably widened by the works of Brif and Mann [84, 85]. Based on their progress, the dynamical description of many-body systems in terms of phase space distributions has received new impetus from the works of Korsch and collaborators [86, 32]. In these works, the authors adopt the GCS as basis functions, and equations of motion for the P- as well as the Q-function of quantum optics [33, 87] have been derived and solved for the BH model with small system size. The use of GCS has been investigated and favored in the same context by Buonsante and Penna in their enlightening review [31], whose focus is on variational mean-field methods. A more recent review with a focus on SU(2) CS, introduced as atomic coherent states in [88], is given in

[89]. An extension of the formalism towards dissipative Lindblad type equations in terms of P functions has been given in [90].

Inspired by these existing works, we will combine the GCS with the variational principle to investigate the time-dependent dynamics of the BH model. It will be shown that this method can go beyond the mean-field theory and faithfully and efficiently approach the exact quantum result. More importantly, this method can be applied to study large system sizes and explore quantum many-body effects that had hitherto been unexplored.

4.2 Bose-Hubbard model

One paradigmatic model for many-body systems is the Bose-Hubbard model, which is used to describe cold atoms trapped in optical lattices within the lowest Bloch band approximation [91], and this approximation is good under the assumption that thermal fluctuations do not have enough energy to excite the particles. We note that a solution of the Schrödinger equation beyond the lowest band approximation has been considered in [92]. The BH model has been realized in ultracold atomic experiments [93, 8, 94]. Its 1D form can be expressed as

$$\hat{H} = -J \sum_{i=1} \left[\hat{a}_i^\dagger \hat{a}_{i+1} + \text{H.c.} \right] + \frac{U}{2} \sum_{i=1}^{M} \hat{a}_i^{\dagger 2} \hat{a}_i^2, \tag{4.2}$$

where $\hat{a}_i^\dagger$ and $\hat{a}_i$ are the bosonic creation and annihilation operator, respectively. The first term in Eq. (4.2) describes the tunnelling of particles between different sites, and J is the isotropic tunnelling strength. Depending on the boundary conditions, the 1D lattice sites can be either thought of as a chain where the site index i ranges from 1 to $M-1$ (open boundary condition), or a circle (periodic boundary condition) with

$$\hat{a}_M^\dagger \hat{a}_{M+1} \equiv \hat{a}_M^\dagger \hat{a}_1.$$

The second term in Eq. (4.2) is the two-body interaction term which accounts for the energy shift due to the occurrence of two particles at the same site.

In experimental setups, the optical lattice is created through the interference of multiple laser beams oriented in opposite directions across three-dimensional space. The two-body interaction strength, denoted as U, is modifiable directly through Feshbach resonances. This adjustment involves tuning the s-wave scattering length via adjusting the magnetic field near the resonance point, ranging from significantly positive to markedly negative values [95]. Notably, a positive scattering length is indicative of repulsive interactions, whereas a negative scattering length signals attractive interactions. The relative interaction strength U/J, is controlled by tuning the laser intensities. Upon loading ultra-cold bosonic atoms into these optical traps, their dynamical evolution is monitored using sophisticated detection methods, including absorption imaging, time-of-flight imaging, and other state-of-the-art techniques with single-site resolution [8, 96–99].

This model is extensively studied both in experiment and theory, since it can capture the essence of the superfluid-insulator phase transition [100, 34]. Besides, benefiting from the good controlability of ultracold atomic systems, the Bose-Hubbard model also provides a promising platform for quantum simulation of many-body systems [101–103].

Despite of the prominent progress in the study of Bose-Hubbard model, the time-dependent dynamics of this model is still a formidable problem. Firstly, the appearance of the non-quadratic interaction term makes the Hamiltonian hard to be diagonalized numerically, due to the fact that the dimension of the Hilbert space expands exponentially with increasing system size. On the other hand, the entanglement entropy of time-evolved states tends to be unbounded, so the DMRG-like methods, the standard tools in equilibrium dynamics for 1D gapped system with local interaction, also fail for long-time evolution [103]. Hopefully, our variational approach provides an alternative route to solve this problem. In the following, we will apply our variational basis function from Eq. (4.1) with GCS instead of the Glauber CS to the time-dependent dynamics of the 1D Bose-Hubbard model.

4.3 Linear combination of GCS

The main working horse of the present thesis is based on the fact that, for a bosonic lattice model with S particles and M sites, we can utilize the linear combination of GCS as a set of basis functions for the solution of the time-dependent Schrödinger equation (TDSE) [104]. The analog to basis function expansion (4.1) is given as [104]

$$|\Psi(t)\rangle = \sum_{j=1}^{N} A_j(t)|S,\vec{\xi}_j(t)\rangle, \tag{4.3}$$

where $|S,\vec{\xi}_j\rangle$ in short-hand vectorized notation denotes the j-th GCS in our basis function with the characteristic parameters

$$\vec{\xi}_j = \{\xi_{j1},\xi_{j2},\cdots,\xi_{jM}\},$$

and the expansion coefficients A_j are responsible for the connection between different GCS, which becomes clear in their coupled equations of motion to be detailed below. It is also worth noting that A_j is not the probability amplitude like in the case of a normal superposition, since the GCS form a non-orthogonal basis and the value of $|A_j|^2$ can be larger than one. Our basis function is close in spirit to the multi Davydov-basis function designed for spin-boson problems [69, 61], which also consists of multiple CSs, and these two Ansätze share some similar features. Firstly, both GCS and CS are non-orthogonal bases, so the overlap between different basis functions will take an important role in the equations of motion. However, the non-orthogonality can also cause a singularity of the equations of motion if two basis functions are very close during evolution. As has been noticed in the literature [105], this severe problem is a major obstacle for the application of CS-based methods and great care has to be taken in the implementation of the equations of motion [70]. Fortunately, most of the times, the singularity problem of GCS bases can be solved straightforwardly by a simple regularization as proved in [104], which will also be explained below. And the numerical stability of GCS bases allows us to explore the dynamics in generic many-body systems. Secondly, the set of GCS also forms an overcomplete basis, which means if we employ enough basis functions in Eq. (4.3), in principle our solution will be very close to the exact one. Moreover, when $N = 1$, both Glauber CS and GCS bases will give the mean-field results by means of the TDVP shown below, while increasing N allows us straightforwardly to go beyond mean-field and recover the quantum effects as much as we can.

Expansion in momentum space

Another way to understand how the basis function expansion in Eq. (4.3) works is given by going to the quasi-momentum space. In momentum representation, the Hamiltonian of the one dimensional system, represented by Eq. (4.2), is transformed into

$$\hat{H} = -2J\sum_k \cos(k)\hat{b}_k^\dagger \hat{b}_k + \frac{U}{2M}\sum_{k,k',p} \hat{b}_{k+p}^\dagger \hat{b}_{k'-p}^\dagger \hat{b}_k \hat{b}_{k'}, \tag{4.4}$$

where k is the quasi-momentum in the region $[-\frac{\pi}{a}\ \frac{\pi}{a})$ with a being the lattice constant, and $\hat{b}_k$ ($\hat{b}_k^\dagger$) is the corresponding annihilation (creation) operator defined in Eq. (2.13). The first term of the equation derives from the hopping term in the original Hamiltonian (Eq. (4.2)), while the second stems from the interaction term.

Simultaneously, an arbitrary GCS of the form $\frac{1}{\sqrt{S!}}\left(\sum_{i=1}^M \xi_i \hat{a}_i^\dagger\right)^S |\text{vac}\rangle$ can be rewritten as $\frac{1}{\sqrt{S!}}\left(\sum_k \tilde{\xi}_k \hat{b}_k^\dagger\right)^S |\text{vac}\rangle$, as we have seen in Chapter. 2. For example, the uniformly distributed state $\frac{1}{\sqrt{S!}}\left(\sum_{i=1}^M \frac{1}{\sqrt{M}}\hat{a}_i^\dagger\right)^S |\text{vac}\rangle$ corresponds to a zero-momentum condensate $\frac{1}{\sqrt{S!}}(\hat{b}_{k=0}^\dagger)^S|\text{vac}\rangle$. Based on the spirit of the Fourier transformation, a localized state in quasi-momentum picture will be delocalized in position space.

The dynamical effect of the first term of Eq. (4.4), is to imprint a relative phase defined by

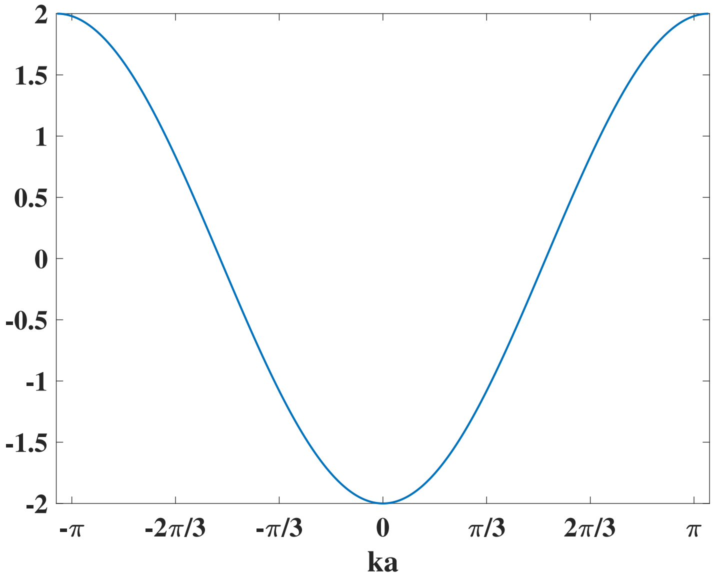

Fig. 4.1 Band function of hopping term in the first Brillouin zone.

the dispersion relation in the first Brillouin zone

$$\varepsilon_k = -2J\cos(ka) \tag{4.5}$$

as depicted in Fig. 4.1, onto each momentum distribution, which can be illustrated as follows:

$$\begin{aligned} &\exp\left(-\mathrm{i}\sum_k \varepsilon_k \hat{b}_k^\dagger \hat{b}_k t\right)\frac{1}{\sqrt{S!}}\left(\sum_k \tilde{\xi}_k \hat{b}_k^\dagger\right)^S |\mathrm{vac}\rangle \\ &= \frac{1}{\sqrt{S!}}\left(\sum_k \tilde{\xi}_k \mathrm{e}^{-\mathrm{i}\varepsilon_k t}\hat{b}_k^\dagger\right)^S |\mathrm{vac}\rangle. \end{aligned} \tag{4.6}$$

From this result we can infer that the condensate will persist under the hopping term alone. However, the second term will induce particle scattering in the quasi-momentum space. For instance, given the initial state is $\frac{1}{\sqrt{S!}}(\hat{b}_{k=0}^\dagger)^S|\mathrm{vac}\rangle$, particles will gradually depart from the condensate, scattering into other momentum states. This phenomenon has been observed in the experimental study of the phase transition from the superfluid phase to the insulator phase [43]. This process generates different configurations such as $|s_1\rangle_{k=-\frac{\pi}{a}}\cdots|s_l\rangle_{k=l}\cdots|s_M\rangle_{k=\frac{\pi}{a}}$, a product state in quasi-momentum space, denoting that s_l particles occupy the state with quasi-momentum $k = l$:

$$|\psi(t)\rangle = \sum_{\vec{S}} c_{\vec{S}} |s_1\rangle_{k=-\frac{\pi}{a}} \cdots |s_l\rangle_{k=l} \cdots |s_M\rangle_{k=\frac{\pi}{a}} \tag{4.7}$$

where $\vec{S}$ denotes any possible distribution of particles in the momentum space $\{s_1, s_2, \cdots, \}$, subject to the condition $s_1 + s_2 + \cdots + s_M = S$. Consequently, the macroscopic occupation is dismantled, and a single GCS can no longer accurately depict the time-evolved state. Yet, a linear combination of different GCS whose equations are governed by TDVP can provide a more flexible form to capture the essence of the evolved states.

Under conditions of relatively weak interaction strength or short evolution time with strong interaction, we expect that the time-dependent state will not deviate significantly from the condensate. In this case, a limited set of basis functions is required. For strong interaction strength which is challenging for the existing methods, a larger numerical effort will be expected.

4.4 Equations of motion for the GCS basis

To derive the variational equations of motion for all involved parameters, we employ the TDVP as mentioned above and to be discussed in detail in the following.

4.4.1 Variational principles

There exist two routines to implement the variational principle. We will review both of them in some detail.

The time-dependent variational principle

For a quantum system which is described by the Hamiltonian $\hat{H}$, the action and the Lagrangian are defined as follows:

$$S = \int \mathrm{dt\,L}; \qquad \mathrm{L} = \langle \Psi(\mathrm{t})| \left(\mathrm{i}\frac{\mathrm{d}}{\mathrm{dt}} - \hat{\mathrm{H}} \right) |\Psi(\mathrm{t})\rangle. \tag{4.8}$$

The Euler-Lagrange equations,

$$\frac{\partial L}{\partial x_k^*} - \frac{\mathrm{d}}{\mathrm{d}t}\frac{\partial L}{\partial \dot{x}_k^*} = 0, \tag{4.9}$$

where x_k is a notation for the wavefunction parameters, guarantee the stationarity of the action, thus leading to the Schrödinger equation. In this equation, the symbol $*$ denotes complex conjugation.

Considering a wavefunction parameterized in a general manner, $|\Psi(x_1, x_2, \cdots)\rangle$, where all parameters are complex numbers, the Lagrangian is represented as:

$$L = \mathrm{i}\langle\Psi|\dot{x}_i|V_i\rangle - \varepsilon \tag{4.10}$$

In this equation, the tangent state $|V_i\rangle$ is defined by $\frac{\partial}{\partial x_i}|\Psi\rangle$ and $\varepsilon = \langle\Psi|\hat{H}|\Psi\rangle$. The chain rule and the Einstein summation convention have been applied here.

Furthermore, the Euler-Lagrangian equation yields the following equations of motion:

$$\mathrm{i}\langle V_j|V_i\rangle\dot{x}_i = \frac{\partial\varepsilon}{\partial x_j^*} \tag{4.11}$$

In this context, we assume the wavefunction to be holomorphic across the entire complex plane, expressed as

$$\frac{\partial|\Psi\rangle}{\partial x_k^*} = 0 \tag{4.12}$$

for any given x_k. The Eq. (4.12) is also called Cauchy-Riemann equation in complex analysis. The holomorphic nature of the wavefunction is crucial, as it results in the equivalence of various variational principles, including the McLachlan's variational principle [26] (MCVP), time-dependent variational principle [27] (TDVP), and the Dirac-Frenkel variational principle [25] (DFVP). Comprehensive details and the condition for the equivalence of these variational principles are presented in Appendix. B. A side remark is that the alternative form of the Lagrangian

$$L = \frac{\mathrm{i}}{2}\left[\langle\dot{\Psi}|\Psi\rangle + \langle\Psi|\dot{\Psi}\rangle\right] - \varepsilon \tag{4.13}$$

would yield identical results [106].

Finally, we note that Eq. (4.11) is a series of implicit differential equations. To transform them into explicit form, it is necessary to compute the inverse of the mass matrix Ω, whose elements are given by

$$\Omega_{ij} = \langle V_i|V_j\rangle \tag{4.14}$$

However, the potential singularity of the mass matrix often hinders this process, thus some numerical strategies need to be developed to overcome this issue [70].

The geometrical perspective

Another approach to understand the variational principle is based on the geometrical perspective [106]. Considering the TDSE

$$\mathrm{i}\partial_t|\Psi\rangle = \hat{H}|\Psi\rangle \tag{4.15}$$

and applying the chain rule, the left side of the equation can be expressed as

$$\mathrm{i}\partial_t|\Psi\rangle = \dot{x}_j|V_j\rangle$$

in terms of the tangent states defined above, while the state in the right side $\hat{H}|\Psi\rangle$ is not the tangent state in general, as can be seen below. The best approximation for every time-step is to project both sides onto the tangent space which will give rise to the result in Eq. (4.11) From this perspective, insights about how the basis function works can be gained from the geometrical analysis as well. Given the definition of the GCS, the corresponding tangent state is

$$|V_i\rangle = \partial_{\xi_i}|S,\vec{\xi}\rangle = \sqrt{S}\hat{a}_i^\dagger|S-1,\vec{\xi}\rangle, \tag{4.16}$$

and one can immediately realize that the application of the hopping term on the GCS is to generate the tangent states

$$\sum_{\langle ij\rangle}\hat{a}_i^\dagger\hat{a}_j|S,\vec{\xi}\rangle = \sqrt{S}\sum_i \xi_j\hat{a}_i^\dagger|S-1,\vec{\xi}\rangle. \tag{4.17}$$

This implies that the hopping term alone will not project the state outside of the tangent space. In contrast, when interaction term acts on GCS, we obtain

$$\sum_{i=1}^{M}\hat{a}_i^{\dagger 2}\hat{a}_i^2|S,\vec{\xi}\rangle = S\sum_{i=1}^{M}\xi_i^2\hat{a}_i^{\dagger 2}|S-2,\vec{\xi}\rangle, \tag{4.18}$$

which doesn't belong to the tangent space. Hence, our objective is to utilize linear combinations to offset the deviation caused by the interaction term.

4.4.2 TDVP applied to the GCS basis function

Because the Lagrangian form of the TDVP is based on the principle of least action which provides a clear physical intuition, in this part, we will apply the TDVP to the basis function expansion as presented in Eq. (4.3), and give a step-by-step derivation of the equations of motion as shown in [104].

Equations of motion

All the time-dependent parameters in Eq. (4.3) are assumed to be complex and it is also clear that the basis functions fulfill the holomorphic condition. The Lagrangian of the basis function expansion of $|\Psi(t)\rangle$ consists of two parts:

$$L = \mathrm{i}\langle\Psi(t)|\partial_t|\Psi(t)\rangle - \langle\Psi(t)|\hat{H}|\Psi(t)\rangle. \tag{4.19}$$

By means of the chain rule, the time derivative of $|\Psi(t)\rangle$ is found to be given by

$$\begin{aligned}
\partial_t|\Psi(t)\rangle &= \partial_t\left(\sum_{j=1}^{N} A_j(t)|S,\vec{\xi}_j(t)\right) \\
&= \sum_{j=1}^{N}\dot{A}_j(t)|S,\vec{\xi}_j(t)\rangle + \sum_{j=1}^{N} A_j(t)\partial_t|S,\vec{\xi}_j(t)\rangle \\
&= \sum_{j=1}^{N}\dot{A}_j(t)|S,\vec{\xi}_j(t)\rangle + \sum_{j=1}^{N} A_j(t)\sum_{i=1}^{M}\dot{\xi}_{ji}(t)\partial_{\xi_{ji}}|S,\vec{\xi}_j(t)\rangle \\
&= \sum_{j=1}^{N}\dot{A}_j(t)|S,\vec{\xi}_j(t)\rangle + \sqrt{S}\sum_{j=1}^{N} A_j(t)\sum_{i=1}^{M}\dot{\xi}_{ji}(t)\hat{a}_i^{\dagger}|S-1,\vec{\xi}_j(t)\rangle,
\end{aligned} \tag{4.20}$$

so the first term in Eq. (4.19) is

$$\begin{aligned}
\mathrm{i}\langle\Psi(t)|\partial_t|\Psi(t)\rangle &= \mathrm{i}\sum_{k=1}^{N} A_k^*\langle S,\vec{\xi}_k|\left[\sum_{j=1}^{N}\dot{A}_j|S,\vec{\xi}_j\rangle + \sqrt{S}\sum_{j=1}^{N} A_j\sum_{i=1}^{M}\dot{\xi}_{ji}\hat{a}_i^{\dagger}|S-1,\vec{\xi}_j\rangle\right] \\
&= \mathrm{i}\sum_{k,j=1}^{N} A_k^*\dot{A}_j\langle\vec{\xi}_k|\vec{\xi}_j\rangle + \mathrm{i}S\sum_{j,k=1}^{N} A_k^* A_j\sum_{i=1}^{M}\xi_{ki}^*\dot{\xi}_{ji}\langle\vec{\xi}_k^{\prime}|\vec{\xi}_j^{\prime}\rangle,
\end{aligned} \tag{4.21}$$

where we have used the more compact notation $\langle\vec{\xi}_k|\vec{\xi}_j\rangle$ and $\langle\vec{\xi}_k^{\prime}|\vec{\xi}_j^{\prime}\rangle$ to represent the overlap $\langle S,\vec{\xi}_k|S,\vec{\xi}_j\rangle$ and $\langle S-1,\vec{\xi}_k|S-1,\vec{\xi}_j\rangle$, respectively.

The second term in Eq. (4.19) relies on the specific system described by $\hat{H}$. Below we will take the 1D BH model given by Eq. (4.2) as an example which yields

$$\begin{aligned}\langle\Psi|\hat{H}|\Psi\rangle &= \sum_{k,j=1}^{N} A_k^* A_j \langle S, \vec{\xi}_k|\hat{H}|S, \vec{\xi}_j\rangle \\ &= \sum_{k,j=1}^{N} A_k^* A_j \left[-JS \sum_{i=1} (\xi_{ki}^* \xi_{j,i+1} + \xi_{k,i+1}^* \xi_{ji}) \langle \vec{\xi}_k' | \vec{\xi}_j' \rangle + \frac{U}{2} S(S-1) \sum_{i=1}^{M} \xi_{ki}^{*2} \xi_{ji}^2 \langle \vec{\xi}_k'' | \vec{\xi}_j'' \rangle \right],\end{aligned} \tag{4.22}$$

where $\langle \vec{\xi}_k'' | \vec{\xi}_j'' \rangle = \langle S-2, \vec{\xi}_k | S-2, \vec{\xi}_j \rangle$. Combing Eq. (4.21) and Eq. (4.22), we obtain the total Lagrangian

$$\begin{aligned} L = {} & \mathrm{i} \sum_{k,j=1}^{N} A_k^* \dot{A}_j \langle \vec{\xi}_k | \vec{\xi}_j \rangle + \mathrm{i}S \sum_{j,k=1}^{N} A_k^* A_j \sum_{i=1}^{M} \xi_{ki}^* \dot{\xi}_{ji} \langle \vec{\xi}_k' | \vec{\xi}_j' \rangle \\ & - \sum_{k,j=1}^{N} A_k^* A_j \left[-JS \sum_{i=1} (\xi_{ki}^* \xi_{j,i+1} + \xi_{k,i+1}^* \xi_{ji}) \langle \vec{\xi}_k' | \vec{\xi}_j' \rangle + \frac{U}{2} S(S-1) \sum_{i=1}^{M} \xi_{ki}^{*2} \xi_{ji}^2 \langle \vec{\xi}_k'' | \vec{\xi}_j'' \rangle \right]. \end{aligned} \tag{4.23}$$

Two different sets of parameters $\{A_j\}$ and $\{\xi_{ji}\}$ are included in the Lagrangian, and we derive their equations of motion separately. For the complex conjugate of the expansion coefficients A_k^*, we calculate the corresponding first derivative of the Lagrangian

$$\frac{\partial L}{\partial A_k^*} = \mathrm{i} \sum_{j=1}^{N} \dot{A}_j \langle \vec{\xi}_k | \vec{\xi}_j \rangle + \mathrm{i}S \sum_{j=1}^{N} A_j \sum_{i=1}^{M} \xi_{ki}^* \dot{\xi}_{ji} \langle \vec{\xi}_k' | \vec{\xi}_j' \rangle - \frac{\partial H}{\partial A_k^*}, \tag{4.24}$$

where

$$\frac{\partial H}{\partial A_k^*} = \sum_{j=1}^{N} A_j \left[-JS \sum_{i=1}^{M-1} (\xi_{ki}^* \xi_{j,i+1} + \xi_{k,i+1}^* \xi_{ji}) \langle \vec{\xi}_k' | \vec{\xi}_j' \rangle + \frac{U}{2} S(S-1) \sum_{i=1}^{M} \xi_{ki}^{*2} \xi_{ji}^2 \langle \vec{\xi}_k'' | \vec{\xi}_j'' \rangle \right]. \tag{4.25}$$

Because $\dot{A}_k^*$ doesn't show up in the Lagrangian, the second part on the LHS of Eq. (4.9) vanishes. Note that although we take the derivative of A_k^* and $\dot{A}_k^*$, the outcome on the right hand side of Eq. (4.24) is related to the time derivative of A_j and j may not be equal to k, this is because the different basis functions are already coupled in the Lagrangian given in Eq. (4.19). From the Euler-Lagrange Eq. (4.9), the equations of motion for the coefficients A_j

read

$$\mathrm{i}\sum_{j=1}^{N}\dot{A}_j\langle\vec{\xi}_k|\vec{\xi}_j\rangle+\mathrm{i}S\sum_{j=1}^{N}A_j\sum_{i=1}^{M}\xi^*_{ki}\dot{\xi}_{ji}\langle\vec{\xi}'_k|\vec{\xi}'_j\rangle-\frac{\partial H}{\partial A^*_k}=0. \tag{4.26}$$

Next, we switch to the equations for the characteristic parameters $\{\xi_{ji}\}$. To this end, we replace x^*_k with ξ^*_{km} in Eq. (4.9) and get the corresponding derivative after some tedious derivation to be given by

$$\begin{aligned}\frac{\partial L}{\partial\xi^*_{km}}=\mathrm{i}S\Big[&\sum_{j=1}^{N}A^*_k\dot{A}_j\xi_{jm}\langle\vec{\xi}'_k|\vec{\xi}'_j\rangle+\sum_{j=1}^{N}A^*_kA_j\dot{\xi}_{jm}\langle\vec{\xi}'_k|\vec{\xi}'_j\rangle\\&+(S-1)\sum_{j=1}^{N}A^*_kA_j\sum_{i=1}^{M}(\xi^*_{ki}\dot{\xi}_{ji})\xi_{jm}\langle\vec{\xi}''_k|\vec{\xi}''_j\rangle\Big]-\frac{\partial H}{\partial\xi^*_{km}},\end{aligned} \tag{4.27}$$

where $\langle\vec{\xi}'''_k|\vec{\xi}'''_j\rangle=\langle S-3,\vec{\xi}_k|S-3,\vec{\xi}_j\rangle$ and

$$\begin{aligned}\frac{\partial H}{\partial\xi^*_{km}}=\sum_{j=1}^{N}A^*_kA_j\Big[&-JS(\xi_{j,m+1}+\xi_{j,m-1})\langle\vec{\xi}'_k|\vec{\xi}'_j\rangle-JS(S-1)\sum_{i=1}^{M-1}(\xi^*_{ki}\xi_{j,i+1}+\xi^*_{k,i+1}\xi_{j,i})\xi_{jm}\\&\times\langle\vec{\xi}''_k|\vec{\xi}''_j\rangle+US(S-1)\xi^*_{km}\xi^2_{jm}\langle\vec{\xi}''_k|\vec{\xi}''_j\rangle+\frac{U}{2}S(S-1)(S-2)\sum_{i=1}^{M}\xi^{*2}_{ki}\xi^2_{ji}\xi_{jm}\langle\vec{\xi}'''_k|\vec{\xi}'''_j\rangle\Big].\end{aligned} \tag{4.28}$$

Again, the second component of the Euler-Lagrange equation Eq. (4.9) is zero. So we obtain the equation of motion for ξ_{km} parameters to be given by

$$\begin{aligned}&\mathrm{i}S\Big[\sum_{j=1}^{N}A^*_k\dot{A}_j\xi_{jm}\langle\vec{\xi}'_k|\vec{\xi}'_j\rangle+\sum_{j=1}^{N}A^*_kA_j\dot{\xi}_{jm}\langle\vec{\xi}'_k|\vec{\xi}'_j\rangle+(S-1)\sum_{j=1}^{N}A^*_kA_j\sum_{i=1}^{M}(\xi^*_{ki}\dot{\xi}_{ji})\xi_{jm}\langle\vec{\xi}''_k|\vec{\xi}''_j\rangle\Big]\\&-\frac{\partial H}{\partial\xi^*_{km}}=0.\end{aligned} \tag{4.29}$$

From Eq. (4.26) and Eq. (4.29), we can observe that all the parameters are coupled with each other in a non-linear way, and the inner products such as $\langle\vec{\xi}'_k|\vec{\xi}'_j\rangle$, which will not appear for orthogonal basis-set methods, play an important role in this coupling. If we consider the large particle number limit $S\to\infty$ with finite number of sites M which corresponds to the classical limit, the $\langle\vec{\xi}_k|\vec{\xi}_j\rangle$ is going to vanish for arbitrary $k\neq j$, namely,

$$\langle\vec{\xi}_k|\vec{\xi}_j\rangle=\delta_{kj}. \tag{4.30}$$

This is because in the expression

$$\langle \vec{\xi}_k | \vec{\xi}_j \rangle = \Big(\sum_{i=1}^{M} \xi_{ki}^* \xi_{ji} \Big)^S$$

as shown in Table. 2.1, the absolute value of the summation in the bracket is equal or smaller than 1. As a result, Eq. (4.30) leads to the decoupling among the different GCS bases $|\vec{\xi}_j\rangle$ and $|\vec{\xi}_j\rangle$ for $k \neq j$. Particularly, if the initial state is a single GCS, only this GCS will join in the evolution which is governed by the simplified equations (the multiplicity indices k, j are not needed here and the index i is the site index)

$$\mathrm{i}\dot{\xi}_i = -J(\xi_{i+1} + \xi_{i-1}) + U(S-1)|\xi_i|^2 \xi_i, \tag{4.31}$$

and additional basis functions will not be occupied.
If we replace ξ_i with $\psi_i = \sqrt{S}\xi_i$ where $|\psi_i|^2$ stands for the particle density on the i-th site and neglect the difference between $S-1$ and S, we will get the so-called non-linear Schrödinger equations or the discrete Gross-Pitaevskii equation [107, 108]

$$\mathrm{i}\dot{\psi}_i = -J(\psi_{i+1} + \psi_{i-1}) + U|\psi_i|^2 \psi_i. \tag{4.32}$$

Eq. (4.31) and Eq. (4.32) are mean-field equations of the BH model which are widely applied to describe the dynamics of the condensate [109].

Matrix form of the full variational equations of motion

The time evolution of all parameters can be gained by integrating Eqs. (4.26) and (4.29). Both of them are implicit equations, however. In order to facilitate their numerical implementation, we rewrite these equations in matrix form as follows:

$$\begin{pmatrix} \boldsymbol{X} & \boldsymbol{Y} \\ \\ \boldsymbol{Y}^\dagger & \boldsymbol{Z} \end{pmatrix} \begin{pmatrix} \dot{\boldsymbol{A}} \\ \\ \dot{\boldsymbol{\xi}} \end{pmatrix} = -\mathrm{i} \begin{pmatrix} \boldsymbol{R}_1 \\ \\ \boldsymbol{R}_2 \end{pmatrix}, \tag{4.33}$$

where the mass matrix (matrix of block matrices on the LHS) is Hermitian. The corresponding block matrices are given by

$$\boldsymbol{X}_{kj} = \langle \vec{\xi}_k | \vec{\xi}_j \rangle, \tag{4.34}$$

$$\boldsymbol{Y} = S(\boldsymbol{\xi}_1^*, \boldsymbol{\xi}_2^*, \cdots, \boldsymbol{\xi}_M^*) \otimes \boldsymbol{A}^T \circ (\mathbf{1}_{1\times M} \otimes \boldsymbol{X}^{'}), \tag{4.35}$$

$$\boldsymbol{Z} = \mathbf{1}_{M\times M} \otimes \boldsymbol{\rho} \circ \boldsymbol{F}, \tag{4.36}$$

where the vector $\vec{\xi}_k = \{\xi_{k1}, \xi_{k2}, \cdots, \xi_{kM}\}$ is now indexed by the basis function discretization index and the vector $\boldsymbol{\xi}_m$, to be defined below, is indexed by the mode index. Furthermore,

$$\boldsymbol{F}_{ij} = S(S-1)\boldsymbol{X}^{''} \circ (\boldsymbol{\xi}_j^* \cdot \boldsymbol{\xi}_i^T)(i \neq j), \tag{4.37}$$

$$\boldsymbol{F}_{ii} = S\boldsymbol{X}^{'} + S(S-1)\boldsymbol{X}^{''} \circ (\boldsymbol{\xi}_i^* \cdot \boldsymbol{\xi}_i^T), \tag{4.38}$$

where $\mathbf{1}_{m\times n}$ is an $m \times n$ matrix which only consists of ones, and $\boldsymbol{X}^{'}_{kj} = \langle \vec{\xi}^{\,\prime}_k | \vec{\xi}^{\,\prime}_j \rangle$ and $\boldsymbol{X}^{''}_{kj} = \langle \vec{\xi}^{\,\prime\prime}_k | \vec{\xi}^{\,\prime\prime}_j \rangle$ are overlaps of $(S-1)$ and $(S-2)$-boson GCS, respectively, whereas $\boldsymbol{\rho}_{kj} = A_k^* A_j$. Additionally, $\otimes$ denotes the tensor-product, and $\cdot$ denotes the standard scalar product.

We note that the mass matrix tends to be singular during propagation which is frequently encountered in the case of Glauber CS [70]. A numerical strategy called regularization is used to address this issue by introducing a small perturbation on the mass matrix. To this end, we add a small number ε around 10^{-5} to the diagonal elements of the matrix $\boldsymbol{\rho}$ such that $\tilde{\boldsymbol{\rho}} = \boldsymbol{\rho} + \varepsilon \mathrm{I}$ where I denotes identity matrix. This perturbation can also be added on other components of the mass matrix as discussed in details in [110]. Our numerical results show that the adjustment on $\boldsymbol{\rho}$ ensures stable propagation while minimally impacting the quality of our results.

Moreover, the vectors on the LHS and RHS are defined as

$$\dot{\boldsymbol{A}} = \begin{pmatrix} \dot{A}_1 \\ \dot{A}_2 \\ \vdots \\ \dot{A}_N \end{pmatrix}, \dot{\boldsymbol{\xi}} = \begin{pmatrix} \dot{\boldsymbol{\xi}}_1 \\ \dot{\boldsymbol{\xi}}_2 \\ \vdots \\ \dot{\boldsymbol{\xi}}_M \end{pmatrix}, \boldsymbol{\xi}_m = \begin{pmatrix} \xi_{1m} \\ \xi_{2m} \\ \vdots \\ \xi_{Nm} \end{pmatrix}, \boldsymbol{R}_1 = \begin{pmatrix} \frac{\partial H}{\partial A_1^*} \\ \frac{\partial H}{\partial A_2^*} \\ \vdots \\ \frac{\partial H}{\partial A_N^*} \end{pmatrix}, \boldsymbol{R}_2 = \begin{pmatrix} \frac{\partial H}{\partial \boldsymbol{\xi}_1^*} \\ \frac{\partial H}{\partial \boldsymbol{\xi}_2^*} \\ \vdots \\ \frac{\partial H}{\partial \boldsymbol{\xi}_M^*} \end{pmatrix}. \tag{4.39}$$

with $H = \langle\Psi|\hat{H}|\Psi\rangle$ denoting the expectation value of the Hamiltonian given in Eq. (4.22). The $\boldsymbol{R_1}$ derived from Eq. (4.25) is

$$\frac{\partial H}{\partial \boldsymbol{A}^*} = -JS\boldsymbol{X}' \circ \sum_{i=1} \left(\boldsymbol{\xi}_i^* \cdot \boldsymbol{\xi}_{i+1}^T + \boldsymbol{\xi}_{i+1}^* \cdot \boldsymbol{\xi}_i^T\right) \cdot \boldsymbol{A} + \frac{U}{2}S(S-1)\boldsymbol{X}'' \circ \left[\sum_{i=1} (\boldsymbol{\xi}_i^*)^2 \cdot (\boldsymbol{\xi}_i^2)^T\right] \cdot \boldsymbol{A} \tag{4.40}$$

which is an $N \times 1$ vector. The elements of $\boldsymbol{R_2}$ derived from Eq. (4.28) are

$$\begin{aligned}\frac{\partial H}{\partial \boldsymbol{\xi}_m^*} = {} & -JS\boldsymbol{\rho} \circ \boldsymbol{X}' \cdot (\boldsymbol{\xi}_{m+1} + \boldsymbol{\xi}_{m-1}) - JS(S-1)\boldsymbol{\rho} \circ \boldsymbol{X}'' \circ \sum_{i=1} \left(\boldsymbol{\xi}_i^* \cdot \boldsymbol{\xi}_{i+1}^T + \boldsymbol{\xi}_{i+1}^* \cdot \boldsymbol{\xi}_i^T\right) \cdot \boldsymbol{\xi}_m \\ & + US(S-1)\boldsymbol{\rho} \circ \boldsymbol{X}'' \cdot \boldsymbol{\xi}_m^2 \circ \boldsymbol{\xi}_m^* + \frac{U}{2}S(S-1)(S-2)\boldsymbol{\rho} \circ \boldsymbol{X}''' \circ \left[\sum_{i=1} (\boldsymbol{\xi}_i^*)^2 \cdot (\boldsymbol{\xi}_i^2)^T\right] \cdot \boldsymbol{\xi}_m,\end{aligned} \tag{4.41}$$

where M elements are included and every element is an $N \times 1$ vector. So totally $(N+1)M$ differential equations are contained in Eq. (4.33).

Expectation values

With the form of basis function expansion Eq. (4.3), it is straightforward to calculate the expectation values of operators. Given an operator $\hat{O}$, we have

$$\langle\hat{O}\rangle = \sum_{k,j}^{N} A_k^* A_j \langle S, \vec{\xi}_k(t)|\hat{O}|S, \vec{\xi}_j(t)\rangle = \text{sum}(\boldsymbol{\rho} \circ \boldsymbol{O}, \text{all}) \tag{4.42}$$

where $\boldsymbol{\rho}_{kj} = A_k^* A_j$ defined as same as above, and the matrix $\boldsymbol{O}$ has the same dimension but with the entries

$$\boldsymbol{O}_{kj} = \langle S, \vec{\xi}_k(t)|\hat{O}|S, \vec{\xi}_j(t)\rangle. \tag{4.43}$$

The symbol $\circ$ denotes the Hadamard-product (element-wise multiplication of matrices) and "sum(...,all)" denotes the summation over all the entries.

To make progress, operator ordering is a key concept. In our framework, we consistently apply normal ordering to our operators, ensuring that all creation operators are positioned to the left of the annihilation operators. This systematic arrangement is achieved through the application of the commutation relationship in Eq. (2.2). If $\hat{O}$ is a normal-ordered operator such as $\hat{a}_f^\dagger \hat{a}_g^\dagger \hat{a}_h^\dagger \cdots \hat{a}_l \hat{a}_m \hat{a}_n \cdots$, the matrix entries are computed as

$$\boldsymbol{O}_{kj} = S(S-1)\cdots(S-n)\xi_{kf}^* \xi_{kg} \xi_{kh}^* \cdots \xi_{jl} \xi_{jm} \xi_{jn} \cdots \langle S-n, \vec{\xi}_k | S-n, \vec{\xi}_j \rangle, \tag{4.44}$$

where n is the number of creation (annihilation) operators, and we have used the property $\hat{a}_i|S,\vec{\xi}_j\rangle = \sqrt{S}\xi_{ji}|S-1,\vec{\xi}_j\rangle$ of the GCS from Table. 2.1 in the second chapter. For small values of N, the numerical evaluation of Eq. (4.42) can be performed without too much computational effort.

4.5 A first numerical appetizer: the bosonic Josephson junction

To verify the validity of our variational approach introduced in last section, we will apply it to a simple system called bosonic Josephson junction (BJJ).

Restricting the amount of lattice sites makes the quantum dynamics of the BH model in Eq. (4.2) easily tractable numerically for moderate particle numbers. Recent theoretical work has thus focused on the cases of four (and six) sites [111] with different levels of approximation: exact, semiclassical and classical (mean-field, or truncated Wigner approximation (TWA)). Also the trimer (ring) case has been studied, due to the facts that it is leading to the melting of discrete vortices via quantum fluctuations [112] and that it is the smallest system that displays chaotic mean-field dynamics without an external driving term [113]. This system has also been dealt with using a group theoretical [114, 115] and a semiclassical time-domain approach [116]. With an additional drive (periodic kicks) even the double well case is showing signatures of chaos [117].

Furthermore, the case of two wells without external driving has been extensively studied. The system dynamics has, e. g., been investigated both in a mean-field classical approximation and fully quantum mechanically [118–121], as well as also semiclassically, using a phase space picture [122] or employing the Herman-Kluk propagator [123, 116, 124]. This same propagator has also been used in a semiclassical time-domain study of the single well problem [125]. Furthermore, the driven single well problem has served as a model in a study of dynamical tunneling [126].

An important lesson from the vast literature is that semiclassical approaches do well in reproducing the full quantum results, while the mean-field and/or TWA approach have their limitations. TWA does, e.g., not allow for the investigation of revival phenomena, present in the quantum dynamics. One interesting phenomenon, that could already be uncovered using a mean-field approach, is the macroscopic quantum self trapping effect in BJJ, where the population imbalance (to be defined below) has a nonzero average [118]. It turns out that mean-field theory predicts the transition to macroscopic quantum self trapping at too large values of the on-site interaction strength, however [127].

In the following, we will focus on the case of two wells, for which the direct experimental observation of tunneling and self trapping has become possible [128]. Theoretically, this case has been reviewed in [129] and a fresh look on finite size (i.e., finite particle number) effects in a mean-field description [127]. These authors have used a single so-called atomic or SU(2) GCS [88], reviewed in Chapter. 2, to uncover mean-field $1/S$ corrections to the more familiar mean-field results based on Glauber CS. We will also employ those favorable number conserving SU(2) GCS here. We will not use them in a mean-field spirit, however, where just a single state is taken to solve the TDSE. In contrast, we will investigate what happens if we allow for non-trivial multiplicity, which means we will use a superposition of SU(2) GCS, given in Eq. (4.3), to solve the TDSE.

4.5.1 Classical description of the bosonic Josephson junction

In this section, we will review the equations underlying the mean-field description of bosonic Josephson junctions by following [127, 129]. The major focus is on the fixed points of the equations along with their stability analysis.

The BJJ can be described by a double-well potential with a finite barrier in the middle, so the particles in each well can tunnel through the barrier and generate a current. The population imbalance induced by the current will cause the relative phase difference which in turn drives the current further. Many quantum phenomena inherent to the Josephson junction result from the dynamic interplay between this particle imbalance and the relative phase - a pair of conjugated variables [130–132].

An effective description of the BJJ is given by the two-site BH model [133]

$$\hat{H} = -J\left(\hat{a}_1^\dagger \hat{a}_2 + \hat{a}_2^\dagger \hat{a}_1\right) + \frac{U}{2}\left(\hat{a}_1^{\dagger 2}\hat{a}_1^2 + \hat{a}_2^{\dagger 2}\hat{a}_2^2\right), \tag{4.45}$$

where the first term describes the tunnelling of particles between the two sites and the second term is the on-site interaction. We recall that a positive U describes repulsive interaction between bosons because particles occurring on same site will increase the energy, and a negative U corresponds to attractive interaction.

To comprehend the physics behind this model well, we firstly focus on the mean-field theoretical description, where the wavefunction is given by an ideal condensate with fixed number of particles, namely, a single SU(2) GCS [88] of the form

$$
\begin{aligned}
|\Psi(t)\rangle &= \frac{1}{\sqrt{S!}}\left(\sqrt{\frac{1+z(t)}{2}}\hat{a}_1^\dagger + \sqrt{\frac{1-z(t)}{2}}\mathrm{e}^{-\mathrm{i}\phi(t)}\hat{a}_2^\dagger\right)^S |0,0\rangle \\
&= |S, \sqrt{\frac{1+z(t)}{2}}, \sqrt{\frac{1-z(t)}{2}}\mathrm{e}^{-\mathrm{i}\phi(t)}\rangle,
\end{aligned} \tag{4.46}
$$

where $z(t)$ denotes the particle number imbalance and $\phi(t) = \phi_1 - \phi_2$ is the relative phase. This wavefunction is a macroscopically occupied state with a coherent phase between the two sites. We note that, using two complex parameters ξ_1 and ξ_2 to represent SU(2) GCS is redundant, because the global phase is not relevant, and the sum of the norm of ξ_1 and ξ_2 is fixed to be 1. The relationship between $\{\xi_1, \xi_2\}$ and $\{z, \phi\}$ is explicitly presented as

$$
z = |\xi_1|^2 - |\xi_2|^2,\ \phi = \arg(\xi_1) - \arg(\xi_2). \tag{4.47}
$$

The equations of motion for $z(t)$ and $\phi(t)$ again follow from the TDVP. To begin with, we derive the Lagrangian of Eq. (4.46), which is given by:

$$
\begin{aligned}
L &:= \mathrm{i}\langle\Psi|\partial_t|\Psi\rangle - \langle\Psi|\hat{H}|\Psi\rangle \\
&= S\frac{1-z}{2}\dot{\phi} + JS\sqrt{1-z^2}\cos\phi - \frac{U}{4}S(S-1)z^2,
\end{aligned} \tag{4.48}
$$

where the factor $S(S-1)$ in the last term is caused by the consecutive action of two annihilation operators on SU(2) coherent state, and this factor would be replaced by S^2 if we utilize the normal (Glauber) coherent states as the basis. It is worth noting that adding a total time derivative of an analytical function to the Lagrangian won't alter the final equations of motion [134]. With this in mind, Eq. (4.48) can be further simplified to:

$$
\tilde{L} = -\frac{S}{2}z\dot{\phi} + JS\sqrt{1-z^2}\cos\phi - \frac{U}{4}S(S-1)z^2. \tag{4.49}
$$

The Euler-Lagrange equations Eq. (4.9) give rise to the following Josephson equations:

$$
\dot{z} = 2J\sqrt{1-z^2}\sin\phi := f_1, \tag{4.50}
$$

$$
\dot{\phi} = -2J\frac{z}{\sqrt{1-z^2}}\cos\phi - U(S-1)z := f_2. \tag{4.51}
$$

The two coupled equations derived from the mean-field theory unveil some notable Josephson effects. From Eq. (4.50), we observe that even if the initial value of z is zero but ϕ possesses a nonzero value, the time derivative of z persists. This suggests the generation of a current between the two sites, initiated by the relative phase, not the bias voltage or particle imbalance.

Moreover, the second term on the RHS of Eq. (4.51) implies that a nonzero imbalance reciprocally influences the phase difference. Another nonlinear effect becomes apparent when $z(0)$ approaches one and U/J is significantly large. In this scenario, ϕ alters swiftly, and z experiences rapid yet small amplitude fluctuations. This effect, known as the self-trapping effect, is characterized by $z(t)$ remaining nearly constant throughout the evolution.

For our discussion, we will limit our focus to the dynamics near the fixed points of Eq. (4.50) and Eq. (4.51). A class of stationary solutions of the above coupled nonlinear equations is given by the fixed points $(0, 2\pi n)$ with $n = 0, \pm 1, \pm 2, \dots$. It is straightforward to verify that these solutions represent the ground state of the classical Hamiltonian

$$\langle \hat{H} \rangle = \frac{US}{4}(S-1)z^2 - JS\sqrt{1-z^2}\cos\phi, \tag{4.52}$$

when $U > 0$. The stability of the fixed points can be evaluated via a linearization process involving the Jacobi matrix.

Specifically, the Jacobi matrix [135] at the point $(z^*, \phi^*) = (0,0)$ is given by

$$\mathbf{J} = \begin{pmatrix} \left.\frac{\partial f_1}{\partial z}\right|_{z^*,\phi^*} & \left.\frac{\partial f_1}{\partial \phi}\right|_{z^*,\phi^*} \\ \left.\frac{\partial f_2}{\partial z}\right|_{z^*,\phi^*} & \left.\frac{\partial f_2}{\partial \phi}\right|_{z^*,\phi^*} \end{pmatrix} = \begin{pmatrix} 0 & 2J \\ -2J-(S-1)U & 0 \end{pmatrix} \tag{4.53}$$

and its eigenvalues are

$$\lambda_{\pm} = \pm\sqrt{2}J\sqrt{-2+\frac{U}{J}-\frac{US}{J}} = \pm 2J\sqrt{-1-\Lambda}. \tag{4.54}$$

Here the so-called strength parameter Λ is defined as

$$\Lambda = U(S-1)/(2J), \tag{4.55}$$

which is an appropriate parameter combination to be used frequently in the following. Moreover, if $z(0)$ and $\phi(0)$ only exhibit minor deviations from the equilibrium point, we can derive the linearized equations from the Jacobi matrix.

$$\dot{z} = 2J\phi, \tag{4.56}$$

$$\dot{\phi} = -\left[2J + U(S-1)\right]z. \tag{4.57}$$

Considering the initial conditions $z(0) = z_0, \phi(0) = 0$, their general solutions are given by

$$z(t) = \frac{z_0}{2}\left[\mathrm{e}^{2J\sqrt{-(1+\Lambda)}t} + \mathrm{e}^{-2J\sqrt{-(1+\Lambda)}t}\right], \tag{4.58}$$

$$\phi(t) = \frac{z_0}{2}\sqrt{-(1+\Lambda)}\left[\mathrm{e}^{2J\sqrt{-(1+\Lambda)}t} - \mathrm{e}^{-2J\sqrt{-(1+\Lambda)}t}\right]. \tag{4.59}$$

The parameter Λ plays an important role in the stability of the dynamics around the fixed point. If $\Lambda > -1$, it is evident that both eigenvalues $\lambda_\pm$ are imaginary which implies that the point $(0,0)$ is a stable fixed point.

From Eq. (4.58) and Eq. (4.59) we have the oscillatory solutions

$$z(t) = z_0 \cos(\Omega t), \tag{4.60}$$

$$\phi(t) = -z_0\sqrt{1+\Lambda}\sin(\Omega t), \tag{4.61}$$

with the plasma frequency

$$\Omega = 2J\sqrt{1+\Lambda}. \tag{4.62}$$

On the other hand, if $\Lambda < -1$, the eigenvalues become real and $\lambda_\pm$ $(0,0)$ is no longer a stable fixed point, and the specific solutions from Eq. (4.58) and Eq. (4.59) are

$$z(t) = z_0 \cosh\left[2J\sqrt{-(1+\Lambda)}t\right], \tag{4.63}$$

$$\phi(t) = z_0\sqrt{-(1+\Lambda)}\sinh\left[2J\sqrt{-(1+\Lambda)}t\right] \tag{4.64}$$

which are hyperbolic functions. We stress that these above equations are only valid when the linearization condition $|z|, |\phi| \ll 1$ is fulfilled. Away from that regime the hyperbolic solution is unphysical.

Interestingly, the condition $\Lambda < -1$ introduces another set of stable fixed points given by

$$\left(\pm\sqrt{1-\frac{1}{\Lambda^2}}, 2\pi n\right),$$

which correspond to the symmetry-breaking ground state in the mean-field level, as the population in two wells is not same. To confirm the stability of these points, we compute the

Jacobi matrix at $\left(\pm\sqrt{1-\frac{1}{\Lambda^2}}, 2\pi n\right)$

$$\mathbf{J} = \left(\begin{array}{cc} 0 & \frac{2J}{\sqrt{\Lambda^2}} \\ -2J\Lambda(1+\Lambda\sqrt{\Lambda^2}) & 0 \end{array} \right). \tag{4.65}$$

Its eigenvalues are given by

$$\lambda_{\pm} = \pm\frac{2J\sqrt{-\Lambda^4-\Lambda\sqrt{\Lambda^2}}}{\sqrt{\Lambda^2}}. \tag{4.66}$$

When $\Lambda < -1$, the above values are imaginary, indicating that $\left(\pm\sqrt{1-\frac{1}{\Lambda^2}}, 2\pi n\right)$ are stable fixed points.

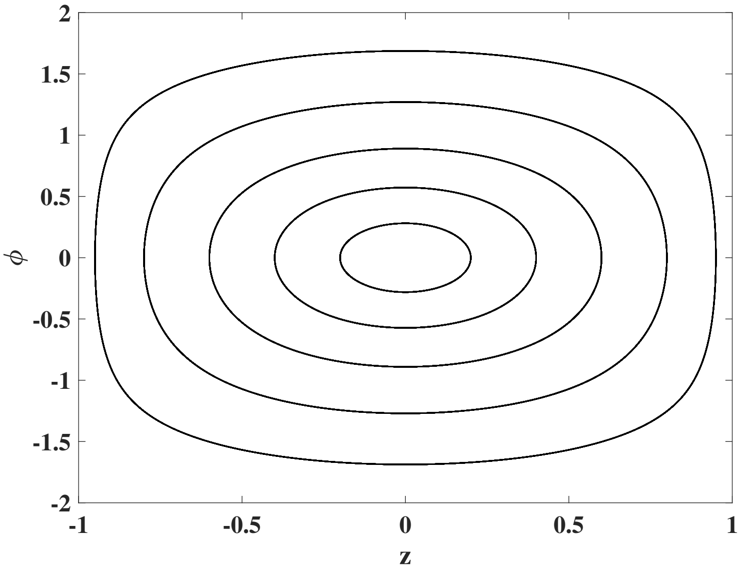

Fig. 4.2 Phase space trajectories from the mean-field dynamics for different initial values of z with fixed $\phi = 0$. The total number of particles is $S = 20$ and the interaction strength is $U = 0.1J$.

In Fig. 4.2, we set U to $0.1J$, and the particle number S is 20, which satisfies the stability condition $\Lambda > 1$. Several trajectories in the phase space composed of z and ϕ around the stable fixed point $(0,0)$ are plotted. All these trajectories follow elliptical orbits, signifying that both the imbalance and relative phase undergo periodic oscillation, and this pattern persists even if the initial point deviates significantly from $(0,0)$.

However, the situation will be dramatically changed if we turn to the regime with $\Lambda < -1$.

As shown in Fig. 4.3 for the attractive interaction strength $U = -0.15J$ and $S = 20$, the stability of the point $(0,0)$ is destroyed and it bifurcates into two new stable fixed points $\left(\pm\sqrt{1-\frac{1}{\Lambda^2}}, 2\pi n\right)$, as previously discussed. The trajectories for symmetric initial points z and $-z$ which originally share the same orbit are delimited by a separatrix and orbit around the new stable points. If the absolute value $|z|$ is large enough, the separated trajectories will merge again.

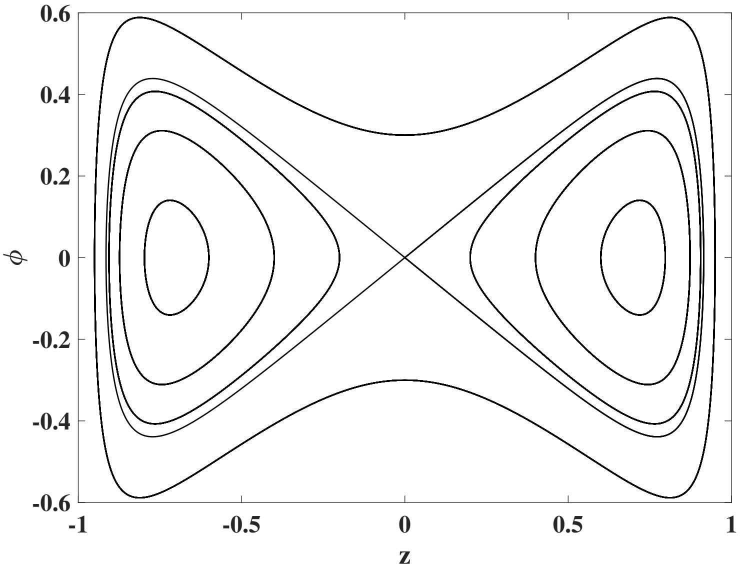

Fig. 4.3 Phase space trajectories with attractive interaction $U = -0.15J$ which leads to the emergence of the bifurcation. Initial values of z are varied with fixed $\phi = 0$. The total number of particles is $S = 20$.

4.5.2 Beyond mean-field theory

The previous subsection dealt with the BJJ in the framework of mean-field theory where only a single SU(2) GCS is employed. However, this method is only rigorously exact when the interaction strength $U = 0$, because if the interaction comes into effect, the solution will deviate from the SU(2) GCS, as discussed below Eq. (3.9), leading to the depletion of the condensate. A typical example is that when $U/J \to \infty$ the ground state of the Josephson junction from the diagonalization of the Hamiltonian in complete Fock space is given by $|\frac{S}{2}, \frac{S}{2}\rangle$, instead of the SU(2) GCS predicted by mean-field theory, despite having the same average population per site.

In order to account for quantum effects beyond mean-field theory, we will employ our basis function expansion, Eq. (4.3), specialized to the two-site model

$$|\Psi(t)\rangle = \sum_{k=1}^{N} A_k(t)|S, \xi_{k1}(t), \xi_{k2}(t)\rangle. \tag{4.67}$$

We will use this simple model to illustrate how well our basis function expansion works [136]. It is worth noting that we have reused the complex parameters in the basis function, the underlying reason is that complex parameters can simplify the derivation of equations of motion by getting rid of the nonlinear terms such as $\sqrt{\frac{1+z(t)}{2}}$ in Eq. (4.46). The parameter space of the basis functions is shown by the diagram in Fig. 4.4, involving two complex planes.

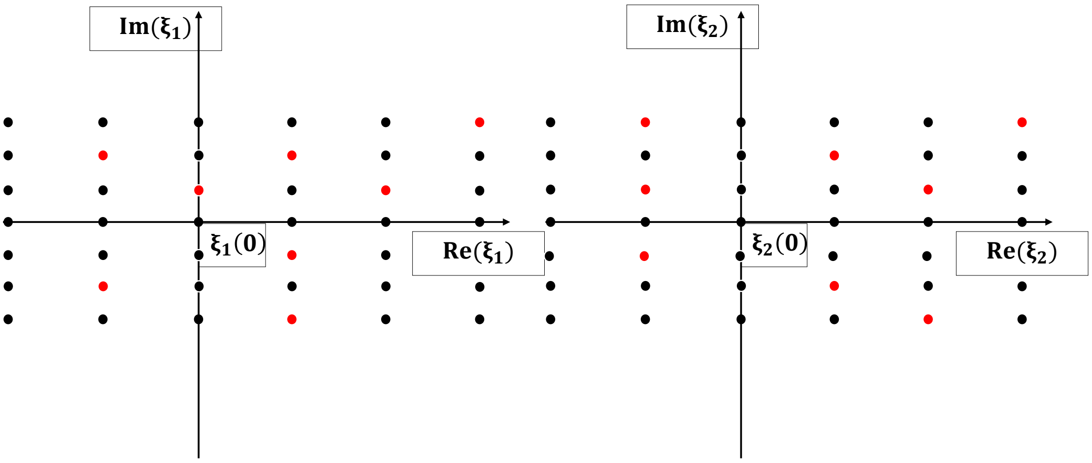

Fig. 4.4 The complex grids for ξ_1 and ξ_2 in the case of two modes. They are centered around $\{\xi_1(0), \xi_2(0)\}$ given by the GCS parameters of the initial state. We stress that there are only 8 pairs of points and not 64.

The initial state is an SU(2) coherent state, characterized by parameters $\xi_1(0)$ and $\xi_2(0)$ located at the origin. Then we produce a regular array of points in the complex plane. We note that the distance between these points, which can be adjusted, impacts the performance of our basis set. In general, a smaller distance between the points results in a more accurate outcome. However, we must avoid reducing the distance excessively, as this could lead to the singularity issue mentioned previously. This problem also occurs in the case of basis functions based on Glauber CS [70]. The effects of the grid spacing are discussed in detail in Appendix. C.

To create additional basis functions beyond the initial state in Eq.(4.67), we randomly sample some pairs of points in close proximity to the origin. This is illustrated by the 8 pairs of red points in Fig. 4.4, with each pair representing a SU(2) CS, so in total we have 9 basis functions in our basis set. When $t = 0$, the coefficient in Eq. (4.67) in front of the initial state is 1 while others are set to be equal to zero. When $t > 0$ the onset of the evolution will allow all basis functions to participate in the propagation, and all coefficients eventually will become nonzero.

Here, we note that the strategy of random sampling is important when we deal with many-body systems. The reason is that utilizing regular grids as depicted in Fig. 2.2 leads to an exponential increase in computational effort with increasing system size. For example, consider a regular grid composed of 20 points per mode; the total number of basis functions for M modes is $N = 20^M$. So the practical solution is to take a set of random samples from M regular grids to form a single basis function, and the total number of basis functions, N, is tailored to meet specific accuracy requirements.

Next, we will examine different initial states and various system parameters to evaluate the effectiveness of our approach.

Quantum phase operator

To begin with, we introduce the concept of the quantum phase operators [112] as the relative phase in Eq. (4.67) is ill-defined in quantum theory. A proper definition is given by

$$\cos\hat{\phi} := \frac{\hat{a}_2^\dagger \hat{a}_1 + \hat{a}_2 \hat{a}_1^\dagger}{\sqrt{2(2\hat{n}_1\hat{n}_2 + \hat{n}_1 + \hat{n}_2)}} \tag{4.68}$$

$$\sin\hat{\phi} := \frac{\mathrm{i}(\hat{a}_1^\dagger \hat{a}_2 - \hat{a}_2^\dagger \hat{a}_1)}{\sqrt{2(2\hat{n}_1\hat{n}_2 + \hat{n}_1 + \hat{n}_2)}} \tag{4.69}$$

where the factor in the denominator is introduced to ensure the normalization condition $\langle \sin^2\hat{\phi} + \cos^2\hat{\phi} \rangle = 1$. The definition of $\sin\hat{\phi}$ is similar with the current operator which counts the net particle current from the right side to the left side. In addition, the variance of the sine is defined by

$$\varDelta(\sin\hat{\phi}) := \langle \sin^2\hat{\phi} \rangle - \langle \sin\hat{\phi} \rangle \tag{4.70}$$

which can be applied to measure the phase fluctuation between two sites.

The relation between the sine of the relative phase and the expectation of the sine of the quantum phase is

$$\langle \sin\hat{\phi} \rangle = \frac{S\sqrt{1-z^2}}{\sqrt{S(S-1)(1-z^2)+2S}} \sin\phi, \tag{4.71}$$

as can be derived by applying the operator in Eq. (4.69) to an SU(2) GCS. For $S \to \infty$, the prefactor on the RHS of the above equation becomes unity and the quantum and classical expressions become identical. By introducing the expectation values of the quantum phase operators, we can study the trajectories of a quantum state in the phase space composed of the imbalance z and $\langle \sin\hat{\phi} \rangle$. But we should emphasize that in the quantum domain, the uncertainty principle precludes the existence of definite trajectories, and what we study here is based on the expectation values, thus the variance or fluctuation of the quantum quantities are lacking in the phase space description.

Plasma oscillations

The first scenario we will consider is the case of $\Lambda > -1$, with a initial state close to the stable equilibrium point $(0,0)$.

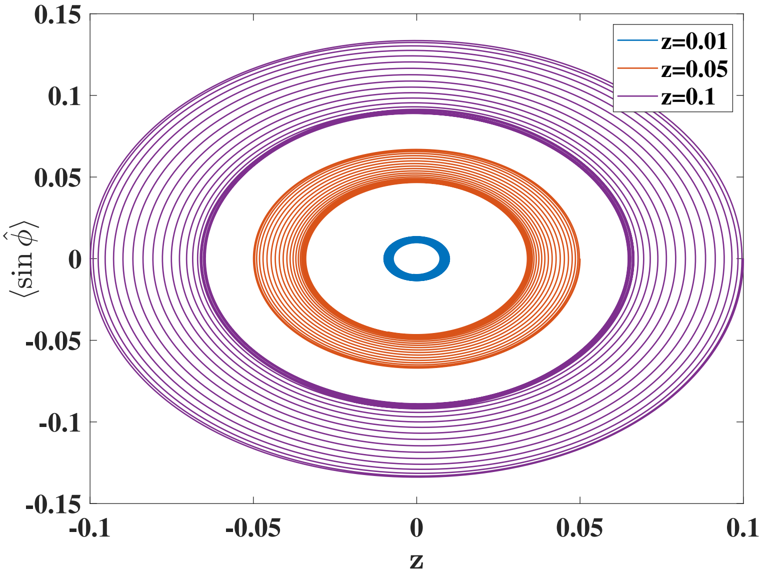

Fig. 4.5 Phase space trajectories for different initial conditions are indicated by different line styles: $z = 0.01$ (solid blue), $z = 0.05$ (dashed red), $z = 0.1$ (dash-dotted yellow). System parameters are $U/J = 0.1$ and $S = 20$. The total evolution time is $Jt = 50$. The total number of basis functions is $N = 5$.

In Fig. 4.5, the interaction strength is $U/J = 0.1$ and the number of particles is $S = 20$. We vary the initial imbalance and present the results from our improved basis function expansion calculation. In mean-field approximation all three initial conditions give rise to an ellipsoidal pattern as shown in the previous section. Notably, if we go beyond the mean-field approximation by employing 5 SU(2) GCS, we observe a distinctly different behavior. This corresponds to a "beating" pattern of the population imbalance and the quantum phase expectation value, characterized by a spiraling motion that first contracts inward then expands outward over a long evolution time for all three initial conditions. These results align with those obtained from an exact numerical calculation, which are not displayed here (for more information, we refer to [136]). The success of our basis function expansion with a small N arises from the fact that in this setting, the evolution doesn't go far beyond the validity of mean-field dynamics. When we initiate the dynamics with a larger imbalance $z = 0.5$, the beating effect will become more dramatic. As is shown in Fig. 4.6, the trajectories spiral inward closely to $(0,0)$ especially when S is large, while the classical trajectories still follow the simple elliptical pattern shown in Fig. 4.2. To ensure good alignment with the exact numerical results, here we employ 8 and 20 basis functions for $S = 20$ and 50, respectively. This larger number of basis functions implies that we need to take more efforts to recover the quantum dynamics when the starting point substantially deviates from the classical fixed point.

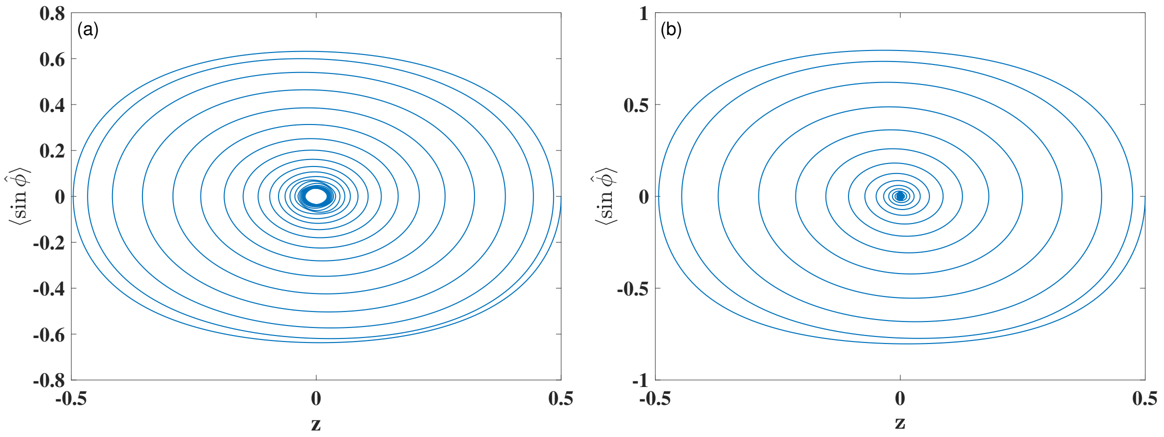

Fig. 4.6 Phase space trajectories for times up to $Jt = 50$ in the case $U/J = 0.1$ for (a) $S = 20$ and (b) $S = 50$. The initial condition is $z = 0.5$ in both cases.

In Fig. 4.7, we focus on the dynamics of the expectation values of the phase operator as well as the phase variance. The evolution time is extended to be $Jt = 100$. We can see that both cases display the beating where the amplitude of the oscillation is significantly suppressed, with the revival time for $S = 50$ being significantly longer than that for $S = 20$. It is also worthwhile to note that a suppressed amplitude coincides with a large variance of the phase operator, which shows that the fluctuation of the phase peaks when the expectation value is minimal. Given that the SU(2) GCS possesses a well-defined relative phase — indicating zero phase fluctuation — it is logical to expect that more basis functions will be needed to be employed to accurately represent the full quantum results.

Another way to explain the higher numerical effort makes use of the Husimi function, similar

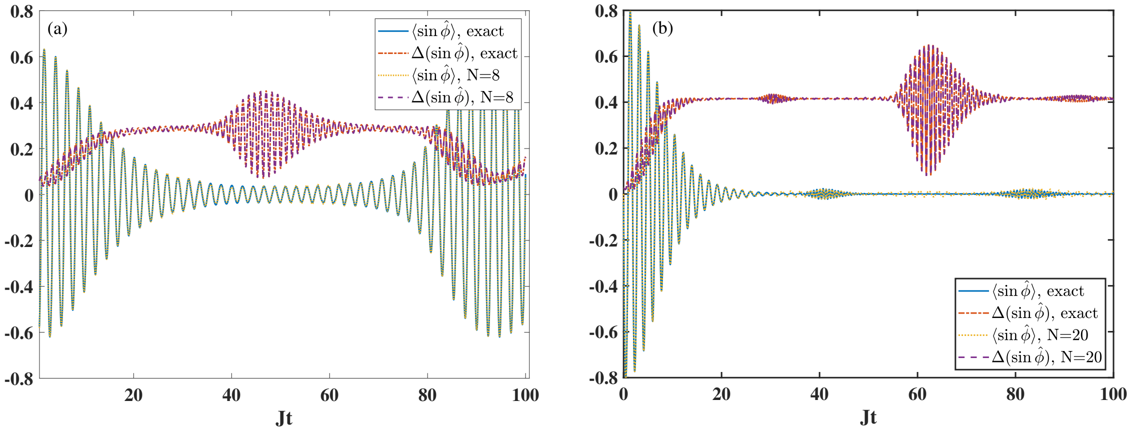

Fig. 4.7 The dynamics of the expectation of the phase operator and the corresponding variances for (a) $S = 20$ and (b) $S = 50$. The initial condition is $z = 0.5$ in both cases. The system parameter is U/J = 0.1. The expectation value of the sine of the phase (exact results: solid blue line, multi ACS results: dotted yellow line) and its variance (exact results: dash-dotted red line, multi ACS results: dashed purple line) are displayed.

.

to Eq. (3.3) but defined for an SU(2) GCS as

$$Q(z,\phi) = |\langle\Omega(z,\phi)|\Psi(t)\rangle|^2 \tag{4.72}$$

where

$$\Omega(z,\phi) = |S, \sqrt{\frac{1+z}{2}}, \sqrt{\frac{1-z}{2}}\mathrm{e}^{-\mathrm{i}\phi}\rangle \tag{4.73}$$

with z ranging from -1 to 1 and ϕ ranging from $-\pi$ to π. This function enables us to get the explicit distribution in phase space of the time-evolved states. In Fig. 4.8, the initial state is located near the stable fixed point and snapshots of the distribution are taken at different time. When $Jt = 0$, the distribution of an initial SU(2) coherent state is presented by a radially decaying spot whose center is the initial point. As the evolution starts, the distribution deviates from the initial spot but still maintains a simple structure, indicating that a large fraction of the state is still a SU(2) GCS. This explains why only a few basis functions are sufficient to simulate this dynamics.

However, in Fig. 4.9, when the initial state is distant from the stable point, the time-evolved state exhibits a more complicated distribution and the distribution changes rapidly with time, although it is still centered around $(0,0)$. Consequently, a larger number of basis functions is required to adequately capture and represent this distribution.

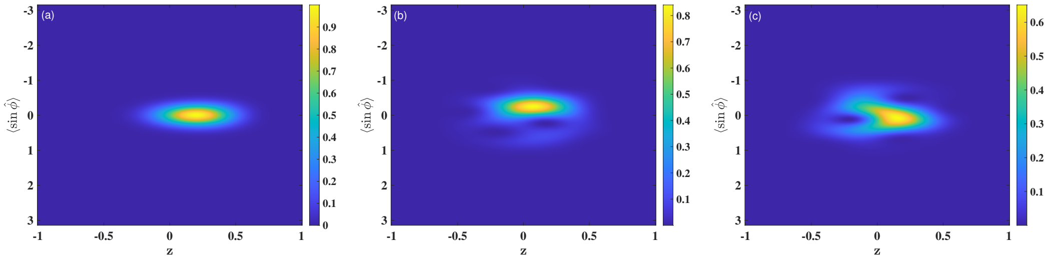

Fig. 4.8 The Husimi function projecting the time-evolved state onto arbitrary SU(2) coherent states whose imbalance ranges from -1 to 1 and relative phase varies from $-\pi$ to π. The function is depicted for different evolution time (a) $Jt = 0$, (b) $Jt = 20$ and $Jt = 50$ with $N = 10$ basis functions. The initial imbalance is $z = 0.2$ and the relative phase is 0. The interaction strength is set to $U = 0.1J$ and the particle number is $S = 50$.

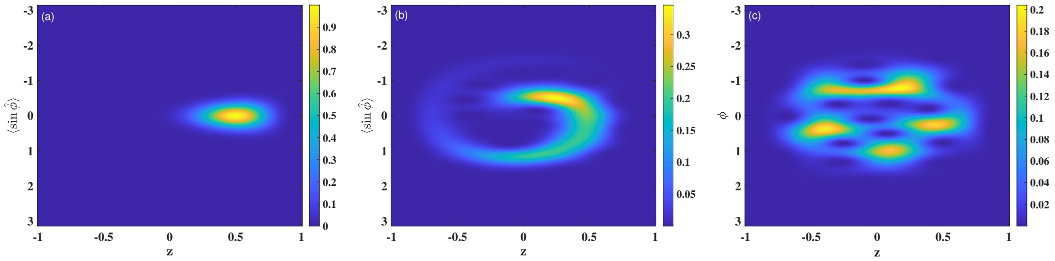

Fig. 4.9 Husimi function for a time-evolved state with initial conditions $z = 0.5$ and $\phi = 0$. The evolution times are (a) $Jt = 0$, (b) $Jt = 10$ and (c) $Jt = 50$. $N = 20$ basis functions are employed in order to achieve a good agreement with the exact numerical result. The system parameters are $U = 0.1J$ and $S = 50$.

Spontaneous symmetry breaking

In the following discussion we want to explore the case of $\Lambda < -1$,with a specific focus on the dynamical characteristics around the unstable fixed point at $(0,0)$, along with two new stable points at $\left(\pm\sqrt{1-\frac{1}{\Lambda^2}}, 2\pi n\right)$. The corresponding SU(2) GCS characterized by the new stable points are degenerate ground states with spontaneous symmetry-breaking (SSB) on the mean-field theory level.

As displayed in Fig. 4.10, we examine an attractive interaction $U = -0.12J$, while varying the initial imbalance throughout the entire interval $(-1,1)$. We firstly present the results for $S = 20$. In contrast to the classical results in Fig. 4.3, trajectories move in a seemingly random fashion, regardless of whether the initial imbalance is near the unstable fixed point or the stable fixed points. When z is initiated with values close to the point $(0,0)$, the dynamics is still chaotic. However, the trajectories around the fixed point $(\pm 0.94, 0)$ have a similar behavior as their classical counterparts in Fig. 4.3 but with the spiraling motion, which has been shown in Fig. 4.5.

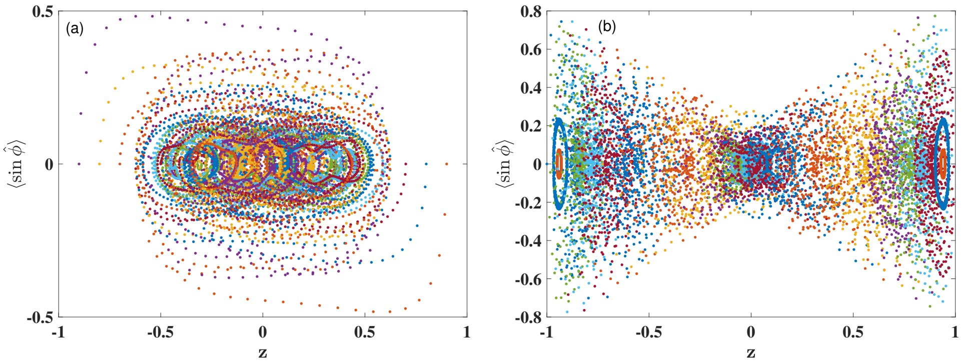

Fig. 4.10 The trajectories described by discrete points when $\Lambda < -1$. Initially $\phi = 0$ and the initial imbalance z varies in the region $(-1, 1)$, and the evolution time is $Jt = 50$. The situations for different particle numbers (a) $S = 20$ and (b) $S = 50$ are studied by employing $N = 8$ and $N = 18$ basis functions, respectively. The interaction strength is fixed to be $U = -0.12J$.

The influence of different S on these trajectories around the stable fixed point can be clarified further in Fig. 4.11, where the initial imbalance is in proximity to the stable points determined by $\sqrt{1-\frac{1}{\Lambda^2}}$ (noticing different S leads to different Λ). It is evident that the pattern of the quantum trajectories gradually collapse to the classical ones with increasing particle number. This is due to the fact that the limit of $S \to \infty$ for small number of sites corresponding to the classical limit gives the mean-field dynamics as shown in Eq. (4.31).

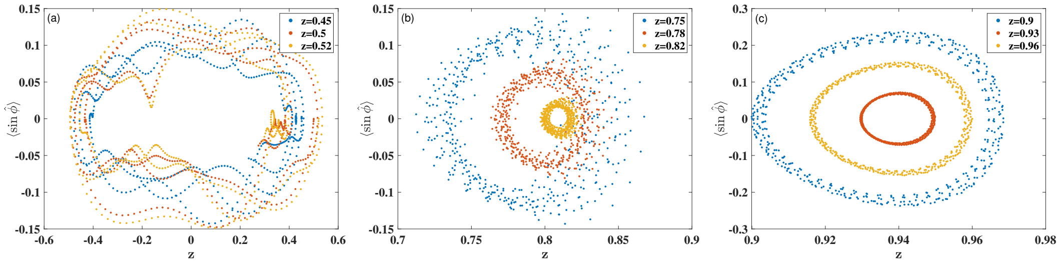

Fig. 4.11 The trajectories with the initial imbalance near $\sqrt{1-\frac{1}{\Lambda^2}}$ for different numbers of particles (a) $S = 20$, (b) $S = 30$, and (c) $S = 50$. The evolution time is $Jt = 50$ employing $N = 10$ basis functions. The interaction strength is set to be $U = -0.12J$.

These results also inspire us to predict the onset of the SSB from a dynamical point of view. In the context of quantum theory, the ground state can be expanded in terms of Fock state basis functions

$$|\mathrm{GS}\rangle = \sum_{\mathrm{n}_1=1}^{\mathrm{S}} \mathrm{c}_{\mathrm{n}_1} |\mathrm{n}_1, \mathrm{S}-\mathrm{n}_1\rangle, \tag{4.74}$$

characterizing SSB through the formation of the bimodal structure of $|c_{n_1}|^2$, namely, the ground state approaches the superposition

$$|S,0\rangle + |0,S\rangle$$

[137], and the coupling between $|S,0\rangle$ and $|0,S\rangle$ will be very weak when S is large [99]. As proved in [127], the absolute values of interaction strength U leading to the bimodal structure are generally larger than the values obtained by the mean-field theory $|U| = \frac{2J}{S-1}$, especially when the particle number is small. This discrepancy is reflected by the dynamics in the way that the quantum trajectories around the points $\left(\pm\sqrt{1-\frac{1}{\Lambda^2}}, 2\pi n\right)$ are not stable or localized as depicted in panel (a) of Fig. 4.11 for small S. The question is if we can use our basis function expansion to give a more precise critical value of U for the onset of SSB.

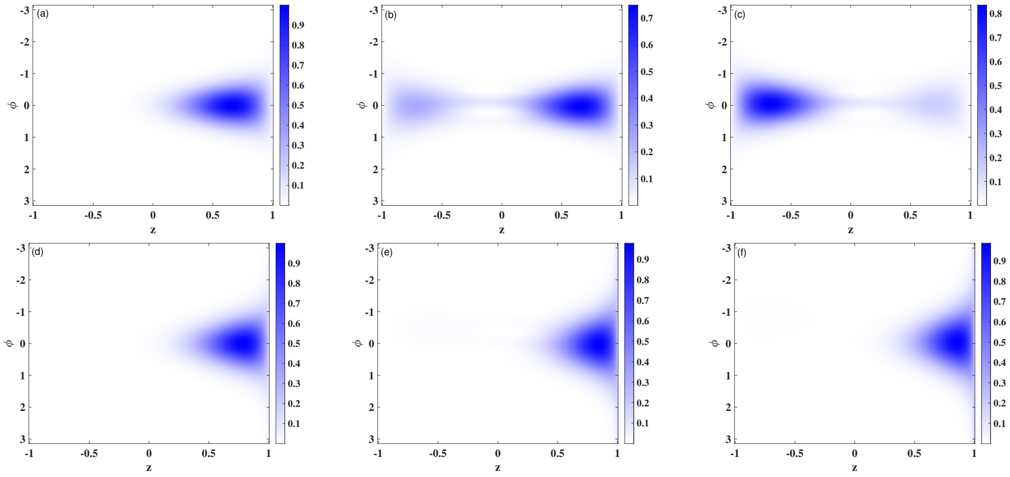

Fig. 4.12 Snapshots of beyond mean-field ($N = 2$) Husimi distributions for $S = 20$ and different on-site coupling strengths and times: (a)-(c): $U/J = -0.15$ and $t = 0$ (a) $t = 200$ (b) and $t = 300$ (c); (d)-(f): $U/J = -0.19$ and $t = 0$ (d) $t = 200$ (e) and $t = 300$ (f). The initial condition for z is $z_{SSB} - 0.05$ with $z_{SSB} = 0.71$ for panels (a)-(c) and $z_{SSB} = 0.83$ for panels (d)-(f).

To explore this possibility, we use two SU(2) GCS - the initial state and a randomly sampled state - and plot snapshots of the Husimi function for varying values of U. In Fig. 4.12 for the case of $S = 20$, the $U = -0.15J$, satisfying the criterion of mean-field theory $\Lambda < -1$ is initially chosen in panel (a)-(c) and the initial condition is $(z_{SSB} - 0.05, 0)$ where $z_{SSB} = \sqrt{1-\frac{1}{\Lambda^2}}$. The results shows that the main distribution is transferred from the right site to the left side over time, suggesting that the quantum dynamics is not stable around the classically stable fixed points. However, if the strength is set to be $U = -0.19J$, and simultaneously the initial condition z_{SSB} is also updated by the different value of U, we can see that the distribution remains localized around the initial point. Physically speaking, when $|U|$ is large enough, the SU(2) GCS $\left(\sqrt{1-\frac{1}{\Lambda^2}}, 2\pi n\right)$ and $\left(-\sqrt{1-\frac{1}{\Lambda^2}}, 2\pi n\right)$ are approximated to be the Fock states $|S,0\rangle$ and $|0,S\rangle$, respectively, and the coupling between these two states is substantially small since this macroscopic transition would have to overcome a high energy barrier [99].

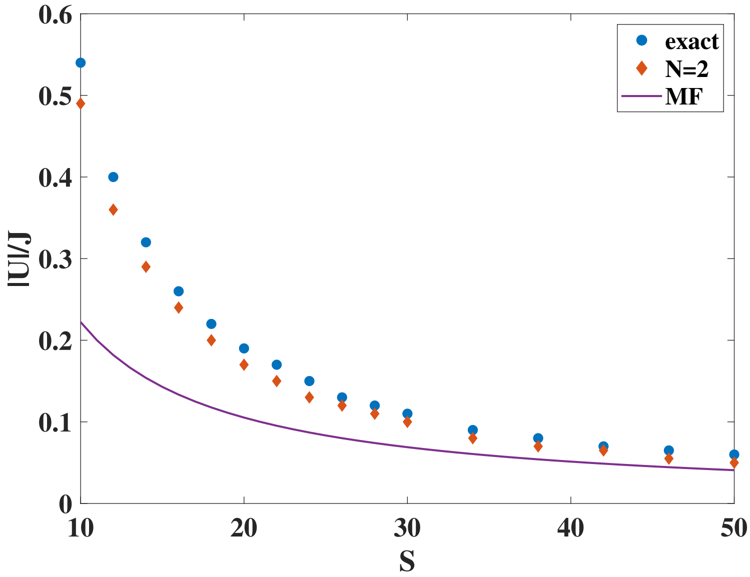

Fig. 4.13 Comparison of the onset of SSB as a function of |U|/J predicted by: (i) Mean field (solid line), (ii) multi-configuration with $N = 2$ (red diamonds) and (iii) exact result (blue dots), inferred from bimodality of ground state.

.

Furthermore, if we treat the dynamical stability and asymmetry of the Husimi function as the criterion for the onset of SSB, we can enhance the accuracy of the critical values for U. In Fig. 4.13, we have propagated the dynamics for large enough times ($Jt = 1000$) to confirm whether the distribution is confined to the right-hand side of phase space (i.e., $z > 0$) or not. An interval nesting strategy is employed to pinpoint the onset of SSB. These two results are then compared to the exact quantum ones (blue dots), calculated by monitoring the expansion of the ground state in terms of Fock states. Once the coefficients' magnitude displays a bimodal structure, the SSB range is assumed to be reached. Notably, the improved basis function expansion calculations with $N = 2$ exhibit a surprisingly close match with the exact quantum results, even for the case of a small number of particles.

4.6 Numerical appetizer II:Three-mode BH model

In the last section, we have explored some dynamical characteristics of the simple two-mode case, and the absolute values of interaction strength U we have considered are relatively small. To further substantiate the validity of our method, in the following we will delve into the dynamics of the three-mode BH model. Our goal is to study the impact of the interaction strength on the dynamics, especially when the system undergoes the transition from the weak interaction region to the strong interaction region with accompanying dynamical phenomena such as the depletion of the condensate. The Hamiltonian of this model with nearest-neighboring coupling is expressed as

$$\hat{H} = -J\sum_{\langle i,j\rangle}^{3}(\hat{a}_j^\dagger \hat{a}_j + h.c.) + \frac{U}{2}\sum_{i=1}^{3}\hat{a}_i^{\dagger 2}\hat{a}_i^2 + \sum_{i=1}^{3}\varepsilon_i \hat{a}_i^\dagger \hat{a}_i \tag{4.75}$$

where the first term couples the three sites together to form a chain or ring, the second term denotes the on-site interaction and the third term arises from the external trapping with the energy offset ε_i.

Let's firstly review the mean-field results for three-site BH model by following [32]. To describe the three-site case, SU(3) GCS of the form

$$\frac{1}{\sqrt{S!}}\left(\sum_{i=1}^{3}\xi_i \hat{a}_i^\dagger\right)^S |0,0,0\rangle$$

will be used. The corresponding Lagrangian for such single GCS is given by

$$L = \mathrm{i}S\sum_{i=1}^{3}\dot{\xi}_i\xi_i^* - \langle S,\vec{\xi}|\hat{H}|S,\vec{\xi}\rangle \tag{4.76}$$

where

$$\langle S,\vec{\xi}|\hat{H}|S,\vec{\xi}\rangle = -J\sum_{\langle i,j\rangle}(\xi_i^*\xi_j + \xi_j^*\xi_i) + U(S-1)\sum_{i=1}^{3}|\xi_i|^4 + \sum_{i=1}^{3}\varepsilon_i|\xi_i|^2. \tag{4.77}$$

The solutions of the corresponding discrete nonlinear Schrödinger equations Eq. (4.31)

$$\mathrm{i}\frac{d\xi_i}{dt} = -J\sum_{j\neq i}\xi_i + U(S-1)|\xi_i|^2\xi_i + \varepsilon_i\xi_i, \quad i = 1,2,3. \tag{4.78}$$

give the classical limit of the quantum system. Taking into account the normalization condition and the irrelevant global phase, the three complex variables ξ_i can be reduced to four real variables. Specifically, the $\{\xi_1, \xi_2, \xi_3\}$ can be rewritten as $\xi_1 = z_1 \mathrm{e}^{-i\phi_1}$, $\xi_3 = z_3 \mathrm{e}^{-i\phi_3}$ and $\xi_2 = z_2 = \sqrt{1-z_1-z_3}$, where z_i are the population densities of i-th site, while ϕ_1 and ϕ_3 denote the phase differences of the second site relative to the first and third site, respectively. Using this set of variables $\{z_1, \phi_1, z_3, \phi_3\}$, the Lagrangian (divided by S) is converted to

$$L = \dot{\phi}_1 z_1 + \dot{\phi}_3 z_3 - \tilde{H} \tag{4.79}$$

where the classical Hamiltonian $\tilde{H} = \langle \hat{H} \rangle / S$ of Eq. (4.75) per particle is written as

$$\begin{aligned} \tilde{H} = & -2J \left[\sqrt{1-z_1-z_3}\sqrt{z_1}\cos\phi_1 + \sqrt{1-z_1-z_3}\sqrt{z_3}\cos\phi_3 + \sqrt{z_1 z_3}\cos(\phi_1 - \phi_3) \right] \\ & + \frac{U(S-1)}{2}\left[z_1^2 + z_3^2 + (1-z_1-z_3)^2 \right] + \varepsilon_1 z_1 + \varepsilon_2 (1-z_1-z_3) + \varepsilon_3 z_3. \end{aligned} \tag{4.80}$$

We note that the term $\sqrt{z_1 z_3}\cos(\phi_1 - \phi_3)$ in the first line only comes into play when considering periodic boundary condition. From Eq. (4.79), one can realize that ϕ_i and z_i play roles of canonical position and momentum variables, respectively. Consequently, the classical Hamiltonian gives rise to the equations of motion in the form of

$$\dot{z}_i = -\frac{\partial \tilde{H}}{\partial \phi_i}, \tag{4.81}$$

$$\dot{\phi}_i = \frac{\partial \tilde{H}}{\partial z_i}. \tag{4.82}$$

Alternatively, we can also solve three equations of Eq. (4.78) which have a more simple form and extract the values of $\{z_1, \phi_1, z_3, \phi_3\}$ from the complex ξ_i.

In contrast to the classical trajectories of the two-mode BH model that do not display any chaotic behavior, the dynamical trajectories of the three-mode case can manifest both regular and chaotic properties [138]. To visualize the trajectories in a plane, we fix the total energy $\tilde{H}$ and set the Poincaré section condition $\phi_1 = 0$ such that only two degrees of freedom $\{z_3, \phi_3\}$ are left. Fig. 4.14 is rendered using data from [32] to show the mixed phase space where different colors are used to distinguish among various types of trajectories. It is found that the trajectories denoted by blue around the elliptic fixed point are periodic, but they are further split into some regular islands (shown in red) which can be understood in the light of the Kolmogorow-Arnol'd-Moser theorem [139]. The chaotic sea colored in purple occupies the space outside these islands, while some quasiperiodic orbits depicted in green are apparent in the lower region. This result presents a typical picture of the transition from regular to

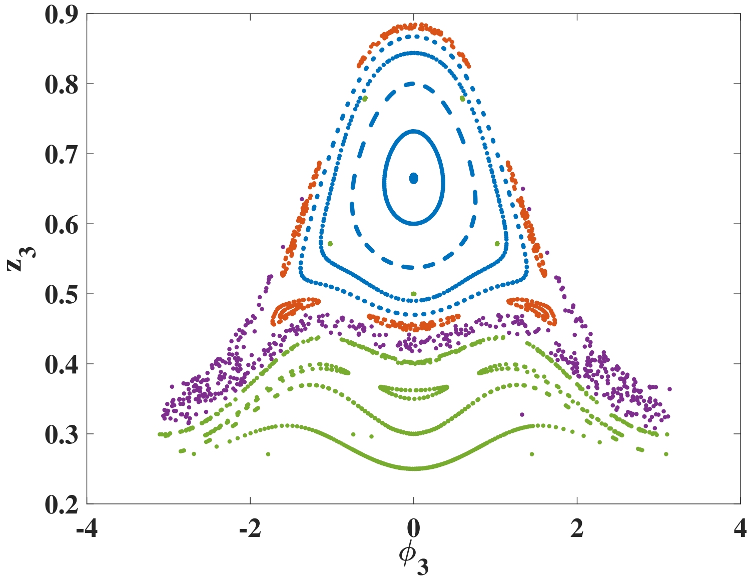

Fig. 4.14 The dynamical trajectories in the phase space comprised of z_3 and ϕ_3. The Poincaré section is chosen by setting $\phi_1 = 0$, while ensuring $\dot{\phi}_1 < 0$. The particle number is $S = 20$ and interaction strength $U = -0.25J$. The energy offset of every site is as follows: $\varepsilon_1 = 2J$, $\varepsilon_2 = 0$ and $\varepsilon_3 = 4J$. The total energy $\tilde{H}$ is fixed to be 1.

chaotic dynamics.

Although the above classical dynamics is rich in physics, our main goal in this section is to explore the quantum dynamics which is far beyond mean-field results. In Fig. 4.15, we investigate the population dynamics starting from an imbalanced initial state, specified by

$$|\psi(t)\rangle = \frac{1}{\sqrt{S!}}\left(\frac{1}{\sqrt{2}}\hat{a}_1^\dagger + \frac{1}{\sqrt{2}}\hat{a}_3^\dagger\right)^S |0,0,0\rangle, \tag{4.83}$$

where the second site is initially empty and the first and third sites have an equal population. We choose $U = 0.2J, 0.5J, 2J$ to analyze the population dynamics of the first site

$$S_1(t) = \langle\psi(t)|\hat{a}_1^\dagger\hat{a}_1|\psi(t)\rangle \tag{4.84}$$

and also study the convergence properties by increasing the number of basis functions. For $U = 0.2J$ (as shown in panel (a)), the exact dynamics oscillates with a slow damping effect, however, the result from the single basis function corresponding to the mean-field theory only presents a simple oscillation without damping. By increasing the number of basis functions to 10, we can successfully recover the exact dynamics.

When increasing the on-site interaction to $U = 0.5J$ (depicted in the panel (b)), the exact dynamics undergo a oscillation at the initial stage, followed by a significant suppression in

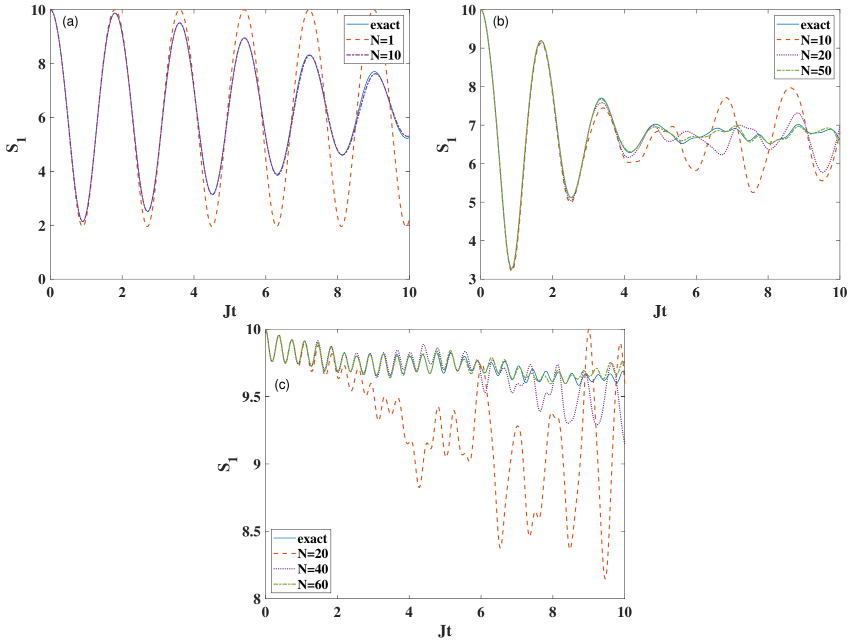

Fig. 4.15 The population dynamics of the first site initiated with the state $\frac{1}{\sqrt{S!}}\left(\frac{1}{\sqrt{2}}\hat{a}_1^\dagger+\frac{1}{\sqrt{2}}\hat{a}_3^\dagger\right)^S|0,0,0\rangle$, where $S=20$. The interaction strength is set as follows: (a) $U=0.2J$, (b) $U=0.5J$, and (c) $U=2J$. In each of the three cases, we utilize different numbers of basis functions to match the results obtained from exact numerical calculations.

.

the amplitude of the oscillation. After a long time, the wavefunction is close to a steady state with an equal population across all sites. In contrast to the previous case, the result using $N=10$ basis functions still exhibits a big deviation from the exact one, and only 50 basis functions can yield a satisfied outcome. Although in the second case the larger interaction strength required more numerical effort, it is worth noting that the dynamics with a small number of basis functions still captures some key dynamical features. For instance, with 20 basis functions, we can already observe the tendency toward the steady state

In panel (c) of Fig. 4.15 where the interaction strength is increased to $U=2J$, the exact result shows that the movement of the particles is dramatically suppressed while the small and rapid oscillation persists. This indicates that the dynamics is dominated by the on-site interaction, making the transport of particles among different sites difficult as it will cost a large amount of energy. In this scenario, even with 20 basis functions, we cannot obtain a reasonable prediction, indicating that more computational effort is required. These results confirm that our method has a better performance in the weak interaction region if we fix the value of J in a specific time window.

From the above results, we infer that the quantum result deviates from the mean-field theory

as the interaction strength is increased. Since the mean-field theory assumes that the time-evolved state is an ideal condensate, it can also be deduced that increasing the interaction strength will lead to the depletion of a pure condensate. This effect can be investigated by utilizing the single particle density matrix (SPDM).
For the three-mode case, the SPDM whose element is $\rho_{ij}^{\mathrm{SPDM}} = \langle \hat{a}_i^\dagger \hat{a}_j \rangle / S$ can be written as

$$\rho^{\mathrm{SPDM}} = \frac{1}{S} \begin{pmatrix} \langle \hat{a}_1^\dagger \hat{a}_1 \rangle & \langle \hat{a}_1^\dagger \hat{a}_2 \rangle & \langle \hat{a}_1^\dagger \hat{a}_3 \rangle \\ \langle \hat{a}_2^\dagger \hat{a}_1 \rangle & \langle \hat{a}_2^\dagger \hat{a}_2 \rangle & \langle \hat{a}_2^\dagger \hat{a}_3 \rangle \\ \langle \hat{a}_3^\dagger \hat{a}_1 \rangle & \langle \hat{a}_3^\dagger \hat{a}_2 \rangle & \langle \hat{a}_3^\dagger \hat{a}_3 \rangle \end{pmatrix}. \tag{4.85}$$

The maximal eigenvalue of the Hermitian matrix ρ^{SPDM} which is also called condensate fraction gives the information of macroscopic occupation of particles. Specifically, if the value is 1, the state is a pure condensate, while any values smaller than 1 indicate a deviation from the pure condensate [32].

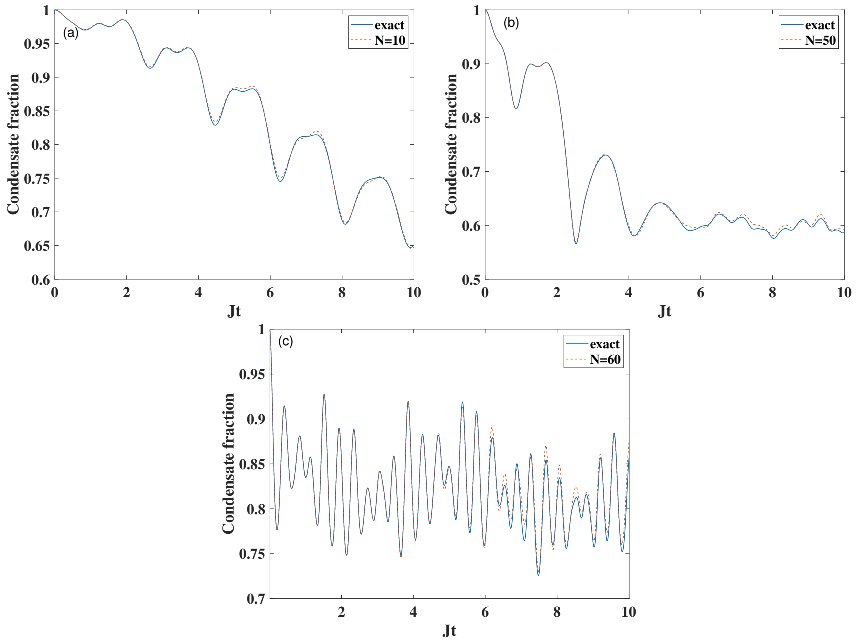

Fig. 4.16 The dynamics of the condensate fraction characterized by the maximal eigenvalue of the SPDM. The system parameters are same as the ones used in Fig. 4.15. Different numbers of basis functions are chosen to match the exact results.

In Fig. 4.16, we draw the dynamics of the condensate fraction with the same system parameters as the ones used for Fig. 4.15. As displayed in the left figure for $U = 0.2J$, the decrease in the condensate fraction happens gradually but non monotonously, which aligns with the slow damping of population dynamics displayed in the left figure of the Fig. 4.15, and this downward trend also illustrates that the effect of the interaction becomes more important with the time evolution. When $U = 0.5J$, the condensate fraction drops more quickly and stabilizes when $Jt > 4$, and such a stabilization has already been manifest in the middle figure of Fig. 4.15. Lastly, for $U = 2J$, the condensate fraction initially undergoes a rapid decrease suggesting that the interaction takes effect at the initial stage, and the subsequent oscillation is the result of the competition between the hopping and interaction effect. This complex dynamics is the distinctive characteristic of the Bose-Hubbard model in the strong interaction regime.

Chapter 5

Variational multi-layer GCS and thermalization

The two-site and three-site cases we discussed in Chapter. 4 are only appetizers in terms of numerical difficulty. Here, we will start to explore the dynamics of more challenging systems, with large lattice sizes M and also large particle numbers S.

The initial state studied is chosen to be a multimode Glauber CS, described by the displacement vector

$$\vec{\alpha} = (\alpha_1, \alpha_2, \cdots, \alpha_M),$$

where α_i denotes the characteristic parameter on the i-th site.

The choice of this state instead of GCS is motivated by several reasons. First, the multimode Glauber CS, independent of S also effectively describes the condensate [44] which is described by the discrete Gross-Pitaevskii equation (Eq. (4.32)) in the framework of mean-field theory. Moreover, applying the TWA method to a Glauber CS is straightforward, given its Gaussian Wigner function, enabling a comparative analysis of classical and quantum results which we aim for in this chapter.

5.1 Variational multi-layer GCS

In order to tackle the dynamics of multimode Glauber CS by using our variational method, we need to recall the relationship between Glauber CS and GCS as provided in Eq. (2.21)

$$|\vec{\alpha}\rangle = \mathrm{e}^{-\frac{\tilde{N}}{2}} \sum_{S=0}^{\infty} \frac{\tilde{N}^{\frac{S}{2}}}{\sqrt{S!}} |S, \vec{\xi}\rangle, \tag{5.1}$$

where $\tilde{N}=\sum_{i=1}^{M}|\alpha_i|^2$ denotes the average particle number. Given that the distribution for GCS with different S follows the Poisson distribution proved in Eq. (2.21), we only consider truncating Eq. (5.1) with S ranging in the interval $[S_1, S_2]$, such that the fidelity satisfies the following condition

$$\langle\vec{\alpha}|\tilde{\vec{\alpha}}\rangle = \mathrm{e}^{-\tilde{N}}\sum_{S=S_1}^{S_2}\frac{\tilde{N}^S}{S!} > 0.99, \tag{5.2}$$

to ensure that the numerical error of the initial state is smaller than 0.01. As a result, our initial state involves a set of GCS with different S values, and the subsequent evolution happens in this different S-particle subspace.

Specifically, our whole Ansätze for this problem is written as

$$|\Psi(t)\rangle = \sum_{S=S_1}^{S_2}\sum_{j=1}^{N}A_j^{(S)}(t)|S,\vec{\xi}_j^{(S)}(t)\rangle, \tag{5.3}$$

which has a multi-layer structure. In each layer labeled by particle number S, we employ N GCS basis functions, characterized by the variables $\vec{A}^{(S)},\vec{\xi}^{(S)}$. Initially, in every layer, the GCS with the characteristic parameters

$$\vec{\xi} = \frac{1}{\sqrt{\tilde{N}}}\{\alpha_1,\alpha_2,\cdots,\alpha_M\}$$

is the sole state that is populated. These basis functions evolve following the TDVP established in the preceding section. Upon completion of the evolution, we obtain the final state by applying a Poisson distribution-related factor to each layer, as expressed in the following equation:

$$|\Psi(t)\rangle_f = \sum_{S=S_1}^{S_2}\mathrm{e}^{-\frac{\tilde{N}}{2}}\frac{\tilde{N}^{\frac{S}{2}}}{\sqrt{S!}}\sum_{j=1}^{N}A_j^{(S)}(t)|S,\vec{\xi}_j^{(S)}(t)\rangle. \tag{5.4}$$

Benefiting from the $U(1)$ symmetry of the BH model, the dynamics in each layer evolves independently. This independence facilitates parallel computation across layers. We highlight again that our reliance on the variational GCS basis functions effectively circumvents the severe singular issues commonly associated with Glauber CS-like basis functions [70]. This is a significant advantage, even though using Glauber CS as basis functions might seem more intuitive for this case.

To evaluate the effectiveness of our variational multi-layer GCS described by Eq. (5.3), we investigate a four-site system which is still numerically solvable, using a Fock-state expansion, if the average particle number $\tilde{N}$ is not too large. We choose an initial state characterized as a half-filling Glauber CS, represented by

$$\vec{\alpha} = (\sqrt{20}, 0, \sqrt{20}, 0),$$

that was previously analyzed in [140]. In Fig. 5.1, we present the dynamics of the absolute

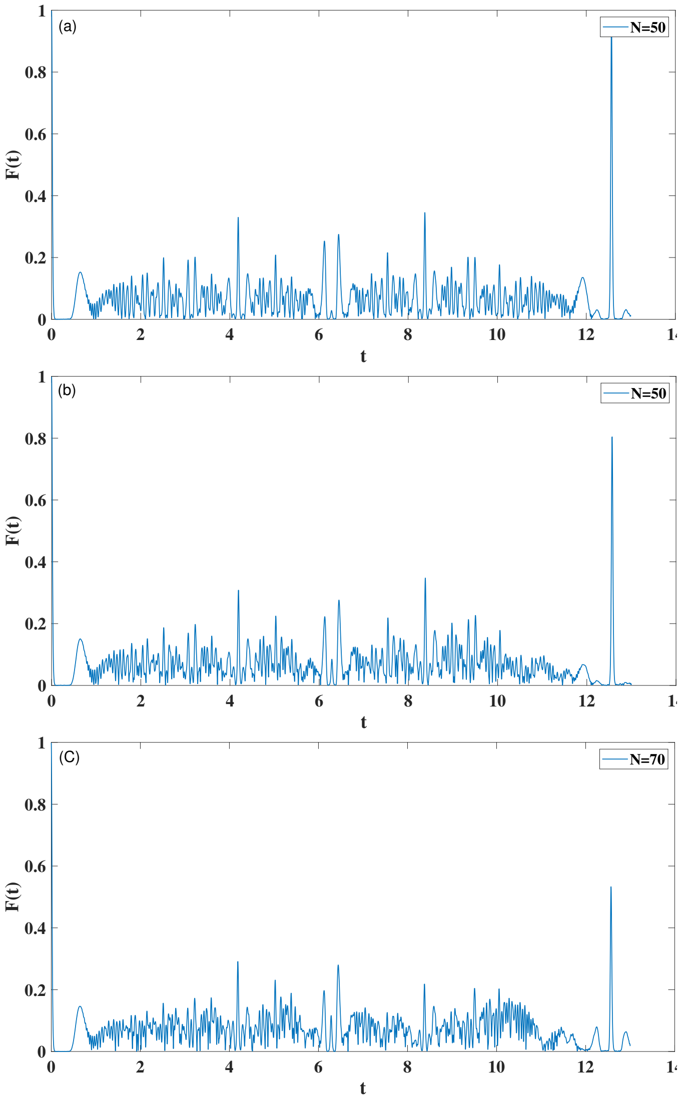

Fig. 5.1 The dynamics of the autocorrelation function for varying parameters: (a) $J = 0.1, U = 0.5$, (b) $J = 0.2, U = 0.5$ and (c) $J = 0.3, U = 0.5$. The initial state is the Glauber CS $\vec{\alpha} = [\sqrt{20}, 0, \sqrt{20}, 0]$ given in the main text. Different numbers of basis functions are used to generate the results. The particle number S in Eq. (5.3) ranges in the interval [21, 60].

value of autocorrelation function

$$F(t) = |\langle\vec{\alpha}|\mathrm{e}^{-\mathrm{i}\hat{H}t}|\vec{\alpha}\rangle|, \tag{5.5}$$

which can manifest a lot of dynamical details. The most significant phenomenon is that the survival probability at time $2\pi/U$ gradually decreases with increasing hopping strength J. From Eq. (3.2), we have learned that $2\pi/U$ is the revival period if $J = 0$, while nonzero values of J make the time-evolved state move away from the prediction of unit survival probability.

To quantify our variational approach for such a system, we compute the accumulated error throughout the time window

$$E = \int_0^t \mathrm{d}\tau |F_{\mathrm{GCS}}(\tau) - F_{\mathrm{exact}}(\tau)|, \tag{5.6}$$

where F_{GCS} denotes the results for $F(t)$ from our variational approach based on GCS, and F_{exact} is the exact numerical result. This accumulated error is plotted in Fig. 5.2 as a function of N for the case with $J = 0.3$ which is the most nonfavorable for variational approach. Remarkably, it is found that the error is suppressed exponentially by increasing the number of basis functions, and the required N to get a satisfactory result is around $N = 100$, which is considerably smaller than the corresponding Hilbert space dimension of the Fock basis.

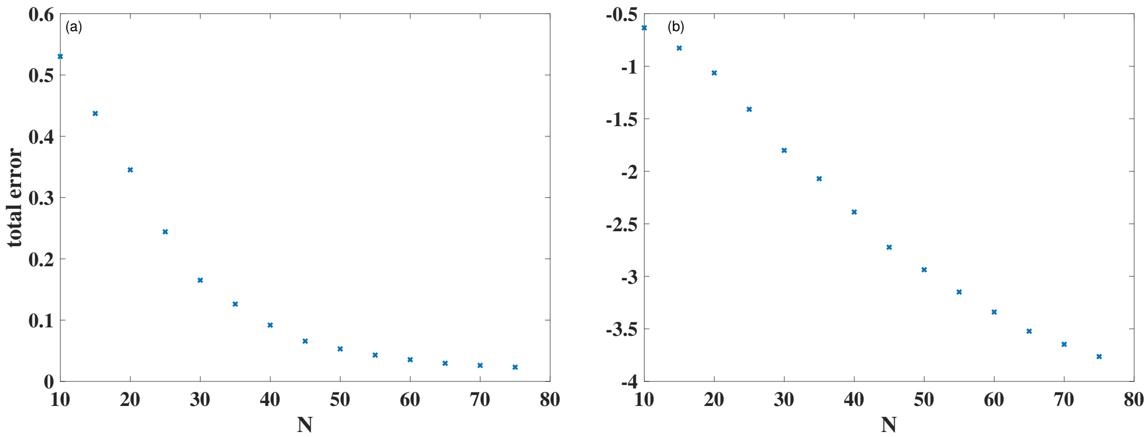

Fig. 5.2 (a) The accumulated error defined in Eq. (5.6) as a function of number of basis functions; (b) The y axis is set as the log of the accumulated error with the base e. The parameters of the system are taken from the panel (c) with $J = 0.3, U = 0.5$ in Fig. 5.1.

.

5.2 Truncated Wigner approximation

In this section, we offer a concise overview of the well-established TWA method, a significant method dealing with dynamics in bosonic systems [141, 142]. This approximation utilizes the Wigner representation, which is an alternative framework to describe quantum theory in phase space [143]. The Wigner function of a quantum state in phase space is defined as follows:

$$W(\boldsymbol{q},\boldsymbol{p}) \equiv \frac{1}{(2\pi)^M}\int_{-\infty}^{\infty} \mathrm{d}^M\boldsymbol{x}\left\langle \boldsymbol{q}+\frac{\boldsymbol{x}}{2}|\psi\right\rangle \langle\psi|\boldsymbol{q}-\frac{\boldsymbol{x}}{2}\rangle e^{-\mathrm{i}\boldsymbol{p}\cdot\boldsymbol{x}}, \tag{5.7}$$

where the reduced Plank constant $\hbar = 1$. $\boldsymbol{q}$ and $\boldsymbol{p}$ denote generalized position and momentum vectors in high dimensional space, respectively.
Noteworthy, the Wigner function of a Glauber CS $|\vec{\alpha}\rangle$ has the form of a Gaussian function

$$W(\boldsymbol{q},\boldsymbol{p}) = \frac{1}{\pi^M}\prod_{j=1}^{M}\exp\left[-(p_j-\tilde{p}_j)^2-(q_j-\tilde{q}_j)^2\right], \tag{5.8}$$

where $\tilde{q}_j = \sqrt{2}\mathrm{Re}[\alpha_j]$ and $\tilde{p}_j = \sqrt{2}\mathrm{Im}[\alpha_j]$ are the real and imaginary components of the displacement, respectively. In the TWA method, the evolution of the Wigner function is governed by the Liouville equation, which omits all quantum corrections, which are of higher orders in $\hbar^2$ [144]. The evolution can thus be represented as:

$$\frac{\mathrm{d}W}{\mathrm{d}t} = \{H, W(\boldsymbol{q},\boldsymbol{p})\} \tag{5.9}$$

where $\{\cdot\}$ symbolizes the Poisson bracket [139]. The Hamiltonian H in this context refers to the classical Hamiltonian for the TWA of the BH model which can be obtained within two steps. Firstly, we replace the the bosonic operators $\hat{a}_j$ and $\hat{a}_j^\dagger$ with position and momentum operators $(\hat{q}_j,\ \hat{p}_j)$ by the following relation

$$\hat{a}_j = \frac{1}{\sqrt{2}}(\hat{q}_j+\mathrm{i}\hat{p}_j),\ \hat{a}_j^\dagger = \frac{1}{\sqrt{2}}(\hat{q}_j-\mathrm{i}\hat{p}_j). \tag{5.10}$$

As a result, the quantum Hamiltonian Eq. (4.2) is converted to

$$\hat{H} = -J\sum_{i=1}^{M}(\hat{q}_i\hat{q}_{i+1}+\hat{p}_i\hat{p}_{i+1})+\frac{U}{2}\sum_{i=1}^{M}\left(\frac{\hat{q}_i^2+\hat{p}_i^2}{2}\right)^2-U\sum_{i=1}^{M}\frac{\hat{q}_i^2+\hat{p}_i^2}{2} \tag{5.11}$$

where the last term is from the commutation relation

$$[\hat{q}_i,\ \hat{p}_j] = \mathrm{i}\delta_{ij}. \tag{5.12}$$

The second step is to replace the operators $(\hat{q}_j,\ \hat{p}_j)$ with c-numbers $(q_j,\ p_j)$, leading to the classical Hamiltonian H

$$H = -J\sum_{i=1}^{M}(q_iq_{i+1} + \hat{p}_ip_{i+1}) + \frac{U}{2}\sum_{i=1}^{M}\left(\frac{q_i^2+p_i^2}{2}\right)^2 - U\sum_{i=1}^{M}\frac{q_i^2+p_i^2}{2} \tag{5.13}$$

In this scenario, we have assumed periodic boundary conditions

$$q_{M+1} = q_1,\ p_{M+1} = p_1.$$

One can verify that the sum $\sum_{i=1}^{M}\left(\frac{q_i^2+p_i^2}{2}\right)$ remains constant throughout the dynamics, as indicated by:

$$\left\{\sum_{i=1}^{M}\left(\frac{q_i^2+p_i^2}{2}\right),\ H\right\} = 0. \tag{5.14}$$

This equation maintains the conservation of the average particle number under the TWA method.

We note that the classical Hamiltonian Eq. (5.13) for the TWA method exhibits a subtle difference from the one in mean-field theory. In the latter, the operators $\hat{a}_j^\dagger$ and $\hat{a}_j$ are directly substituted by the c-numbers $\alpha_j^* = \frac{1}{\sqrt{2}}(q_j + \mathrm{i}p_j)$ and $\alpha_j = \frac{1}{\sqrt{2}}(q_j - \mathrm{i}p_j)$ such that the last term in Eq. (5.13) will not show up (if normal ordering is used). This distinction arises because the TWA method accounts for the quantum fluctuations of the initial state in phase space which is caused by the commutator Eq. (2.2). Consequently, the corresponding Hamiltonian should also contain the effect of this non-commutativity.

Alternatively, the TWA method can also be implemented through a distinct process that involves sampling initial values in phase space. This process starts by selecting a set of initial conditions, denoted as $(\boldsymbol{q}_0, \boldsymbol{p}_0)$, based on the Wigner function as defined in Eq. (5.8). These initial conditions are then used to integrate the classical equations of motion for the system, which are formulated as follows:

$$\dot{q}_j = \frac{\partial H}{\partial p_j} = -J(p_{j+1} + p_{j-1}) + Up_j\left(\frac{q_j^2+p_j^2}{2}\right) - Up_j, \tag{5.15}$$

$$\dot{p}_j = -\frac{\partial H}{\partial q_j} = J(q_{j+1} + q_{j-1}) - Uq_j\left(\frac{q_j^2+p_j^2}{2}\right) + Uq_j. \tag{5.16}$$

Here, $\dot{q}_j$ and $\dot{p}_j$ represent the time derivatives of the elements of the generalized position and momentum vector, respectively. The values $(\boldsymbol{q}_t, \boldsymbol{p}_t)$ obtained through this integration represent the evolved state of the system at time t, and they can be used to calculate various observable quantities.

An important aspect of the TWA approach is that it encompasses the complete quantum information of the initial state within its Wigner function. However, the subsequent evolution of the system is approximated using classical dynamics. This distinction is crucial as it highlights the TWA method's approach to dealing with quantum systems using classical mechanics trajectories.

For the half-filling initial state, a key quantity of interest is the dynamics of the particle population on odd-numbered sites. This can be quantitatively assessed using

$$N_{\text{odd}} = \frac{1}{N} \sum_{j=1}^{N} \sum_{i=\text{odd}} \left(\frac{q_i^2 + p_i^2 - 1}{2} \right), \tag{5.17}$$

where N represents the total number of sampled pairs (q_j, p_j). The term -1 in the numerator of this equation stems from the commutator Eq. (5.12), when we replace the number operator for the j-th site by

$$\hat{a}_j^\dagger \hat{a}_j = \frac{\hat{q}_i^2 + \hat{p}_i^2 - 1}{2}. \tag{5.18}$$

Therefore, it is necessary to subtract this additional term to accurately reflect the true population dynamics.

5.3 Thermalization: classical and quantum

5.3.1 Eigenstate Thermalization Hypothesis

The thermalization of isolated systems is a fundamental topic in the study of non-equilibrium dynamics. Central to this discussion is the Eigenstate Thermalization Hypothesis (ETH), which argues that for a given local observable $\hat{O}$, its expectation value in an eigenstate of a generic many-body system is identical to the one in micro-canonical ensemble with the same energy. This hypothesis can be translated into

$$\langle E_\alpha | \hat{O} | E_\beta \rangle = \bar{O}_{\text{mc}}(E_\alpha) \delta_{\alpha\beta} + c_{\alpha\beta}, \tag{5.19}$$

where $|E_\alpha\rangle$ and $|E_\beta\rangle$ are two eigenstates of the many-body system with eigenenergies E_α and E_β, respectively. Moreover, $\bar{O}_{\mathrm{mc}}(E_\alpha)$ denotes the expectation value in the micro-canonical ensemble with energy E_α, and $c_{\alpha\beta}$ is a cross term which tends to be zero when the system size is large [145–147].

As a consequence, considering an initial state expressed as a superposition of a set of eigenstates:

$$|\Psi(t=0)\rangle = \sum_\alpha A_\alpha |E_\alpha\rangle, \tag{5.20}$$

a sufficiently long time evolution will lead to [147, 99]

$$\begin{aligned}\langle \hat{O}\rangle_{t\to\infty} &= \lim_{t\to\infty}\frac{1}{t}\int_0^t \mathrm{d}t\langle\Psi(t)|\hat{O}|\Psi(t)\rangle \\ &= \sum_\alpha |A_\alpha|^2\langle E_\alpha|\hat{O}|E_\alpha\rangle \\ &= \sum_\alpha |A_\alpha|^2\bar{O}_{\mathrm{mc}}(E_\alpha),\end{aligned} \tag{5.21}$$

where $\langle\hat{O}\rangle_{t\to\infty}$ denotes the infinite-time average of $\hat{O}$. If the variance of the initial state's energy E is small, Eq. (5.21) can be further approximated to be

$$\sum_\alpha |A_\alpha|^2\bar{O}_{\mathrm{mc}}(E_\alpha) \approx \bar{O}_{\mathrm{mc}}(E)\sum_\alpha |A_\alpha|^2 = \bar{O}_{\mathrm{mc}}(E). \tag{5.22}$$

Eq. (5.22) indicates that after long time evolution, the local observables of quantum many-body systems will finally reach the thermodynamic equilibrium predicted by classical statistics. This holds true even if the system's global state remains a pure state. Notably, the realistic process towards thermalization has been studied in ultracold atomic gases [103, 148, 149]. While the ETH predicts the eventual equilibration of generic many-body systems after ruling out some exceptional cases like many-body localization [147, 150], it does not give the dynamical details of the approach towards thermalization. Specifically, we can not infer from the ETH how the approach to thermalization in quantum systems deviates from classical dynamics. In next section, we will focus on examining the process of thermalization within the BH model through the application of our multi-layer GCS basis function expansion, and conduct a comparative study between the quantum results obtained from our variational approach and the classical results derived from the TWA method.

5.3.2 Numerical results

Our investigation focuses on exploring the dynamics of an 11-site BH model under periodic boundary conditions. The system is initialized in a half-filling multimode Glauber CS, defined by the following set of parameters:

$$\vec{\alpha} = [0, \sqrt{2}, 0, \sqrt{2}, 0, \sqrt{2}, 0, \sqrt{2}, 0, \sqrt{2}, 0].$$

In this configuration, the average particle number, denoted as $\tilde{N}$, is calculated based on the sum of the squares of the coherent state amplitudes on the even-numbered sites:

$$\tilde{N} = \sum_{i=\text{even}} |\alpha_i|^2 = 10.$$

Quantum Results

To use the multi-layer GCS Eq. (5.3), we take the particle number S of GCS ranging in the interval $[3,20]$ to ensure the fulfillment of the fidelity condition presented in Eq. (5.2).
To ensure that our results are reliable, in Fig. 5.3, our analysis centers on the long-term convergence behavior obtained from the variational approach, specifically examining how this behavior varies with different ratios of tunneling strength to on-site interaction strength $J/U = 0.25,\ 0.5,\ 1,\ 5$, which is similar with what we have performed for the three-site case. We use a logarithmic scale for the time axis in order to compress the (uniform) long-term behavior. For each of the four scenarios, we have increased the number of basis functions N as defined in Eq. (5.3) to test their convergence.
The results for varied U/J in Fig. 5.3 present a clear trend towards a stable convergence when increasing the number of basis functions N in a large region. However, in the case of strong interaction strength specifically for $J/U = 0.25$ as depicted in panel (a), it should be noted that despite employing a greater number of basis functions compared to other cases, there still remains a slight divergence among the different curves. For more extreme scenarios, beyond what displayed in Fig. 5.3, such as the case with $U/J = 0.1$ in Fig. 5.4, the deviation becomes more obvious, such that the number of basis functions needed to get stable convergence is not clear. This suggests that in regimes of strong interaction, achieving convergence will be more challenging, which is consistent with our previous discussion of the three-site case.
In the remaining three cases, especially in panels (c) and (d) of the figure with weaker interaction strengths, we observe the onset of convergence even when the number of basis functions N is relatively small, and the curves from different N match with each other closely. Thus, it is safe to say that for moderate value of U/J, the results from the variational approach lie in the correct dynamical region. We emphasize that the number of basis functions used

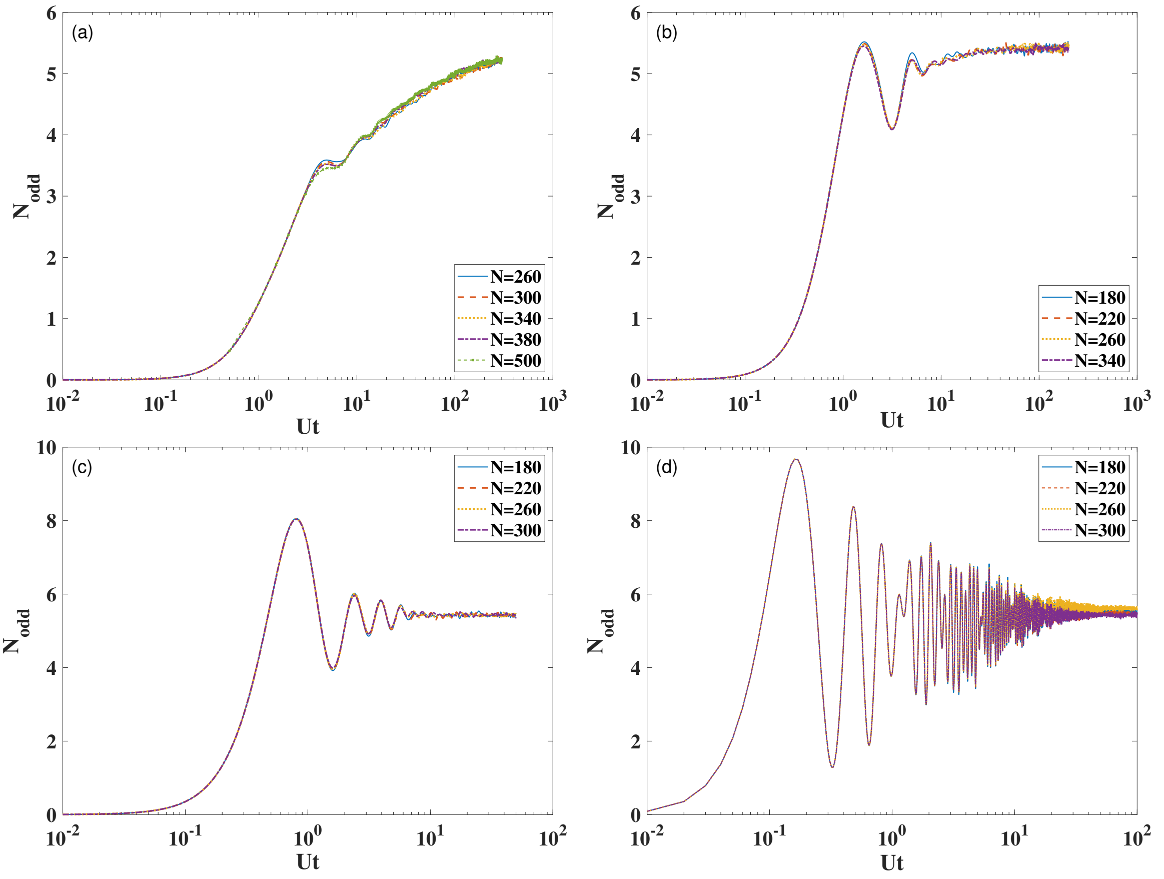

Fig. 5.3 Convergence of population dynamics of odd sites for different values of J/U: (a) $J/U = 0.25$ with $Ut \in [0,300]$, (b) $J/U = 0.5$ with $Ut \in [0,300]$, (c) $J/U = 1.0$ with $Ut \in [0,50]$ and (d) $J/U = 5.0$ with $Ut \in [0,100]$.

in our study, even for the case with the strongest interaction (as depicted in panel (a)), is confined to several hundreds which is very small compared to the dimension of the Hilbert space spanned by the Fock basis. In such systems, obtaining exact numerical results is already very challenging due to the computational demands.

The results in Fig. 5.3 and Fig. 5.4 also reveal how the approach to thermalization in the BH model is influenced by the interaction strength. In cases of weak interaction, where tunneling is dominant, the system's dynamics for N_{odd} approaches an equilibrium value, that is approximated by $\frac{6\times 10}{11}$ indicating that the particles distribute evenly cross all sites. This trend is accompanied by rapid oscillations because the weak interaction lifts the barrier to the movement of particles between sites. On the other hand, strong interaction strength tends to inhibit the dispersion of particles across different sites, thereby decreasing the rate of reaching equilibrium. Particularly, as the tunneling strength and on-site interaction are balanced, which is the case in panel (c) for $J/U = 1$, the system reaches its equilibrium state

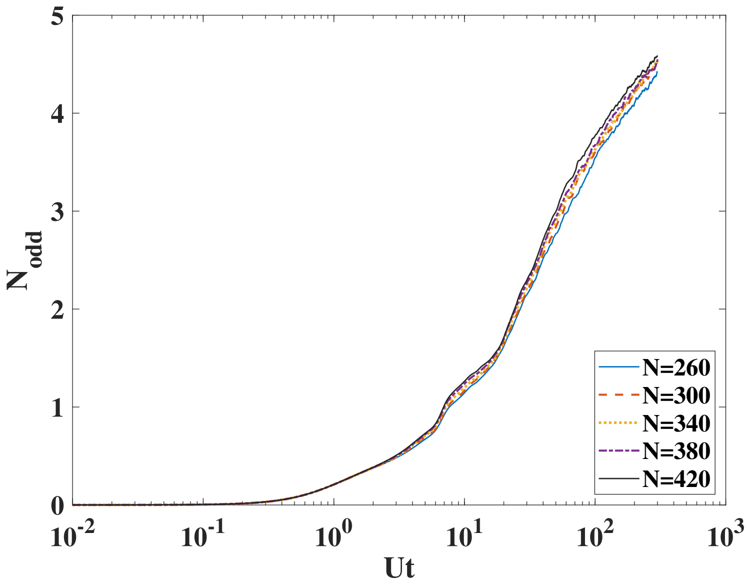

Fig. 5.4 Convergence of population dynamics on odd odd sites for $J/U = 0.1$ with $Ut \in [0,300]$

most rapidly. This balance facilitates a more efficient distribution of particles across the system and leads to a quicker approach to thermal equilibrium.

Comparison to classical results

Due to the existence of a classical counterpart of the BH model, we can conduct a comparison between the quantum dynamics from our variational approach, and classical dynamics described by TWA method. This comparison, depicted in Fig. 5.5, reveals key differences in how these two methods approach equilibrium under varying interaction strengths.

A striking difference between quantum and classical dynamics is observed in the cases of $J/U = 0.5$ and $J/U = 0.25$. In these cases, the classical dynamics matches with the quantum dynamics prior to $Ut \approx 1$, while it deviates noticeably from the quantum results in the subsequent evolution and tends to reach equilibrium at a slower pace. This contrasts with the results of weak interaction, where the classical and quantum dynamics approach to equilibrium at a similar rate.

In addition to exploring the effects of interaction strength, we extend our study to investigate how the average particle number influences the thermalization process in the BH model. For this purpose, we consider an initial state characterized by the parameter set:

$$\vec{\alpha} = [0,2,0,2,0,2,0,2,0,2,0]$$

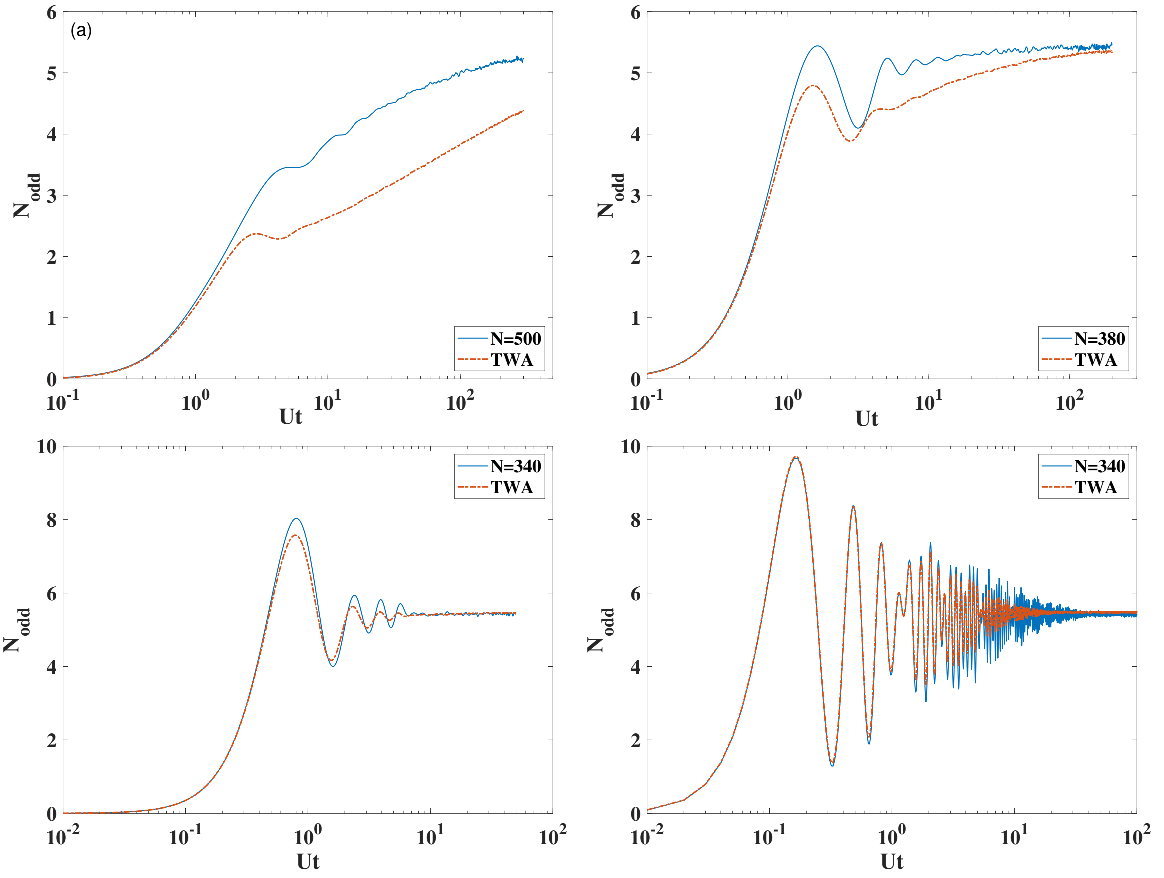

Fig. 5.5 Comparison between quantum dynamics and classical dynamics. System parameters used here are same with the ones in Fig. 5.3: (a) $J/U = 0.25$ with $Ut \in [0,300]$, (b) $J/U = 0.5$ with $Ut \in [0,300]$, (c) $J/U = 1.0$ with $Ut \in [0,50]$ and (d) $J/U = 5.0$ with $Ut \in [0,100]$. The blue lines for different U/J are from Fig. 5.3 with the largest N. The red dashed lines are calculated by TWA method with 50000 trajectories employed to get stable results.

resulting in a larger average particle number $\tilde{N} = 20$. Accordingly, we adjust the range of particle numbers S for the GCS basis functions to be within the interval $[6,30]$. This modification ensures that our variational approach retains a high fidelity with the initial state. In Figure 5.6, we present a convergence study similar to the analysis in Fig. 5.3, but with the altered initial state. Interestingly, while the general convergence behavior in most cases resembles that observed for $\tilde{N} = 10$, a notable exception arises for the case of $J/U = 0.5$. In this scenario, achieving convergence proves more challenging than in the corresponding case with a lower average particle number. This indicates that the ratio $J/(U\tilde{N})$ might serve as a more appropriate parameter for understanding the dynamics of the system, as previously demonstrated in studies involving Josephson junctions in Chapter. 4. The dynamics observed in panel (a) of Figure 5.6 for $J = 0.25$ offers an illustrative example. These dynamics bear a close resemblance to the result in Fig. 5.4 for $J = 0.1$, significantly because the ratios $J/(U\tilde{N})$

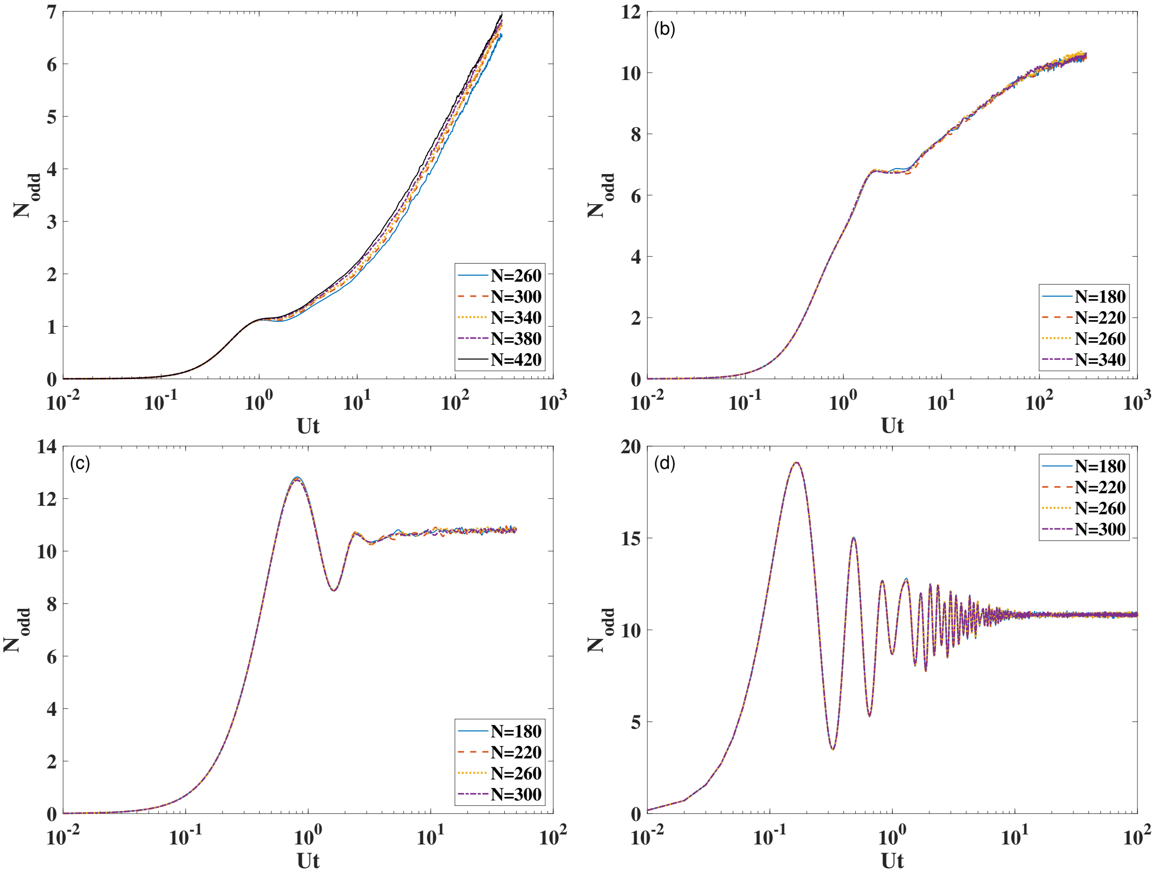

Fig. 5.6 Convergence of population dynamics of odd sites for varied J/U: (a) $J/U = 0.25$ with $Ut \in [0,300]$, (b) $J/U = 0.5$ with $Ut \in [0,300]$, (c) $J/U = 1.0$ with $Ut \in [0,50]$ and (d) $J/U = 5.0$ with $Ut \in [0,100]$.

in both cases are quite close. This similarity underscores the importance of considering the combined effects of interaction strength and average particle number when examining the dynamics.

In Figure 5.7, we repeat the comparative analysis between quantum dynamics and classical dynamics for the case of larger particle numbers. The main conclusion stays the same as the one derived from Fig. (5.5), but the onset of the discrepancy between quantum and classical results is earlier in terms of the values of U/J. For example, a clear deviation can be observed in panel (b) of Fig. 5.7, while classical dynamics stays more close to quantum dynamics with smaller $\tilde{N}$ in panel (b) of Fig. 5.5. This comparison proves again that taking into account the average particle number $\tilde{N}$, can offer a more comprehensive view of how different factors influence the approach to thermalization in the BH model.

The underlying reason for this discrepancy observed in Fig. (5.5) and Fig. (5.7) is definitely attributed to the quantum effects which classical dynamics lacks. Intuitively, when time is

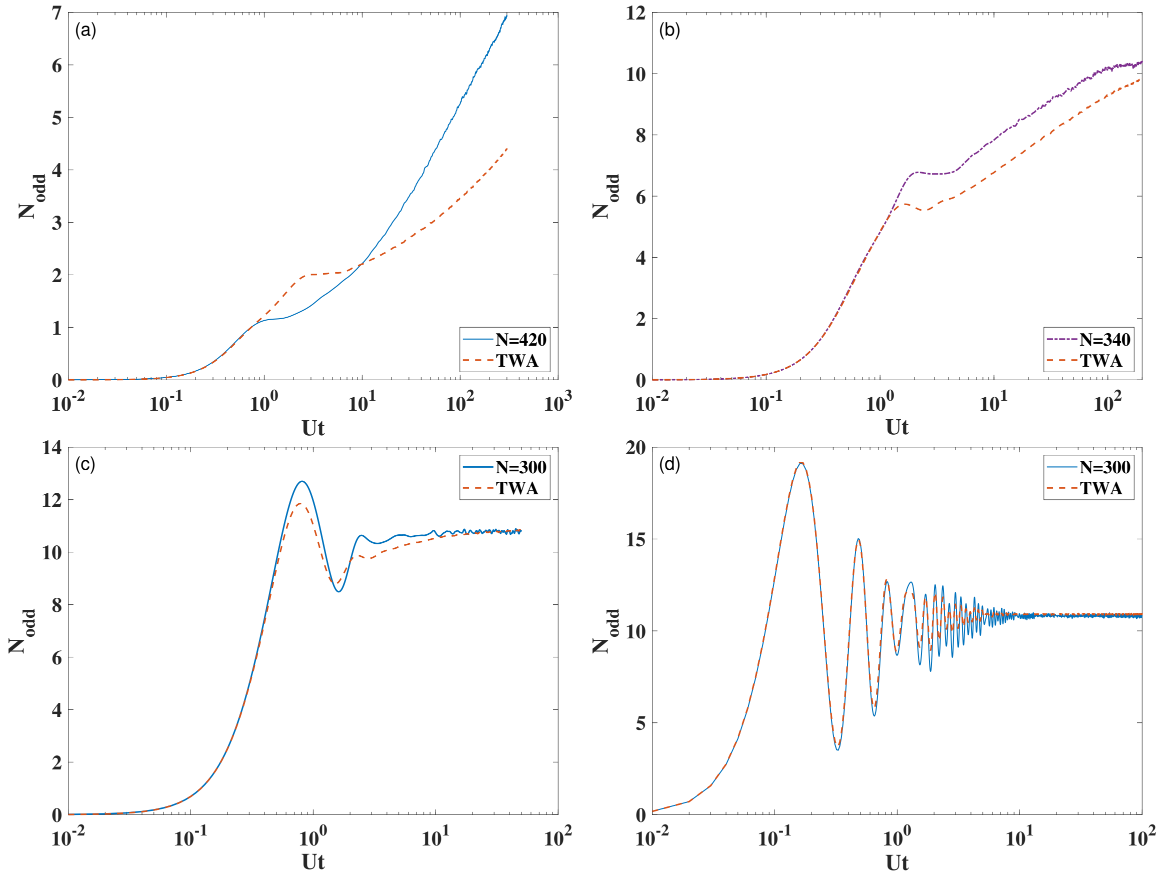

Fig. 5.7 Comparison between quantum dynamics and classical dynamics. System parameters are same with the ones in Fig. 5.3 except = 20. The red dashed lines are calculated by the TWA method using 50000 trajectories.

small, strong interactions will 'freeze' the diffusion of particles by hindering their distribution across the sites no matter in quantum or classical dynamics. Furthermore, by replacing ψ_i (equivalent to the α_i in this section) with $\sqrt{\tilde{N}}\xi_i$ in the classical equation Eq. (4.32)

$$i\dot{\xi}_i = -J(\xi_{i+1} + \xi_{i-1}) + U\tilde{N}|\xi_i|^2\xi_i \tag{5.23}$$

where ξ_i represents the normalized particle density, it is clear that the constraint induced by the nonlinear interaction can be increased by the average particle number $\tilde{N}$. However, as the system continues to evolve, quantum tunneling which is absent in classical dynamics will come into effect and will enhance the spreading of particles. We highlight that the quantum effect is captured by the nontrivial coupling of different basis functions in the variational approach, while in the TWA method, each trajectory evolves independently and classically. In contrast, the constraints on the particle movement in cases of weak interaction are less pronounced leading to a free spreading of particles in both quantum and classical models. As a result, the two approaches exhibit similar dynamics and rates of approaching equilibrium. It is important to note that the above analysis only provides a possible interpretation of the dependency of the thermalization process on interaction strength. Delving into the finer details of this process, especially how to distinguish the roles of quantum tunneling and quantum interference in the quantum enhancement would require a more in-depth study beyond the scope of numerical simulations. Nonetheless, these observations offer valuable insights into the distinct behaviors of quantum and classical systems.

Chapter 6

Entanglement in boson sampling

In the previous chapter, we have demonstrated the significance of GCS in the time-dependent dynamics of the BH model. In fact, the GCS-based approach can also be employed in other systems that preserve the U(1) symmetry, such as linear systems with up to quadratic Hamiltonians. Notably, the problems related to the linear optical network have gained considerable attention both in theoretical studies and experiments, a representative example is the boson sampling (BS) problem [151, 152]. While the structure of the linear optical network might appear more straightforward due to the absence of nonlinear interactions, estimating its output state remains a challenging task. In this chapter, we will illustrate the application of GCS in such linear systems, with a primary emphasis on analyzing the entanglement of the output state.

Entanglement, as first formulated by Schrödinger in 1935 [153], is one of the most striking properties of quantum systems, and it is also at the heart of quantum information, quantum computation, and quantum cryptography [154]. Entanglement is a fundamental resource for performing tasks such as teleportation, key distribution, quantum search, and many others; therefore, the calculation of entanglement and related measures [155] in lattice Hamiltonian has gained considerable interest [156–160]. Buonsante and Vezzani, e.g., have performed entanglement studies to investigate quantum phase transitions in the BH model [156]. In [161], it has been pointed out that even for non-interacting particles, bosonic entanglement creation outmatches the fermionic case due to the larger Hilbert space in the former case [162]. Moreover, understanding the build-up of entanglement, e.g., after a quench (a sudden change of the underlying Hamiltonian) is a central focus of the quantum many-body field [163], and an efficient simulation of quench dynamics on a classical computer would be a valuable resource [164]. A commonly used measure for estimating the entanglement is given by the Rényi entropy in a bipartite many-body setup [165].

However, the rapid growth of entanglement in many-body systems causes a severe problem to efficient numerical simulations. In lattice systems relevant for solid-state physics, e.g., matrix product state (MPS) based calculations are mainly favorable for area law scaling of the entanglement growth [11], which usually conflicts with a typical non-equilibrium dynamics. Similar problems are also encountered in linear systems, although without involving interaction between particles, and a well known example is the BS problem. Although the output state of BS does not follow an area law [159], in [157], the usage of MPS has been advocated for BS (as well as for a fermionic circuit). Therein, results for moderate particle and small mode numbers have been presented. The efficiency of these numerical calculations relies on the restriction to a small bond dimension, which, however, is not favorable for the rapid growth of entanglement.

The motivation of discussing the BS problem in the framework of the GCS is natural. The linear optical network is a straightforward setup for the GCS. It is expected that if the input state is a single GCS, the output state obtained through a unitary transformation will remain in the form of a GCS since the transformation preserves the symmetry as shown in the following sections. Furthermore, by means of the so-called Kan's formula [166] which will be discussed in detail below, the Fock state, which is the input of standard BS can be represented by a linear combination of GCS, which shares the same structure as our Ansätz used in Chapter. 4. This favorable representation indicates that the relationship between the input and the output can be established by applying a straightforward transformation to each GCS. The combination of theses advantages indicates that GCS will serve as a powerful basis for the BS problem.

6.1 Introduction to Boson sampling

A quantum computer, which benefits from quantum resources such as entanglement, can present some unique advantages when addressing certain problems which are intractable for classical computers. However, quantum systems are generally not isolated and are vulnerable to external noise. This environmental influence can cause quantum systems to deteriorate into classical systems which results in computational errors. Although numerous strategies have been proposed to mitigate these errors [167–172], the construction of a practical and universal quantum computer is still a significant challenge in the foreseeable future. On the other hand, some non-universal quantum computers have been designed to demonstrate the quantum supremacy in some specific problems. Most importantly, these specialized quantum machines typically require less complex architecture than their universal counterparts, which might make them more achievable in near-term experiments.

BS as a non-universal quantum computational model has been proposed to prove the ad-

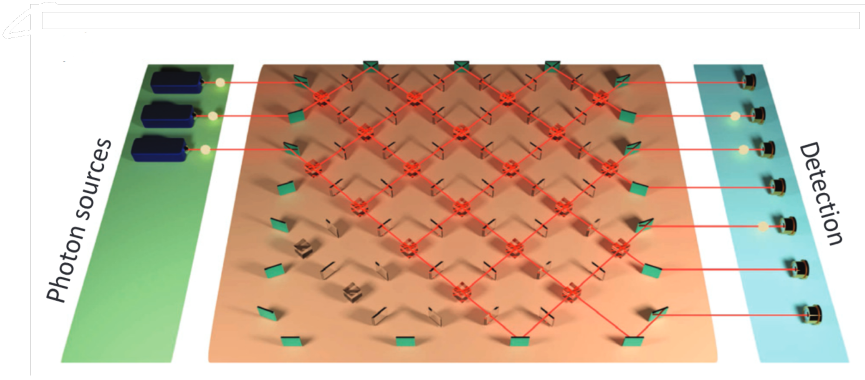

Fig. 6.1 The setup of BS, where three single photons are input into a linear optical network with 7 modes. This figure is originally from [176]. On the left side are single photon sources, the middle part consists of a linear optical network and the right side is a set of detectors.

vantage over classical computers, as BS is related to the calculation of the permanent of matrices, which has no efficient classical algorithm [173]. The standard framework of BS comprises three essential components. Firstly, a group of single-photon sources is used to produce a product state serving as the input. For instance, the input state could be denoted as $|11...100...\rangle$ where the first several modes are filled with single photons, and the remainder are unoccupied. However, creating a perfect single-photon source still remains a challenging task in experiment, hence Gaussian BS which employs a Gaussian state as its input has been extensively investigated as an alternative [174].

The second component is a liner optical network which is composed of beam splitters and phase shifters. Theoretically this network is characterized by a Haar random unitary matrix (HRU). This matrix is based on a uniform distribution and has no special structure apart from being unitary. The dimension of the matrix M, equal to the number of modes, is required to be much larger than the number of particles S on the order of $M > S^2$, such that the so-called collision free subspace (CFS) condition is satisfied, in which the particles will not collide with each other [151, 175]. Quantum interference will come into play when identical particles pass through this network, and such interference will give rise to a complicated output state which is a linear combination of all possible Fock states with fixed particle number S. The final component of the BS setup is the output port, where M detectors are used to measure the photon distribution over M modes. Under the CFS condition, every mode is ideally occupied by a single particle. Therefore, simple bucket detectors can be employed to verify particle arrival, eliminating the need to count the particle number. The schematic of BS is displayed in Fig. (6.1) taken from [176].

6.2 Boson Sampling as a unitary evolution

The quantity of interest in theoretical studies of BS is the probability P for a given configuration C of S photons distributed over M detectors in the CFS case, where $M \gg S$ and every mode is maximally singly occupied. This probability is related to the permanent of a submatrix of a (Haar random) unitary matrix with entries U_{ij} [177]. To see this, we briefly review the BS formalism by looking at the full state vector expressed in the Fock state basis $\{|\mathbf{m}\rangle\}$. It is given by [152],

$$|\Psi\rangle = \hat{R}(\mathbf{U^T})|\mathbf{n}\rangle = \sum_{\mathrm{C}} \gamma_{\mathrm{C}}|\mathbf{m}\rangle, \tag{6.1}$$

where the evolution of the initial state $|\mathbf{n}\rangle = |n_1, n_2, \dots, n_M\rangle$ is expanded in terms of the set $\{|\mathbf{m}\rangle = |m_1, m_2, \dots, m_M\rangle\}$. Now in the CFS case

$$\gamma_{\mathrm{C}} = \langle \mathbf{m}|\hat{R}(\mathbf{U^T})|\mathbf{n}\rangle = \mathrm{per}(U_{\mathbf{nm}}), \tag{6.2}$$

where $U_{\mathbf{nm}}$ is prepared by taking n_k copies of the k-th column and m_k copies of the k-th row of the full matrix $\mathbf{U}$. Thus, the probability, mentioned above, is identified as

$$P(\mathrm{C}) = |\gamma_{\mathrm{C}}|^2 = |\mathrm{per}(U_{\mathbf{nm}})|^2. \tag{6.3}$$

For the instance of three photons, initially in the Fock state $|1,1,1,0,0,\dots\rangle$ and finally in $|1,0,1,0,\dots,0,1\rangle$, the submatrix is constructed as follows:

$$U_{\mathbf{nm}} = \begin{pmatrix} U_{11} & U_{12} & U_{13} \\ U_{31} & U_{32} & U_{33} \\ U_{M1} & U_{M2} & U_{M3} \end{pmatrix}. \tag{6.4}$$

Furthermore,

$$\mathrm{per}(\mathbf{A}) = \sum_{\sigma \in S} \Pi_{k=1}^{S} A_{k\sigma_k}, \tag{6.5}$$

with σ the vector of permutations of (1,2,. . . .S), denotes the permanent of the matrix $\mathbf{A}$, which is defined analogously to the determinant but does not have the alternating sign in its definition and therefore is much harder to calculate because, generally, $\mathrm{per}(\mathbf{AB}) \neq \mathrm{per}(\mathbf{A})\mathrm{per}(\mathbf{B})$.

Permanent calculation is one of the prime examples of #*P*-hard problems in the field of computational complexity [173].

For an $n \times n$ matrix, the scaling of the numerical effort for its calculation via Ryser's formula [178] is of $\mathcal{O}(n^2 2^n)$, or $\mathcal{O}(n2^n)$ using Gray code [179], as compared to $\mathcal{O}(n^{2.373})$ for the determinant. We note that all these scalings are much better than that of Laplace expansion introduced in standard textbooks, which is $\mathcal{O}(nn!)$, but they are still exponentially expensive. The world record for numerical permanent calculation has just been pushed to matrices of sizes as small as 54x54 [180].

To make an analogy with unitary time evolution over one unit of time, we write the rotation operator appearing in Eq. (6.1) as

$$\hat{R}(\mathbf{U^T}) = \exp(-\mathrm{i}\hat{H}) \tag{6.6}$$

with the help of the beam splitting Hamiltonian

$$\hat{H} = \hat{\boldsymbol{a}}^{\dagger\mathrm{T}}\boldsymbol{\Phi}\hat{\boldsymbol{a}}, \qquad \boldsymbol{\Phi} = \mathrm{i}\ln \mathbf{U}^T, \tag{6.7}$$

where $\hat{\boldsymbol{a}}$ ($\hat{\boldsymbol{a}}^\dagger$) denotes the column vector of annihilation (creation) operators on the M modes and $\boldsymbol{\Phi}$, in general, is a full $M \times M$ Hermitian matrix with entries Φ_{ij} [181]. The action of the rotation operator on the elements of the vector of creation operators is then given by

$$\begin{aligned}
\hat{R}(\mathbf{U^T})\hat{a}_i^\dagger \hat{R}(\mathbf{U^T})^\dagger &= \sum_{m=0}^{\infty} \frac{1}{m!}\left[-\mathrm{i}\hat{H}, \hat{a}_i^\dagger\right]_m \\
&= \sum_{m=0}^{\infty} \frac{1}{m!}\left[-\mathrm{i}\sum_{kj}\Phi_{kj}\hat{a}_k^\dagger \hat{a}_j, \hat{a}_i^\dagger\right]_m \\
&= \sum_{m=0}^{\infty} \frac{1}{m!}(-\mathrm{i})^m \hat{\boldsymbol{a}}^{\dagger T}\boldsymbol{\Phi}_i^m \\
&= \hat{\boldsymbol{a}}^{\dagger T}\exp(-\mathrm{i}\boldsymbol{\Phi})_i \\
&= \sum_j U_{ij}\hat{a}_j^\dagger,
\end{aligned} \tag{6.8}$$

where we have used the Baker-Haussdorff (or Hadamard) lemma [182] and $\boldsymbol{\Phi}_i^m$ denotes the i-th column of the m-th power of $\boldsymbol{\Phi}$. To generate the numerical results presented in Sec.6.4, we used the Matlab code for the creation of Haar random unitary (HRU) matrices provided by Cubitt [183].

6.3 Application of the GCS bases

In the previous chapters, we have discussed the applications of the GCS defined by Eq. (2.1) for the non-equilibrium dynamics of many-body systems. For linear systems without interactions, using GCS as the initial state leads to a straightforward solution of the dynamical problem by the rotation operator, Eq. (6.8), which can be shown as follows [184]

$$\begin{aligned}
|\psi\rangle_{\text{out}} &= \hat{R}(\mathbf{U^T})|S,\vec{\xi}\rangle \\
&= \hat{R}(\mathbf{U^T})1/\sqrt{S!}\left(\sum_{i=1}^{M}\xi_i\hat{a}_i^\dagger\right)^S \hat{R}(\mathbf{U^T})^\dagger|0,0,\ldots\rangle \\
&= \sqrt{S!}\left(\sum_{i=1}^{M}\xi_i\sum_{j=1}^{M}U_{ij}\hat{a}_j^\dagger\right)^S|00\cdots 0\rangle \\
&= |S,\sum_{i=1}^{M}\xi_i U_{i1},\sum_{i=1}^{M}\xi_i U_{i2},\cdots,\sum_{i=1}^{M}\xi_i U_{iM}\rangle
\end{aligned} \tag{6.9}$$

where in the second line we have introduced $\hat{R}(\mathbf{U^T}^\dagger)$, using the fact that

$$\hat{R}(\mathbf{U^T})^\dagger|0,0,\ldots\rangle = \exp(i\hat{H})|0,0,\ldots\rangle = |0,0,\ldots\rangle, \tag{6.10}$$

because the annihilation operator acting on the vacuum state produces zero. From the above derivation, it is clear that the output state after the transformation is still a GCS just with updated parameters. This outcome suggests that if the input can be represented in terms of the GCS, the GCS form of the output state will be maintained. This task will be accomplished in the next section.

6.3.1 Exact representation of the initial state: Kan summation formula

In the following, we take a direct approach to the unitary evolution in the BS problem without invoking the variational principle [184]. In Chapter. 4, the time-evolved state is written in terms of the GCS as

$$|\Psi(t)\rangle = \sum_{k=1}^{N} A_k(t)|S,\vec{\xi}_k(t)\rangle, \tag{6.11}$$

where $\vec{\xi}_k = (\xi_{k1},\xi_{k2},\ldots,\xi_{kM})$ denotes a time-dependent vector of complex-valued GCS parameters and with multiplicity index k ranging from 1 to N. In this general form of the wavefunction, both the expansion coefficients $\{A_k\}$ as well as the GCS parameters are in principle time-dependent and complex valued. We can, however, refrain from the explicit time-dependence of the coefficients, if the exact expansion of the initial state in terms of GCS is used, as will be shown below. Applying the HRU of boson sampling from Eq. (6.6) amounts to evolution over the complete unit time interval ($t = 1$), but below, we will also consider finite time evolution, which is characterized by an exponent of the unitary operator $\exp(-\mathrm{i}\hat{H}t)$, where $t \in [0,1]$. This will allow us to study the build-up of entanglement, similar to the case of dynamics after a quench [185].

For the applicability of the proposed approach, it is decisive that the initial Fock state can be represented in terms of GCS since the product state is chosen as the input of the BS. This puzzle can be solved exactly analytically by the use of Kan's formula for monomials (a single product of powers) [166]

$$x_1^{s_1} x_2^{s_2} \cdots x_n^{s_n} = \frac{1}{S!} \sum_{\nu_1=0}^{s_1} \cdots \sum_{\nu_n=0}^{s_n} (-1)^{\sum_{i=1}^{n} \nu_i} \binom{s_1}{\nu_1} \cdots \binom{s_n}{\nu_n} \Big(\sum_{i=1}^{n} h_i x_i \Big)^S, \tag{6.12}$$

where $S = s_1 + s_2 + ... s_n$, with integers $s_i \geq 0$ and $h_i = s_i/2 - \nu_i$. The simplest case of this formula is elucidated by the equation

$$x_1 x_2 = \frac{1}{4}(x_1 + x_2)^2 - \frac{1}{4}(x_1 - x_2)^2,$$

where we only consider two formal variables x_1 and x_2, and both s_1 and s_2 are set to be 1. We observe that the term $\left(\sum_{i=1}^{n} h_i x_i \right)^S$ on the right hand side of Eq. (6.12) has a structure appearing also in the definition of the GCS given in Eq. (2.1). By replacing the formal variables x_i by creation operators $\hat{a}_i^\dagger$, we are thus able to build the (exact) relationship between Fock states and GCS according to

$$\begin{aligned}
|s_1, s_2, \cdots, s_M\rangle &= \frac{1}{\sqrt{s_1! s_2! \cdots s_M!}} (\hat{a}_1^\dagger)^{s_1} (\hat{a}_2^\dagger)^{s_2} \cdots (\hat{a}_M^\dagger)^{s_M} |00\cdots 0\rangle \\
&= \frac{1}{\sqrt{s_1! s_2! \cdots s_M!}\sqrt{S!}} \sum_{\nu_1=0}^{s_1} \cdots \sum_{\nu_M=0}^{s_M} (-1)^{\sum_{i=1}^{M} \nu_i} \\
&\binom{s_1}{\nu_1} \cdots \binom{s_M}{\nu_M} \Big(\sum_{i=1}^{M} |h_i|^2 \Big)^{S/2} \frac{1}{\sqrt{S!}} \Big(\sum_{i=1}^{M} \xi_i \hat{a}_i^\dagger \Big)^S |00\cdots 0\rangle \\
&= \frac{1}{\sqrt{s_1! s_2! \cdots s_M!}} \sum_{k=1}^{(s_1+1)(s_2+1)\cdots(s_M+1)} A_k |S, \vec{\xi}_k\rangle.
\end{aligned} \tag{6.13}$$

The initial coefficients and parameters of the GCS thus are

$$A_k = (-1)^{\sum_{i=1}^{M} v_{ki}} \binom{s_1}{v_{k1}} \cdots \binom{s_M}{v_{kM}} \frac{\left(\sum_{i=1}^{M} |h_{ki}|^2\right)^{S/2}}{\sqrt{S!}}, \tag{6.14}$$

$$\vec{\xi}_k = \frac{1}{\sqrt{\sum_{i=1}^{M} |h_{ki}|^2}} (h_{k1}, h_{k2}, \cdots, h_{kM}), \tag{6.15}$$

where $\{h_{ki}\} = \{\frac{s_i}{2} - v_{ki}\}$ and the set of $\{v_{k1}, v_{k2}, \cdots, v_{kM}\}$ represents the k-th possible combination of $v_1 = \{0, 1, \cdots, s_1\}, v_2 = \{0, 1, \cdots, s_2\}, \cdots, v_M = \{0, 1, \cdots, s_M\}$. The factor $\left(\sum_{i=1}^{M} |h_{ki}|^2\right)^{S/2}$ has been introduced in the definition of the coefficients in order to normalize the GCS parameter vectors.

For the special case $s_1 = s_2 = \cdots = s_S = 1$, we have $(S \leq M, N = 2^{S-1})$

$$|11 \cdots 100 \cdots 0\rangle = \sum_{k=1}^{N} A_k |S, \vec{\xi}_k\rangle \tag{6.16}$$

where

$$A_k = (-1)^{\sum_{i=1}^{S} v_{ki}} \binom{1}{v_{k1}} \cdots \binom{1}{v_{kS}} \frac{\left(\sum_{i=1}^{S} |h_{ki}|^2\right)^{S/2}}{\sqrt{S!}}, \tag{6.17}$$

$$\{h_{ki}\} = \left\{\frac{1}{2} - v_{ki}\right\}, \tag{6.18}$$

$$v_1 = \{0\}, v_2 = \{0, 1\}, \cdots, v_S = \{0, 1\}, \tag{6.19}$$

$$\xi_{k,S+1} = \cdots = \xi_{k,M} = 0. \tag{6.20}$$

Here, we note that there is a redundancy in Kan's original formula (6.12), already noticed by Kan himself. This results in the fact that we can reduce the multiplicity sum from $N = 2^S$ to $N = 2^{S-1}$ terms by fixing the first index v_1 to be zero. In passing, we note that the Kan formula underlying the present procedure thus involves an exponential scaling in the particle number of the required number of GCS basis functions. The numerical overhead in terms of mode number scales polynomially for a given number of particles, and thus we can handle a larger number of modes efficiently. Overall, this is in clear contrast to the typically much more demanding factorial scaling, according to $(M+S-1)!/[S!(M-1)!]$, of the number of basis functions that would be required in a Fock space calculation.

6.3.2 Unitary evolution

With the boson sampling setup in mind, we now assume that the input state is the Fock state $|11\cdots100\cdots0\rangle$, which we just discussed, and that the linear optical circuit is described by the rotation operator $\hat{R}$ from Eq. (6.6). Using Eqs. (6.8,6.9) and (6.13), the output state (at $t=1$) can then be written as

$$\begin{aligned}
|\Psi\rangle_{\text{out}} &= \hat{R}|11\cdots100\cdots0\rangle \\
&= \sum_{k=1}^{N}\frac{A_k}{\sqrt{S!}}\hat{R}\left(\sum_{i=1}^{M}\xi_{ki}\hat{a}_i^\dagger\right)^S \hat{R}^{-1}\hat{R}|00\cdots0\rangle \\
&= \sum_{k=1}^{N}\frac{A_k}{\sqrt{S!}}\left(\sum_{i=1}^{M}\xi_{ki}\sum_{j=1}^{M}U_{ij}\hat{a}_j^\dagger\right)^S|00\cdots0\rangle \\
&= \sum_{k=1}^{N}A_k|S,\sum_{i=1}^{M}\xi_{ki}U_{i1},\sum_{i=1}^{M}\xi_{ki}U_{i2},\cdots,\sum_{i=1}^{M}\xi_{ki}U_{iM}\rangle \\
&= \sum_{k=1}^{N}A_k|S,\vec{\xi}_k\rangle_{\text{out}}.
\end{aligned} \tag{6.21}$$

In contrast to an expansion in terms of Fock states, the GCS expansion coefficients (amplitudes) stay constant at all times and the GCS parameters $\{(\xi_{ki})_{\text{out}}\}$ characterizing the output state can be obtained by the matrix product

$$\begin{pmatrix}\vec{\xi}_1\\ \vec{\xi}_2\\ \vdots\\ \vec{\xi}_N\end{pmatrix}_{\text{out}} = \begin{pmatrix}\vec{\xi}_1\\ \vec{\xi}_2\\ \vdots\\ \vec{\xi}_N\end{pmatrix}_{\text{in}} \begin{pmatrix}U_{11} & U_{12} & \cdots & U_{1M}\\ U_{21} & U_{22} & \cdots & U_{2M}\\ \vdots & \vdots & \vdots & \vdots\\ U_{M1} & U_{M2} & \cdots & U_{MM}\end{pmatrix}. \tag{6.22}$$

In Appendix D, we show that the above output state allows for a rederivation of Glynn's formula for the permanent [186], given by

$$\begin{aligned}
\text{per}(\mathbf{U}) &= \langle 11\cdots1|\Psi\rangle_{\text{out}} \\
&= \frac{1}{2^{M-1}}\sum_{k=1}^{2^{M-1}}\left[\left(\prod_{i=1}^{M}x_{ki}\right)\prod_{m=1}^{M}\vec{x}_k\cdot\vec{U}_m\right],
\end{aligned} \tag{6.23}$$

where $M = S$ and $\vec{U}_m$ is the m-th column vector of the matrix $\mathbf{U}$. The vector $\vec{x}_k$ is defined in Appendix D.

6.4 The entanglement entropy

In the following, we investigate the creation of entanglement by application of the unitary operation of boson sampling [184]. The initial Fock state of the unpartitioned system is not entangled because it can be written as a single product of single particle states. A single GCS, in general, however, does not have this property, as can be inferred from its definition (2.1) as well as the discussion in Sec.2.4. Due to the important property of a single GCS being the ground state of the free-boson model, its entanglement properties have been studied in great depth by Dell'Anna, using the reduced density matrix [160].

6.4.1 Bipartitioning and Rényi entropies

In contrast to the single GCS case, we now consider the multi-configuration case, with the state $|\Psi\rangle$ being the superposition of multiple GCS, according to Eq. (6.11). Partitioning the system into a left and a right part, the (final) density operator of the full system is

$$\begin{aligned}\hat{\rho} &= \sum_{k,j=1}^{N} A_k A_j^* |S,\vec{\xi}_k\rangle\langle S,\vec{\xi}_j| \\ &= \frac{1}{S!}\sum_{n',n=0}^{S}\sum_{k,j=1}^{N} A_k A_j^* \binom{S}{n}\binom{S}{n'}\sqrt{n!(S-n)!n'!(S-n')!} \\ &\quad |S-n,\vec{\xi}_{k\tilde{L}}\rangle\langle S-n',\vec{\xi}_{j\tilde{L}}| \otimes |n,\vec{\xi}_{k\tilde{R}}\rangle\langle n',\vec{\xi}_{j\tilde{R}}| \qquad (6.24)\end{aligned}$$

where the sum in the definition of the GCS, Eq. (2.1), was split in two parts (L and R), a binomial expansion was used, and where the two unnormalized GCS are defined by

$$|S-n,\vec{\xi}_{\tilde{L}}\rangle = \frac{1}{\sqrt{(S-n)!}}\left(\sum_{i=1}^{M_L}\xi_i\hat{a}_i^\dagger\right)^{S-n}|00\cdots0\rangle, \qquad (6.25)$$

$$|n,\vec{\xi}_{\tilde{R}}\rangle = \frac{1}{\sqrt{n!}}\left(\sum_{i=M_L+1}^{M}\xi_i\hat{a}_i^\dagger\right)^{n}|00\cdots0\rangle. \qquad (6.26)$$

The fact that these GCS are not normalized is indicated by the tilde over the symbols L as well as R.

The reduced density matrix of the left subsystem can then be derived by tracing over the right one. Using the fact that GCS with different particle numbers are orthogonal to each other, this yields

$$\begin{aligned}\hat{\rho}_L &= \mathrm{Tr}_R(\hat{\rho}) \\ &= \sum_{n=0}^{S}\binom{S}{n}\sum_{k,j=1}^{N} A_k A_j^* \langle n, \vec{\xi}_{j\tilde{R}} | n, \vec{\xi}_{k\tilde{R}}\rangle |S-n, \vec{\xi}_{k\tilde{L}}\rangle\langle S-n, \vec{\xi}_{j\tilde{L}}|. \end{aligned} \tag{6.27}$$

Going into Fock space, the density matrix corresponding to the above density operator, analogous to Eq. (5) in [160], can thus be written in block diagonal form

$$\boldsymbol{\rho}_L = \mathrm{diag}(\boldsymbol{\rho}_L^{(0)}, \boldsymbol{\rho}_L^{(1)}, \cdots, \boldsymbol{\rho}_L^{(S)}), \tag{6.28}$$

where the uncoupled blocks $\boldsymbol{\rho}_L^{(n)}$ describe a distribution of n particles on the right side and $S-n$ particles on the left side of the cut. The elements of the blocks are given by

$$\boldsymbol{\rho}_L^{(n)} = \binom{S}{n}\sum_{k,j=1}^{N} C_{jk}^{(n)} \vec{W}_k^{(n)} \vec{W}_j^{(n)\dagger}. \tag{6.29}$$

with the coefficient

$$C_{jk}^{(n)} = A_k A_j^* \langle n, \vec{\xi}_{j\tilde{R}} | n, \vec{\xi}_{k\tilde{R}}\rangle \tag{6.30}$$

and where the vector $\vec{W}_k^{(n)}$ is filled by the entries $\langle n_1 n_2 \cdots n_{M_L} | S-n, \vec{\xi}_{k\tilde{L}}\rangle$ with $\sum_{i=1}^{M_L} n_i = S-n$. The product of the column vector with the row vector is a matrix but in the reverse order (row times column) it is the scalar

$$\vec{W}_j^{(n)\dagger} \cdot \vec{W}_k^{(n)} = \langle S-n, \vec{\xi}_{j\tilde{L}} | S-n, \vec{\xi}_{k\tilde{L}}\rangle = \left(\sum_{i=1}^{M_L} \xi_{ji}^* \xi_{ki}\right)^{S-n}, \tag{6.31}$$

where, for the overlap between GCS, a formula from the appendix of [104] has been used. Due to ease of computation, as a measure of the entanglement of the left subsystem after the application of the unitary matrix of boson sampling, the linear entropy $S_L = 1 - \mathrm{Tr}(\boldsymbol{\rho}_L^2)$ [177] as well as the second order Rényi entropy (see below) are frequently used. For computational purposes, to be explained more explicitely below, for the purity, it is favorable to use the expression

$$
\begin{aligned}
\mathrm{Tr}(\boldsymbol{\rho}_L^2) &= \sum_{n=0}^{S} \binom{S}{n}^2 \mathrm{Tr}\Big(\sum_{k,j=1}^{N} C_{jk}^{(n)} \vec{W}_k^{(n)} \vec{W}_j^{(n)\dagger} \sum_{k',j'=1}^{N} C_{j'k'}^{(n)} \vec{W}_{k'}^{(n)} \vec{W}_{j'}^{(n)\dagger} \Big) \\
&= \sum_{n=0}^{S} \binom{S}{n}^2 \sum_{k,j,k',j'=1}^{N} C_{jk}^{(n)} C_{j'k'}^{(n)} \mathrm{Tr}\Big(\vec{W}_k^{(n)} \vec{W}_j^{(n)\dagger} \vec{W}_{k'}^{(n)} \vec{W}_{j'}^{(n)\dagger} \Big) \\
&= \sum_{n=0}^{S} \binom{S}{n}^2 \sum_{k,j,k',j'=1}^{N} C_{jk}^{(n)} C_{j'k'}^{(n)} \left[\vec{W}_j^{(n)\dagger} \vec{W}_{k'}^{(n)} \right] \left[\vec{W}_{j'}^{(n)\dagger} \vec{W}_k^{(n)} \right] \\
&= \sum_{n=0}^{S} \binom{S}{n}^2 \sum_{k,j,k',j'=1}^{N} C_{jk}^{(n)} C_{j'k'}^{(n)} \left[\left(\sum_{i=1}^{M_L} \xi_{ji}^* \xi_{k'i} \right) \left(\sum_{i=1}^{M_L} \xi_{j'i}^* \xi_{ki} \right) \right]^{S-n} , \qquad (6.32)
\end{aligned}
$$

where we have used that the trace of the product of two operators amounts to a scalar product (step from line two to line three). This result can be specified to the case of the boson sampling problem by expressing the GCS parameters after the application of the HRU in terms of the Hermitian matrices

$$
\Lambda_L = (\vec{\mathscr{U}}_1, \vec{\mathscr{U}}_2, \cdots, \vec{\mathscr{U}}_{M_L}) \cdot (\vec{\mathscr{U}}_1, \vec{\mathscr{U}}_2, \cdots, \vec{\mathscr{U}}_{M_L})^\dagger \qquad (6.33)
$$

$$
\Lambda_R = (\vec{\mathscr{U}}_{M_L+1}, \vec{\mathscr{U}}_{M_L+2}, \cdots, \vec{\mathscr{U}}_M) \cdot (\vec{\mathscr{U}}_{M_L+1}, \vec{\mathscr{U}}_{M_L+2}, \cdots, \vec{\mathscr{U}}_M)^\dagger \qquad (6.34)
$$

derived in Appendix E and where $\vec{\mathscr{U}}_i$ is the truncated vector $\vec{U}_i$ with only the first S entries. There also the purity is reexpressed as

$$
\begin{aligned}
\mathrm{Tr}(\boldsymbol{\rho}_L^2) = \left(\frac{1}{2}\right)^{4(S-1)} \sum_{n=0}^{S} \frac{1}{[(S-n)!n!]^2} \\
\sum_{k,j,k',j'=1}^{2^{S-1}} \prod_{i=1}^{S} (x_{ki} x_{ji} x_{k'i} x_{j'i}) (\vec{x}_{k'} \Lambda_L \vec{x}_j^T \vec{x}_k \Lambda_L \vec{x}_{j'}^T)^{S-n} (\vec{x}_k \Lambda_R \vec{x}_j^T \vec{x}_{k'} \Lambda_R \vec{x}_{j'}^T)^n . \qquad (6.35)
\end{aligned}
$$

This formula allows us to write the purity in terms of particle as well as mode number and the entries of the unitary matrix $\boldsymbol{U}$ only, not making reference to GCS any longer.
The previous form of the purity, given in Eq. (6.32), with the output GCS parameters $\{\vec{\xi}_k\}$ from Eq. (6.22), however, is better suited for numerical purposes, as it can be calculated easily in matrix language. Also, there is no need to calculate the eigenvalues of the reduced density matrix for typically huge Fock space dimensions, which would be necessary to

calculate the von Neumann entropy

$$S_{\mathrm{vN}} = -\mathrm{Tr}(\boldsymbol{\rho}_L \ln \boldsymbol{\rho}_L) = -\sum_{n=0}^{S} \mathrm{Tr}(\boldsymbol{\rho}_L^{(n)} \ln \boldsymbol{\rho}_L^{(n)}). \tag{6.36}$$

In the focus of the results section below thus are the so-called Rényi entropies

$$S_\alpha = \frac{1}{1-\alpha} \ln \mathrm{Tr}(\boldsymbol{\rho}_L^\alpha). \tag{6.37}$$

For $\alpha = 2$ the purity just discussed is needed for its calculation. In the general case, higher powers of the density matrix have to be considered, however. This can be done along lines, similar to those of Eq. (6.32). The quadruple sum over the multiplicity indices would, e.g., turn into a sextupel sum for $\alpha = 3$. We stress that the number of terms in every sum can be reduced to 2^{S-1} by using the non-redundant Kan formula mentioned above. A relation between the Rényi entropy and the von Neuman entropy that we will refer to below is $S_{\mathrm{vN}} = \lim_{\alpha\to 1} S_\alpha$, and it is well-known that $S_1 \geq S_2 \geq S_3 \ldots$ [187]; see also [188] for a recent discussion of Rényi entropy inequalities in the context of Gaussian boson sampling. For the one-dimensional XY spin chain some useful exact results for Rényi entropies as a function of α are available [189]. Rényi entropies for noninteger values $0 < \alpha < 1$ are discussed in [190]. An experimental approach to measuring Rényi entropies employs the preparation of two copies of the same system and measuring the expectation value of the so-called swap operator. It has originally been devised to investigate quench dynamics in Bose-Hubbard type lattice Hamiltonians by Daley et al. [191].

6.4.2 Numerical results for the case $t = 1$

We first focus on the case $t = 1$ of time evolution with the full unitary matrix. All the entropies are calculated by averaging over different realizations of the HRU matrix, analogous to the analytic work by Page [192]. Individual realizations (not shown) do not differ much from the plots to be shown below, however. Firstly, in Fig. 6.2, the Rényi entropy for index $\alpha = 2$ as a function of subsystem size, corresponding to the locus of the bipartition, is depicted for different photon numbers, ranging between 8 and 12 (single realization calculations for 14 photons (not shown) are also possible within a few hours on a standard workstation). The total number of modes in all cases is 200, and the displayed Page curves are all symmetric around bipartition mode number 100, in contrast to the asymmetric curves in [157]. For a subsystem size smaller than S, the entropy follows a volume law (see also the discussion in

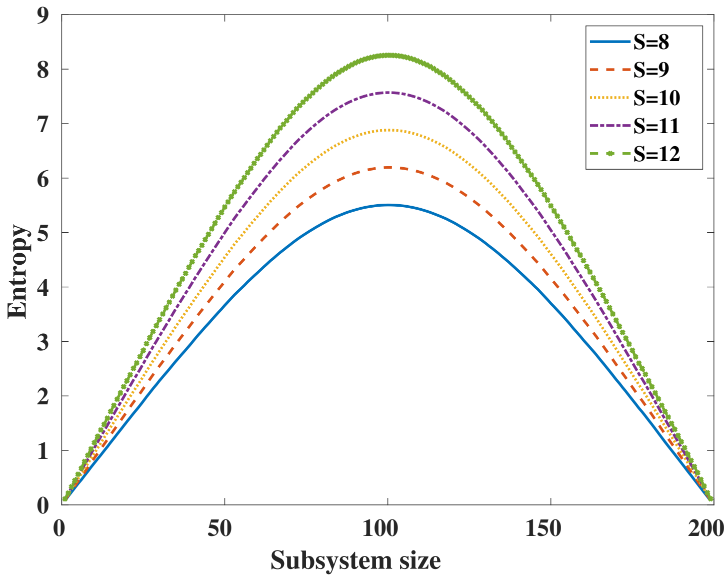

Fig. 6.2 Rényi entropy (averaged over 100 realizations of the HRU) with index $\alpha = 2$ as a function of the size of the left system for different photon numbers, ranging from $S = 8$ to $S = 12$, in the case of a fixed number of modes ($M = 200$).

the following subsection), and the maximum entropy [1] is displayed for splitting the system into two equal halves. The scaling of this maximum entropy with particle number is linear, as shown in Fig. 6.3. We stress that the Rényi entropy is a lower bound for the von Neumann entropy, and our exact results can be taken as a benchmark for other, purely numerical calculations. Furthermore, we note that we can observe asymmetric curves for the entropy if we consider exponents $t < 1$, as will be discussed in the following subsection.

Secondly, the Rényi entropy for different index α as a function of subsystem size in a system with $S = 10$ and $M = 500$ is depicted in Fig. 6.4. Again, for subsystem size smaller than S, a volume law is found with the slope depending on the Rényi index. Changing the number of photons does not qualitatively alter the results. They show that by increasing α, the entropy is monotonically decreasing (in complete agreement with classical results from symbolic dynamics [187]), and the functional form turns from concave to (almost) convex (the second order derivative (assuming the abscissa to be a continuous variable) of the blue curve in Fig. 6.4 is negative, whereas the second derivative of the green curve is almost everywhere positive).

Interestingly, the maximum of the entropy (at $M = 250$) for $S = 10$ is only slightly dependent on the Rényi index but we stress that the deviations of the maximum are not finite size effects, as shown in Fig. 6.3, for different index the maximum entropy will increase linearly with the

---

[1] Defined as the maximal value of the entanglement entropy as a function of subsystem size (after averaging)

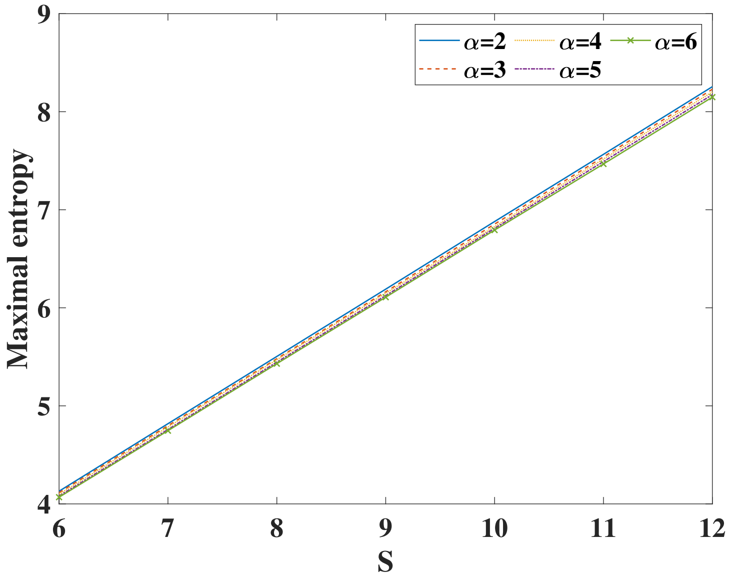

Fig. 6.3 The maximal Rényi entropy (averaged over 100 realizations of the HRU) as a function of particle numbers for different α with fixed $M = 200$.

particle number (with an decreasing slope for increasing α) , when the mode number is very large. Particularly, the slope of the line for $\alpha = 2$ is $\ln 2$. The fundamental physics behind this is that, when the system is cut in the middle and particles are input through the first S modes, the output state can be presented as

$$\begin{aligned}|\Psi\rangle_{\text{out}} &= \left[\prod_{i=1}^{S}(\vec{U}_i^L \hat{\boldsymbol{a}}_L^\dagger + \vec{U}_i^R \hat{\boldsymbol{a}}_R^\dagger)\right]|00\cdots 0\rangle \\ &= \sum_{l=1}^{2^S} |\vec{\psi}_L\rangle_l |\vec{\psi}_R\rangle_l \end{aligned} \tag{6.38}$$

where $\vec{U}_i^L$ is the vector consisting of the first $M/2$ elements of $\vec{U}_i$, and $\hat{\boldsymbol{a}}_L^\dagger$ is the vector of creation operators for the first $M/2$ modes. Moreover, the index l in the second line denotes the possible configuration of the output state in Fock space. A concrete form of $|\vec{\psi}_L\rangle_l$ is presented as follows

$$|\vec{\psi}_L\rangle_l = \prod_{i \in G_l} \vec{U}_i^L \hat{\boldsymbol{a}}_L^\dagger |0\rangle \tag{6.39}$$

where G_l is a group of some possible integer numbers from 1 to S. The factorial form of $|\vec{\psi}_L\rangle_l$ results from the assumption that

$$[\vec{U}_i^L \hat{\boldsymbol{a}}_L^\dagger, \vec{U}_j^L \hat{\boldsymbol{a}}_L^\dagger] = \delta_{ij}. \tag{6.40}$$

This commutation relation is valid under the CFS condition as different input particles will not occupy the same modes in the output ports.
As the Haar random matrix is uniformly distributed, we have

$$|\vec{U}_i^L|^2 \approx |\vec{U}_i^R|^2 \approx \frac{1}{2} \tag{6.41}$$

which holds for every i. This means each particle can appear in the left partition or the right partition equally. The corresponding reduced matrix of Eq. (6.38) after tracing out the right part $|\vec{\psi}_R\rangle_l$ is a diagonal matrix filled with the same element $1/2^S$, which gives the largest 2nd order Rényi entropy,

$$S \ln 2.$$

The derivation for the maximal entropy of the output state can be found in [193]. The fact that we can calculate Rényi entropies for many different values of α would allow us also to study entanglement spectra [194].
Finally, we studied the maximum Rényi entropy (at equal partition) as a function of the total mode number in Fig. 6.5. All the curves shown are almost saturating as increasing M, so the maximum entropy tends to stay constant from a certain size. We checked the case of $M > 1000$ and still found a slight increase, though. This finding corroborates the assumption that in order to fully reach the so-called CFS limit, it might be necessary that $M \geq S^5 \log^2 S$ [175]. Thus, in essence, the finding of this last numerical result is that, under CFS conditions, the maximum entropy that the application of the unitary can yield is achieved. We also stress that the initial quick increase of the maximum entropy, which we observe for small mode numbers and which is also seen in a similar setup [195] is broken for higher mode numbers. The scaling of the maximum entropy with respect to particle number can be extracted from Fig. 6.2. This scaling is linear, corroborating the finding displayed in the last entry of Table I in [196], but in contrast to the observation of a logarithmic scaling in [159] for a nonlinear optical network. It is also worthwhile to note that although there is still an increase in entanglement for large mode numbers (at fixed particle number), the numerical effort to produce the results is not growing exponentially with M since the number of basis functions is not changing.

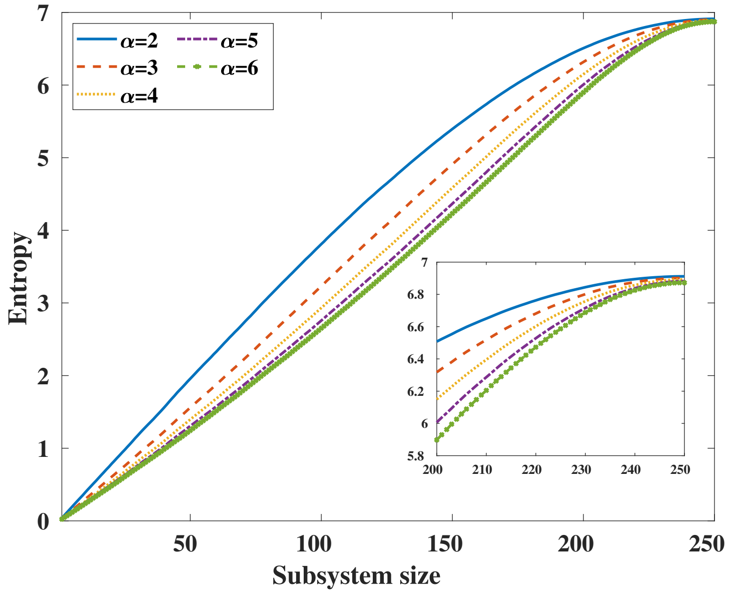

Fig. 6.4 Rényi entropy (averaged over 100 realizations of the HRU) as a function of bipartition mode number for different α for fixed $S = 10$ and $M = 500$. Only the left side of the symmetric curve is depicted. The inset shows more clearly that the curves do not converge to the exact same maximum.

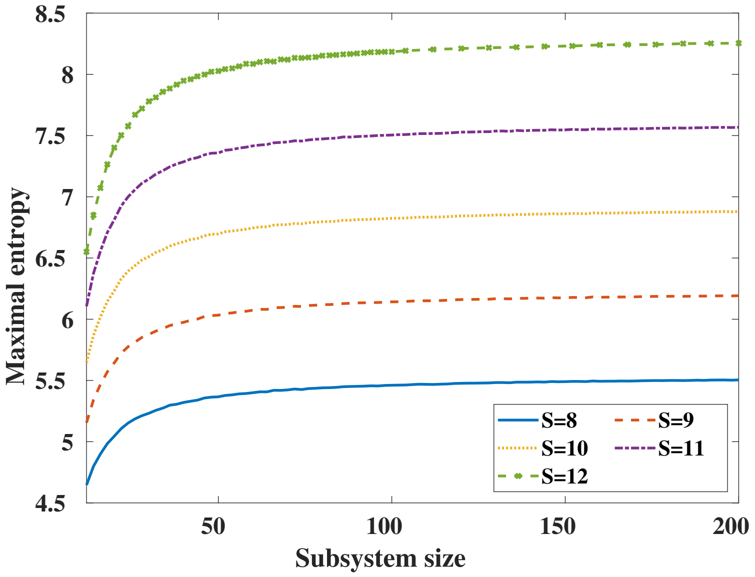

Fig. 6.5 Maximum Rényi entropy ($\alpha = 2$) averaged over 500 realizations of the HRU as a function of mode number for different particle numbers S.

6.4.3 Build-up of entanglement

In this last section, we mimic the build-up of entanglement by choosing the power of the unitary matrix (which in the previous section was given by $t = 1$) to be somewhere inside the interval $t \in [0,1]$. The parameter t then plays a similar role as does time in a study of the dynamics of a many-body system after a quench (sudden change of the Hamiltonian) [185]. In panels (a) and (b) of Fig. 6.6, where we took different roots of the HRU, it is revealed that for small values of t, the diagonal elements of the resulting matrix (a single matrix is displayed, we did not take an average) are still dominant, whereas for t closer to unity, the structure along the diagonal gets washed out. For the case $t = 0.8$, displayed in panel (b), it is barely visible any longer, as the matrix elements tend to be fully random. The result of applying the evolution matrix to the initial state, according to Eq. (6.22), is represented in panels (c) and (d) of the same figure. Increasing t leads to a transfer of population to mode numbers that are further and further away from the initially occupied ones. Thus at $t = 0.8$ a more even distribution of the population over all modes is observed.

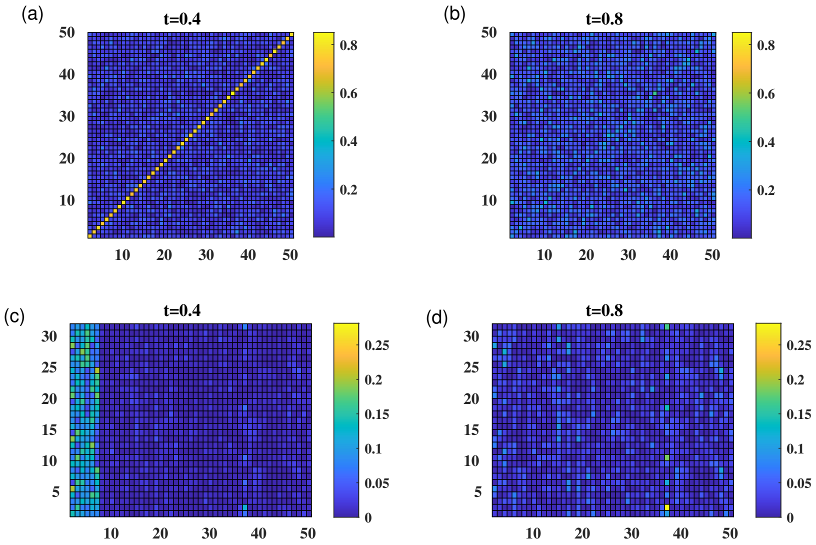

Fig. 6.6 Panels (a) and (b): absolute values of the elements of different powers t of the HRU matrix with $M = 50$; panels (c) and (d): absolute value squared of the GCS parameters ξ_{ki} as a function of mode number (x-axis running from 1 to M) and multiplicity index (y-axis for $S = 6$ running to $N = 2^{6-1} = 32$).

The corresponding results for the entanglement shown in Fig. 6.7 are similar to the ones in [193] as they show a linear increase with particle number of the maximum entropy in the asymptotic regime. However, our results do not show an almost linear increase with time [197, 185] before the asymptotic regime is reached. This may be because a local coupling is

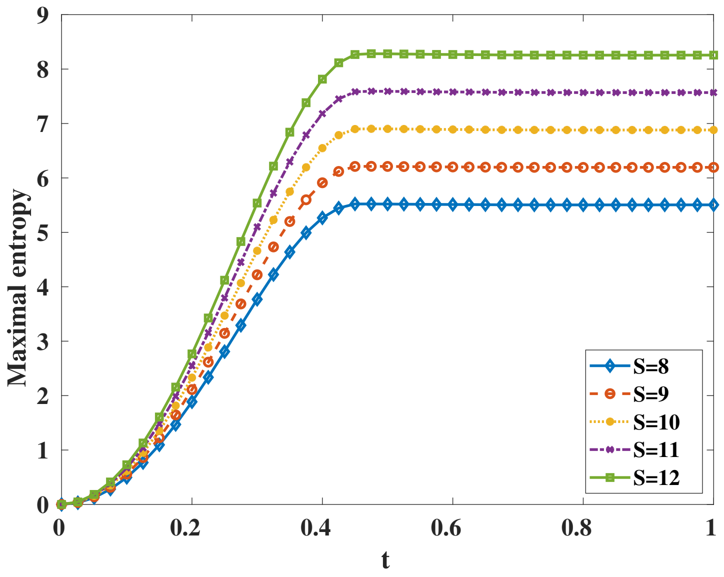

Fig. 6.7 Maximum Rényi entropy ($\alpha = 2$) as a function of t (time) averaged over 100 realizations of the unitary for different particle numbers S and fixed mode number $M = 200$.

employed to generate the results in [185]. In contrast, in our case, for all $t < 1$, the coupling is still fully nonlocal (taking the logarithm of the unitary matrices). In our results, a quadratic increase is followed by a linear one, and the maximum entropy is reached already at $t = 0.45$ regardless of the particle number. Thus, although the population has not been distributed evenly across the system (see Fig. 6.6), the entropy has already reached its maximum.
Another important observation is that if we rescale the maximal entropy with $1/S$, these different curves will converge into a single one displayed in Fig. 6.8,and the maximal value achieved is $\ln 2$, which we have already extracted from Fig. 6.3. This indicates that there exists an universality, independent of the particle numbers in the entanglement dynamics.
Finally, in Fig. 6.9 we show the full entropy curve as a function of subsystem size for different values of t for $S = 10$. The graphs display an asymmetric shape with a cusp-like structure at bipartition mode number equal to the particle number $S = 10$, due to the choice of the asymmetric initial state. The cusp gets smoothened out and the curves become more and more symmetric for larger values of t. At $t = 1$ there is no "memory" of the unsymmetric initial state left. For bipartition mode numbers smaller than ten, we always find a linear increase of the entropy, corresponding to a volume law, as already mentioned in the discussion of Fig. 6.2. As also mentioned earlier, the maximum entropy is reached already at $t = 0.45$. It is, however, not located at symmetric bipartition if the exponent is not equal to unity. For $t \ll 1$, the correlation between the left (initially populated) and the right (initially unpopulated) part is not fully developed; thus, the entanglement will decrease for bipartition mode numbers

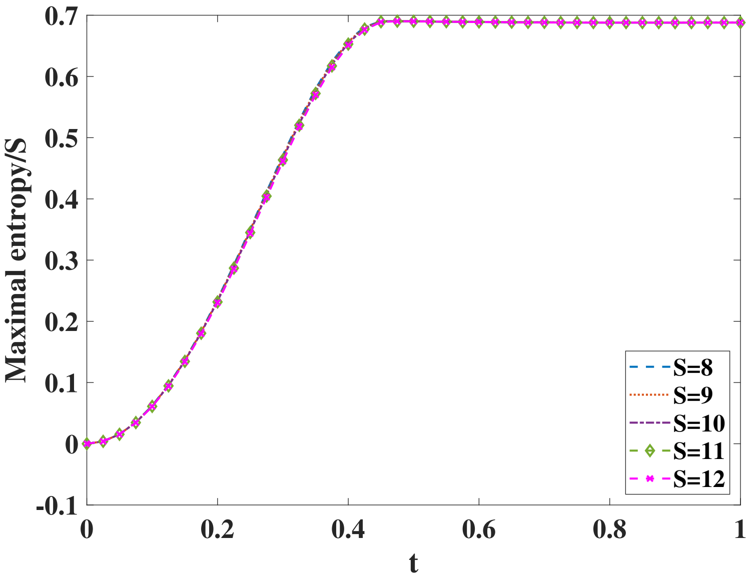

Fig. 6.8 The rescaled maximal Rényi entropy ($\alpha = 2$) as a function of t (time). The entropy is divided by corresponding particle numbers S for each curve in Fig. 6.7.

above 10. For $t \to 0$, as expected, the entropy will shrink to an overall constant value of zero without a cusp.

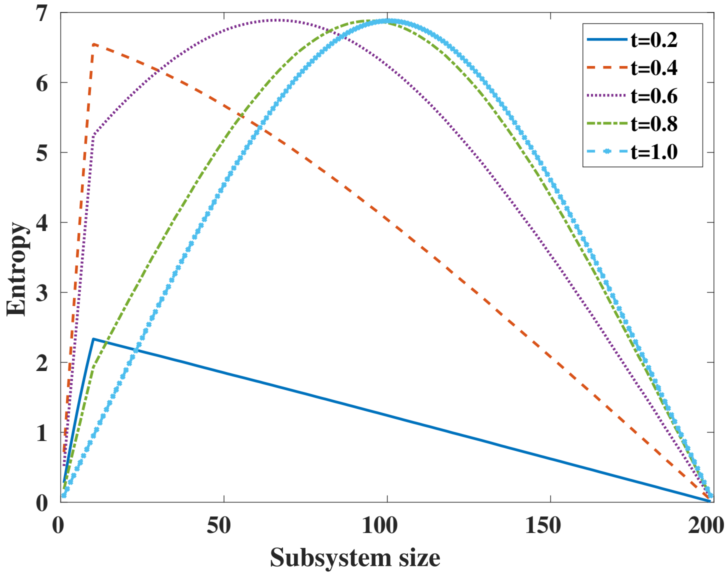

Fig. 6.9 Rényi entropy ($\alpha = 2$) averaged over 100 realizations of the HRU as a function of mode number for different depths and fixed particle number $S = 10$.

6.4.4 Linear optical network with layers

In experimental setups and also theoretical studies [157, 193], the linear optical network is constructed in layers, and each layer consists of beam splitters, which only act on the adjacent modes, and the on-site phase shifters. A typical schematic is displayed in Fig. 6.10. In theory, each beam splitter is characterized by a 2×2 Haar random matrix. Compared to the global Haar random matrix we discussed above, this local matrices will give rise to a different behavior of the entanglement dynamics, because intuitively, the local operation will slow down the spreading of the entanglement.

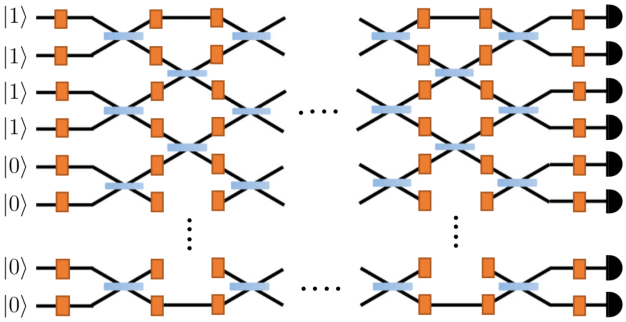

Fig. 6.10 Linear optical network with the layer structure. The orange bricks mean the on-site phase shifters and the crossings denote the beam splitters which couples the adjacent modes. This figure is taken from [193].

In Fig. 6.11, we show the dynamics of the maximal entropy as a function of network depth, and every depth contains two layers-one coupling the odd sites and the other the even sites. The input state we use is still $|11\cdots100\cdots0\rangle$. We can observe that the maximal entropy initially shows a logarithmic growth which is consistent with the result in [193], and for small particle numbers, using a maximal depth of 100 layers leads to the saturated results. Although the curves for large particle number still continue to increase for larger depth, the ultimate saturated values achieved are identical to those found in the cases with the global network.

In Fig. 6.12, we gradually increase the depth of the network, denoted by L, from 50 to 5000, and for each depth we compute the entanglement entropy as a function of the subsystem size. This figure can be compared to Fig. 6.9 where time rather than depth is used and the Haar random matrix is global. It is shown that when the depth is shallow, the distribution of the entropy is confined in the first several modes. Beyond this region, the entropy tends to diminish, while in Fig. 6.9 the entropy remains nonzero even the position of the bipartition is remote. When the depth is increased, the maximal entropy for each depth also increases until the saturated value is reached, and the distribution of the entropy becomes more broad and symmetric, which is similar with the results in Fig. 6.2. This suggests that we can use

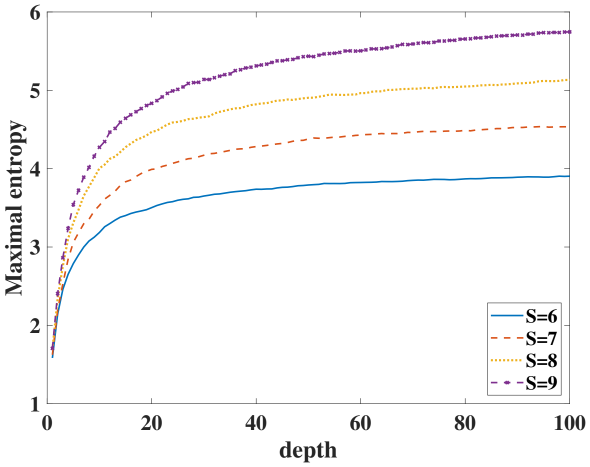

Fig. 6.11 The maximal 2nd Renyi entropy of a bipartition as a function of the depth defined in the main text. The curves for different particle numbers $S = 6, 7, 8, 9, 10$ with fixed number of modes $M = 100$ are drawn with different colors. The results are averaged over 100 realizations.

the optical network with local Haar random matrices to simulate standard BS, as long as the considered depth is large.

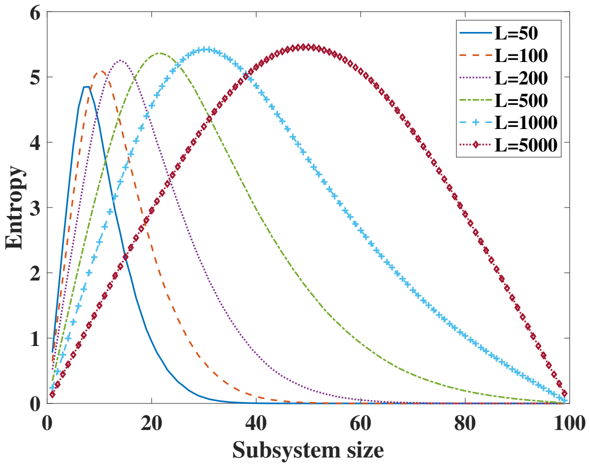

Fig. 6.12 The entropy as a function of the subsystem size for various the depth of the network. The particle number $S = 8$ and number of modes $M = 100$. The results are averaged over 100 realizations.

Chapter 7

Summary and Outlook

In this work, we have studied the application of GCS for the quantum dynamics of many-body systems. The results, in the main text from Chapter 2 to Chapter 6, are summarized as follows.

In Chapter 2, we have delved into the properties of GCS. The definition of GCS we have used in this thesis shows that GCS describe an ideal condensate where all particles occupy a single-particle state. This state can be created by applying a generator of the SU(M) group to an extreme state. Moreover, we have revealed that GCS are intimately related to the standard Glauber CS in several ways: 1) Glauber CS can be expanded in terms of GCS with different particle numbers; 2) annihilation operators have similar effects on these two states; 3) both states constitute overcomplete and non-orthogonal basis sets, whereas GCS are only overcomplete in the subspace with fixed particle number. Despite these similarities, the two sets of states also have some different properties, such as the conservation of particle numbers which GCS adhere to. Another noticeable difference being entanglement, where GCS is an entangled state, while a multi-mode Glauber CS is a product state.

In Chapter 3, we have studied the non-equilibrium dynamics of GCS and Glauber CS driven by nonlinear interaction. The nonlinear effect has been presented through a look at the dynamics of the Husimi function of the evolved Glauber CS. Our analytical derivations have confirmed that the two-point correlation functions of the evolved GCS are equivalent to those of the evolved Glauber CS in the thermodynamic limit, where the particle number and the number of the modes are infinite but their ratio is finite. However, their autocorrelation functions, which measure the amplitude of the survival probability, are not simply equivalent. We have demonstrated that these functions are related by a Fourier series of the overlap between the evolved Glauber CS and the initial state up to a phase. We have used this finding to explain the vanishing of the survival probability of the evolved GCS, which corresponds to kinks of the dynamical free energy density, calculable exactly by the generating function method. Furthermore, we have drawn the Husimi function of the evolved Glauber CS in phase space, where the survival probability is determined by the relative position between the Husimi function and a circle in phase space with a radius equal to the amplitude of the displacement of the CS. Specifically, when the distribution of the Husimi function is far from the circle, the survival probability will rapidly decrease to zero. However, if the value of the displacement is large, then the Husimi function tends to distribute over the circle, such that the full integral of the Fourier series should be calculated. We further demonstrated that the conclusion about the autocorrelation can be generalized to the case of a generic Hamiltonian.

In Chapter 4, we have investigated the dynamics of the Bose-Hubbard (BH) model, involving the nonlinear interaction and the tunneling term. To deal with this complex system, we have developed a basis function expansion consisting of a linear combination of a set of GCS. Both expansion coefficients and the characteristic parameters of the GCS have been treated as variables, and their equations of motion have been obtained from the TDVP. We have applied this basis function set to the nonequilibrium dynamics of the BH model. The usefulness of the variational approach was verified by gradually recovering quantum effects with increasing numbers of GCS basis functions.

In the first example in Chapter 4, we have discussed some dynamical properties of the bosonic Josephson junction, described by the two-mode BH model. In such a toy model, the classical phase space is characterized by the particle imbalance z, and the relative phase ϕ between two wells. For initial points in proximity to the classically stable fixed points, just a handful of basis functions suffice to reproduce the quantum beating effect. But for initial points distant from the stable points, the quantum beating effect is amplified accompanied by a substantial phase fluctuation, such that more basis functions are required to recover this fluctuation. For $\Lambda < -1$ defined in main text, quantum trajectories around the unstable fixed point exhibit chaotic behaviour when the particle number is small. However, large particle numbers can lead to the emergence of the regular dynamics similar with the classical ones. At last, by recalling the Husimi distribution again, we have provided a more precise criterion compared to the mean-field theory for the onset of the SSB with merely two basis functions.

Another example before entering into the real many-body realm is the three-site BH model. Herein, we have focused on the effect of the value of the interaction strength on the effectiveness of our basis function expansion. We have computed the dynamics of the population along with the condensate fraction with different values of interaction strength, and compared the results from the variational method to the exact ones. We found that larger interaction strength requires us to employ more basis functions to get satisfactory results.

In Chapter 5, we have developed a multi-layer GCS basis function to deal with the dynamics initialized by multimode Glauber CS. We have increased the system size up to 11 sites and studied the phenomenon of thermalization. The thermalization process has been investigated using both a quantum variational approach and the classical TWA method. Key findings include the significant influence of interaction strength (J/U) and average particle number ($\tilde{N}$) on the system's approach to thermal equilibrium. Quantum dynamics showed a faster approach to equilibrium in strong interaction regimes, likely due to quantum tunneling effects, in contrast to classical dynamics.

In Chapter 6, we have shifted our focus to the so-called Boson sampling problem whose setup is a linear optical network. Using Kan's formula to express a Fock initial state in terms of generalized coherent states, we have derived an exact analytical formula for the output state of a linear optical network for standard boson sampling. The scaling of the numerical effort to evaluate the sum is exponential in particle number S via 2^{S-1}, but only polynomial in the number of modes M. In total, the computational complexity thus increases much less severely than the super-exponential scaling of the size of the Fock state Hilbert space, which is of dimension $(M+S-1)!/[S!(M-1)!]$. The tractable dependence on the mode number of the numerical effort of sum evaluation has allowed us to investigate the so-called collision-free subspace case, for which it is believed that $M \approx S^2$ is sufficient. At the initial investigation stage, the output state wavefunction has been derived in terms of multiple GCS. Along the way, we have also rederived the formula of Glynn for the permanent of a square matrix.

Using the binomial theorem, the reduced density operator is calculated from the wavefunction. Employing this important intermediate result, the purity and traces of powers higher than two of the reduced density matrix are calculated exactly and are given in terms of multiple sums that could probably be simplified further. The results involve overlaps of GCS and do not need the evaluation of eigenvalues of matrices for huge Hilbert space dimensions. This allows us to study the creation of subsystem entanglement by applying the unitary matrix of boson sampling. In case of applying the full unitary matrix, i.e., for $t = 1$, we have corroborated numerically that the Rényi entropy is a decreasing function of the Rényi index and that the maximum Rényi entropy is realized at equipartition, regardless of the asymmetric population of the initial state. In addition, we have found that the maximum entropy is only slightly dependent on the index α. Furthermore, because of the polynomial dependence on M of our numerical complexity, we could corroborate that under collision-free subspace conditions, the maximum Rényi entropy saturates as a function of mode number. A cusp in the (generally asymmetric) entropy curve at partition mode number equal to particle number has been found by investigating the build-up of entanglement which follows a universal pattern after rescaling in terms of the particle number. As an important insight of the last subsection, it turns out that although the population has not yet fully equilibrated, the entropy already has reached its maximum value at $t \approx 0.45$.

In the final part of Chapter. 6, we have studied the local optical network with multiple layers, finding that the build-up of entanglement by increasing the depth of the local optical network is fundamentally different from that driven by a global Haar matrix. Meanwhile, the entropy as a function of subsystem size is asymmetric when the depth is small. These results highlight the differences with respect to the entanglement entropy between globally and locally connected linear systems.

In summary, we have studied various physical features of GCS, and developed a GCS-based variational basis function approach to explore the nonequilibrium dynamics of the BH model and the properties of the entanglement entropy in the Boson sampling problem.

In the future, we could apply our basis function to the dynamics of higher dimensional system which are formidable to solve due to the violation of area law of entanglement entropy [11]. By employing our basis function expansion, we could possibly capture the essence of non-equilibrium dynamics by recovering quantum effects gradually. This could lead to significant advancements in understanding the process of thermalization in more complex lattice structures.

Another promising direction is exploring quantum information scrambling in many-body systems by combining our methods for dynamics and entanglement entropy. Quantum information scrambling refers to the process by which information encoded in a local quantum state becomes distributed over global degrees of freedom, a phenomenon that is closely related to the growth of entanglement in these systems. Through our studies focusing on entanglement dynamics, we could gain insights into the mechanisms of scrambling, which are essential in fields like quantum computing and black hole thermodynamics in quantum gravity [198].

Appendix A

Some properties of generalized coherent states

In this appendix, we review some computationally helpful formulae along the lines of [31, 104], which are needed in the main text. Firstly, the commutation between the annihilation operator and the collective creation operator which is applied to generate an GCS is given by

$$[\hat{a}_i, \Big(\sum_{j=1}^{M} \xi_j \hat{a}_j^\dagger\Big)^S] = S\xi_i \Big(\sum_{j=1}^{M} \xi_j \hat{a}_j^\dagger\Big)^{S-1}. \tag{A.1}$$

Secondly, by defining two collective operators

$$\hat{A}^\dagger = \sum_{i=1}^{M} \xi_i \hat{a}_i^\dagger, \qquad \hat{B}^\dagger = \sum_{i=1}^{M} \eta_i \hat{a}_i^\dagger, \tag{A.2}$$

two different GCSs can be generated via

$$|\vec{\xi}\,\rangle = \frac{1}{\sqrt{S!}}(\hat{A}^\dagger)^S|0\rangle, \qquad |\vec{\eta}\,\rangle = \frac{1}{\sqrt{S!}}(\hat{B}^\dagger)^S|0\rangle. \tag{A.3}$$

The vectorized parameter contains the parameters of all modes (here we do not consider doubly indexed parameters). The inner product of the above two states is then given by

$$\begin{aligned}
\langle\vec{\eta}|\vec{\xi}\,\rangle &= \frac{1}{S!}\langle 0|\Big(\sum_{i=1}^{M}\eta_i^*\hat{a}_i\Big)^S\Big(\sum_{j=1}^{M}\xi_j\hat{a}_j^\dagger\Big)^S|0\rangle \\
&= \frac{1}{S!}\langle 0|\sum_{n_1+n_2+\cdots=S}\frac{S!}{n_1!n_2!\cdots}[(\eta_1^*\hat{a}_1)^{n_1}(\eta_2^*\hat{a}_2)^{n_2}\cdots]\rangle \\
&\sum_{m_1+m_2+\cdots=S}\frac{S!}{m_1!m_2!\cdots}[(\xi_1\hat{a}_1^\dagger)^{m_1}(\xi_2\hat{a}_2^\dagger)^{m_2}\cdots]|0\rangle \\
&= \frac{1}{S!}\Big(\sum_{n_1+n_2+\cdots=S}\frac{S!}{\sqrt{n_1!n_2!\cdots}}\eta_1^{*n_1}\eta_2^{*n_2}\cdots\langle\vec{n}|\Big) \\
&\sum_{m_1+m_2+\cdots=S}\frac{S!}{\sqrt{m_1!m_2!\cdots}}\xi_1^{m_1}\xi_2^{m_2}\cdots|\vec{m}\rangle \\
&= \sum_{m_1+m_2+\cdots=S}\frac{S!}{m_1!m_2!\cdots}(\eta_1^*\xi_1)^{m_1}(\eta_2^*\xi_2)^{m_2}\cdots \\
&= \Big(\sum_{i=1}^{M}\eta_i^*\xi_i\Big)^S,
\end{aligned} \tag{A.4}$$

where we have used the general binomial theorem

$$(x_1+x_2+\cdots+x_n)^k = \sum_{a_1+a_2+\cdots+a_n=k}\frac{k!}{a_1!a_2!\cdots a_n!}x_1^{a_1}x_2^{a_2}\cdots x_n^{a_n}. \tag{A.5}$$

The above result (A.4) is quite different from the corresponding property for Glauber coherent states, which involves exponential functions.

Using Eq. (A.1), we can now calculate the action of the annihilation operator on the GCS via

$$\begin{aligned}
\hat{a}_i|\vec{\xi}\,\rangle &= \hat{a}_i\frac{1}{\sqrt{S!}}\Big(\sum_{j=1}^{M}\xi_j\hat{a}_j^\dagger\Big)^S|0\rangle \\
&= \frac{1}{\sqrt{S!}}[\Big(\sum_{j=1}^{M}\xi_j\hat{a}_j^\dagger\Big)^S a_i + S\xi_i\Big(\sum_{j=1}^{M}\xi_j\hat{a}_j^\dagger\Big)^{S-1}]|0\rangle \\
&= \sqrt{S}\xi_i|\vec{\xi}'\rangle
\end{aligned} \tag{A.6}$$

where we have used the action of the annihilation operator on the Fock state, namely, $a_i|n_i\rangle = \sqrt{n_i}|n_i - 1\rangle$ as well as the definition

$$|\vec{\xi}'\rangle = \frac{1}{\sqrt{(S-1)!}}\Big(\sum_{j=1}^{M} \xi_j \hat{a}_j^\dagger\Big)^{S-1}|0\rangle \tag{A.7}$$

of the $(S-1)$-boson GCS.
Furthermore, for $|\eta\rangle$ and $|\xi\rangle$, from Eq. (A.6) we get

$$\langle\vec{\eta}|\hat{a}_j^\dagger \hat{a}_k|\vec{\xi}\rangle = S\eta_j^* \xi_k \langle\vec{\eta}'|\vec{\xi}'\rangle \tag{A.8}$$

where the inner product $\langle\vec{\eta}'|\vec{\xi}'\rangle$ is

$$\langle\vec{\eta}'|\vec{\xi}'\rangle = \Big(\sum_{i=1}^{M} \eta_i^* \xi_i\Big)^{S-1}. \tag{A.9}$$

In the main text as well as below, we will also refer to the following two inner products

$$\langle\vec{\eta}''|\vec{\xi}''\rangle = \Big(\sum_{i=1}^{M} \eta_i^* \xi_i\Big)^{S-2}, \tag{A.10}$$

$$\langle\vec{\eta}'''|\vec{\xi}'''\rangle = \Big(\sum_{i=1}^{M} \eta_i^* \xi_i\Big)^{S-3}, \tag{A.11}$$

of the $(S-2)$ and the $(S-3)$ GCS.

Using the chain rule, the matrix element of the right time-derivative now is

$$\begin{aligned}
\langle\vec{\eta}|\overrightarrow{\partial_t}|\vec{\xi}\,\rangle &= \langle\vec{\eta}|\sum_{i=1}^{M}\dot{\xi}_i\partial_{\xi_i}|\vec{\xi}\,\rangle \\
&= \frac{S}{\sqrt{S!}}\langle\vec{\eta}|\sum_{i=1}^{M}(\dot{\xi}_i\hat{a}_i^{\dagger})(\hat{A}^{\dagger})^{S-1}|0\rangle \\
&= \frac{S}{S!}\langle 0|\hat{B}^{S-1}\hat{B}\sum_{i=1}^{M}(\dot{\xi}_i\hat{a}_i^{\dagger})(\hat{A}^{\dagger})^{S-1}|0\rangle \\
&= \langle\vec{\eta}'|\sum_{i=1}^{M}(\dot{\xi}_i\hat{B}\hat{a}_i^{\dagger})|\vec{\xi}'\rangle \\
&= \langle\vec{\eta}'|\sum_{i=1}^{M}\dot{\xi}_i(\eta_i^{*}+\hat{a}_i^{\dagger}\hat{B})|\vec{\xi}'\rangle \\
&= \sum_{i=1}^{M}(\dot{\xi}_i\eta_i^{*})\langle\vec{\eta}'|\vec{\xi}'\rangle + \sum_{i,j=1}^{M}\dot{\xi}_i\eta_j^{*}\langle\vec{\eta}'|\hat{a}_i^{\dagger}\hat{a}_j|\vec{\xi}'\rangle \\
&= \sum_{i=1}^{M}(\dot{\xi}_i\eta_i^{*})\langle\vec{\eta}'|\vec{\xi}'\rangle + (S-1)\sum_{i,j=1}^{M}\dot{\xi}_i\eta_j^{*}\eta_i^{*}\xi_j\langle\vec{\eta}''|\vec{\xi}''\rangle \\
&= S\sum_{i=1}^{M}(\dot{\xi}_i\eta_i^{*})\langle\vec{\eta}'|\vec{\xi}'\rangle
\end{aligned} \tag{A.12}$$

In the fifth line of the above equation, we have used the result of Eq. (A.1) for $S=1$, and the relation $\sum_{j=1}^{M}\xi_j\eta_j^{*}\langle\vec{\eta}''|\vec{\xi}''\rangle = \langle\vec{\eta}'|\vec{\xi}'\rangle$ which follows from Eqs. (A.9,A.10) is also used to get the result of the last line.

Similarly, for the left time-derivative we find

$$\begin{aligned}
\langle\vec{\eta}|\overleftarrow{\partial_t}|\vec{\xi}\,\rangle &= \langle\vec{\eta}|\sum_{i=1}^{M}\dot{\eta}_i^{*}\partial_{\eta_i^{*}}|\vec{\xi}\rangle \\
&= \langle\vec{\eta}'|\sum_{i=1}^{M}(\dot{\eta}_i^{*}\hat{a}_i\hat{A}^{\dagger})|\vec{\xi}'\rangle \\
&= \sum_{i=1}^{M}(\dot{\eta}_i^{*}\xi_i)\langle\vec{\eta}'|\vec{\xi}'\rangle + (S-1)\sum_{i,j=1}^{M}(\dot{\eta}_i^{*}\xi_j\eta_j^{*}\xi_i)\langle\vec{\eta}''|\vec{\xi}''\rangle \\
&= S\sum_{i=1}^{M}(\dot{\eta}_i^{*}\xi_i)\langle\vec{\eta}'|\vec{\xi}'\rangle
\end{aligned} \tag{A.13}$$

Both results will be used in the main text.

Appendix B

Variational principles

In this appendix, we will review three variational principles and reveal their relations. Furthermore, we will demonstrate that satisfying the Cauchy-Riemann equations is a sufficient condition for these principles to be equivalent.
Let us initiate our discussion with the time-dependent Schrödinger equation, expressed as

$$\mathrm{i}\frac{\partial}{\partial t}|\Phi(t)\rangle = \hat{H}|\Phi(t)\rangle. \tag{B.1}$$

Despite its seemingly straightforward form, finding the exact solution for $|\Phi(t)\rangle$ proves to be a formidable challenge in the majority of scenarios. To facilitate this challenge, it is promising to construct an approximate trial function $|\Psi(x(t))\rangle$ which is close to the exact one

$$|\Psi(x(t))\rangle \approx |\Phi(t)\rangle \tag{B.2}$$

where $x \equiv x_i$ represents a set of time-dependent variables, which can be either real or complex. Particularly, if x_j is a complex number, we treat x_j and its complex conjugate x_j^* as independent variables, for example, the variable space can be like $x_j \in \{x_i\}$ with i ranging from 1 to N, while $x_j^* \in \{x_i\}$ with i ranging from $N+1$ to $2N$. A specific configuration of variables is given in Chapter. 4, where $|\Psi(x(t))\rangle$ is represented as a linear combination of GCS, with x comprising both coefficients and characteristic parameters as shown in Eq. (4.1). Since $|\Psi(x(t))\rangle$ is an approximation, the residual state vector

$$\left(\mathrm{i}\frac{\partial}{\partial t} - \hat{H}\right)|\Psi(x(t))\rangle$$

is nonzero quantifying the deviation from the exact solution. The remaining task is to find the differential equations of $\{x_j\}$ which minimize the error. To this end, several variational principles are introduced to address this issue.

Dirac-Frenkel variational principle

The first one we will discuss is the Dirac-Frenkel variational principle (DFVP) [25]. The core idea of DFVP is to render the residual state vector orthogonal to the variation of the basis function $|\Psi\rangle$. The required variation is defined by

$$|\delta\Psi\rangle = |\partial_{x_j}\Psi\rangle\delta x^j$$

where δx^j denotes the infinitesimal variation of $x_j(t)$ and the Einstein summation convention is used to sum over all indeces. Here we clarify that the ket $|\partial_{x_j}\Psi(x)\rangle$ denotes the derivative with respect to the variable x_j

$$|\partial_{x_j}\Psi\rangle = \frac{\partial|\Psi\rangle}{\partial x_j} \tag{B.3}$$

irrespective of whether x_j is real or complex. Correspondingly, the bra $\langle\partial_{x_j}\Psi|$ takes the form

$$\langle\partial_{x_j}\Psi| = \frac{\partial\langle\Psi|}{\partial x_j^*}, \tag{B.4}$$

with $x_j = x_j^*$ if x_j is real. Please always keep in mind that x_j and x_j^* are indexed differently within the variable set $\{x_j\}$.

The condition of orthogonality to the variation of the basis function translates to:

$$\left\langle \delta\Psi \middle| \left(\mathrm{i}\frac{\partial}{\partial t} - \hat{H}\right) \middle| \Psi \right\rangle = 0. \tag{B.5}$$

Given that different variations δx_j are independent, we derive a set of differential equations for $x_j(t)$ by substituting Eq. (B.4) into Eq. (B.5), leading to

$$\mathrm{i}\Omega_{jk}\dot{x}^k = \varepsilon_j, \tag{B.6}$$

where $\dot{x}^k$ denotes the time derivative of the variable x_k, and the chain rule is used

$$\frac{\partial|\Psi\rangle}{\partial t} = \frac{\partial|\Psi\rangle}{\partial x_j}\frac{\mathrm{d}x^j}{dt} \tag{B.7}$$

when the time derivative acts on the $|\Psi\rangle$. The Hermitian matrix Ω_{jk} in Eq. (B.6) is thus defined as

$$\Omega_{jk} = \langle \partial_{x_j}\Psi|\partial_{x_k}\Psi\rangle \tag{B.8}$$

and ε_j is given by

$$\varepsilon_j = \langle \partial_{x_j}\Psi|\hat{H}|\Psi\rangle. \tag{B.9}$$

Before leaving this section, we note that, in general, Eq. (B.6) is highly nonlinear.

McLachlan's variational principle

Following the introduction of DFVP, McLachlan's Variational Principle (MCVP) was proposed to minimize the norm of the residual state vector

$$||\mathrm{i}\partial_t|\Psi\rangle - \hat{H}|\Psi\rangle||^2 \tag{B.10}$$

throughout the entire evolution [26]. In order to attain the minimum, this expression needs to satisfy the stationary condition

$$\delta||\mathrm{i}\partial_t|\Psi\rangle - \hat{H}|\Psi\rangle||^2 = 0. \tag{B.11}$$

MCVP operates under the assumption that the state $|\Psi\rangle$ at time t is not varied, while $\Theta = \partial_t|\Psi\rangle$ is variable and subject to optimization, hence we only need to compute the variation of Θ in Eq. (B.11), leading to

$$-\mathrm{i}\langle\delta\Theta|(\mathrm{i}\partial_t - \hat{H})|\Psi\rangle + \mathrm{i}(\langle\mathrm{i}\partial_t\Psi| - \langle\Psi|\hat{H})|\delta\Theta\rangle = 0 \tag{B.12}$$

where the variation of Θ is given by

$$\delta\Theta = |\partial_{x_j}\Psi\rangle\delta\frac{\mathrm{d}x^j}{\mathrm{d}t}, \tag{B.13}$$

and is proportional to the variation of the trial function $|\Psi\rangle$

$$|\delta\Psi\rangle = |\partial_{x_j}\Psi\rangle\delta x^j$$

because the variation $\delta \frac{\mathrm{d}x^j}{\mathrm{d}t}$ is arbitrary. This leads us to the final form of MCVP

$$\mathrm{Im}\left[\langle\delta\Psi|(\mathrm{i}\partial_t - \hat{H})|\Psi\rangle\right] = 0. \tag{B.14}$$

Equation (B.14) reveals that MCVP imposes a less stringent condition compared to DFVP, as it only requires the imaginary part of the expression in DFVP to be zero.

We also note that Eq. (B.14) is identical with

$$\mathrm{Re}\left[\langle\delta\Psi|(\partial_t + \mathrm{i}\hat{H})|\Psi\rangle\right] = 0, \tag{B.15}$$

which is frequently encountered in the literature.

Time-dependent variational principle

The third variational principle is the time-dependent variational principle (TDVP) we have employed in the main text [27]. TDVP ensures the stationarity of the action expressed as

$$\delta S = 0, \qquad S = \int_{t_1}^{t_2} \mathrm{d}t L, \tag{B.16}$$

where the Lagrangian in quantum mechanics is given by

$$L = \langle\Psi|(\mathrm{i}\partial_t - \hat{H})|\Psi\rangle. \tag{B.17}$$

Substituting Eq. (B.17) into Eq. (B.16), we obtain

$$\begin{aligned}
\delta S &= \int_{t_1}^{t_2} \mathrm{d}t \left[\langle\delta\Psi|(\mathrm{i}\partial_t - \hat{H})|\Psi\rangle + \langle\Psi|(\mathrm{i}\partial_t - \hat{H})|\delta\Psi\rangle\right] \\
&= \int_{t_1}^{t_2} \mathrm{d}t \left[\langle\delta\Psi|(\mathrm{i}\partial_t - \hat{H})|\Psi\rangle + (\langle\mathrm{i}\partial_t\Psi| - \langle\Psi|\hat{H})|\delta\Psi\rangle\right] + \mathrm{i}\langle\Psi|\delta\Psi\rangle|_{t_1}^{t_2} \\
&= \int_{t_1}^{t_2} \mathrm{d}t \left[\langle\delta\Psi|(\mathrm{i}\partial_t - \hat{H})|\Psi\rangle + (\langle\mathrm{i}\partial_t\Psi| - \langle\Psi|\hat{H})|\delta\Psi\rangle\right]
\end{aligned} \tag{B.18}$$

where in the second line we have performed a partial integral to let the time derivative act on the bra, and we have assumed that the variation $|\delta\Psi\rangle$ is zero at the boundaries of the time interval $[t_1, t_2]$ as is shown in [199].

It is important to note that the final result in Eq. (B.18) is equivalent to the condition

$$\mathrm{Re}\left[\langle\delta\Psi|(\mathrm{i}\partial_t - \hat{H})|\Psi\rangle\right] = 0 \tag{B.19}$$

which must hold throughout the entire time interval. This condition can alternatively be expressed using the Euler-Lagrange equation displayed in Eq. (4.9). Eq. (B.19) shows that the TDVP is also a part of DFVP.

Equivalence of three variational principles

In [199], the notion of complementary parameters is introduced to establish a sufficient condition for the equivalence of different variational principles. This paper also elucidates how the concept of complementary parameters can be linked to the Cauchy-Riemann equations

$$\frac{\partial|\Psi\rangle}{\partial x_j^*}=0, \tag{B.20}$$

employed in our Chapter. 4, and where x_j are the first N variables in the variable space. Here we will utilize this equation to give a brief proof of the equivalence condition.

Eq. (B.20) indicates that all the variables must be complex numbers with nonzero imaginary parts, in the meantime the only non-zero derivative of $\langle\Psi|$ with respect to the variables is $\partial_{x_j^*}\langle\Psi|$. As a result, the variation of the $\langle\Psi|$ is expressed as

$$\langle\delta\Psi| = \langle\partial_{x_j}\Psi|\delta x^{j*} = \langle\partial_{x_j}\Psi|\left(\mathrm{Re}[\delta x^{j*}]+\mathrm{i}\mathrm{Im}[\delta x^{j*}]\right). \tag{B.21}$$

Inserting Eq. (B.21) into Eq. (B.14), we derive an equation for every x_j

$$\mathrm{Re}[\delta x_j^*]\cdot\mathrm{Im}\left[\langle\partial_{x_j}\Psi|(\mathrm{i}\partial_t-\hat{H})|\Psi\rangle\right]+\mathrm{Im}[\delta x_j^*]\cdot\mathrm{Re}\left[\langle\partial_{x_j}\Psi|(\mathrm{i}\partial_t-\hat{H})|\Psi\rangle\right]=0. \tag{B.22}$$

Given that $\mathrm{Re}[\delta x^{j*}]$ and $\mathrm{Im}[\delta x^{j*}]$ are independent variations, both terms on the LHS in Eq. (B.22) are enforced to be zero, namely,

$$\mathrm{Re}\left[\langle\partial_{x_j}\Psi|(\mathrm{i}\partial_t-\hat{H})|\Psi\rangle\right]=0, \tag{B.23}$$

$$\mathrm{Im}\left[\langle\partial_{x_j}\Psi|(\mathrm{i}\partial_t-\hat{H})|\Psi\rangle\right]=0. \tag{B.24}$$

The combination of Eq. (B.23) and Eq. (B.24) is identical to Eq. (B.6) derived from the DFVP. Analogous to the proof in the case of MCVP, it is straightforward to verify that if the Cauchy-Riemann equation is satisfied, Eq. (B.23) and Eq. (B.24) will also hold for the TDVP, in other words, TDVP agrees with the DFVP as well.

We argue that our above results only demonstrate that the Cauchy-Riemann equations is a sufficient condition for the equivalence of the three variational principles. A typical counterexample is the Glauber CS defined by Eq. (2.17). It is clear that the Glauber CS does not follow the Cauchy-Riemann equation as the α^* is involved in the normalization factor $\exp(-|\alpha|^2/2)$, whereas the previous study [200] shows that all the variational principles are equivalent also for this state. A more strict condition for the equivalence based on the concept of Kähler manifolds can be found in a recent paper [106].

Appendix C

Detailed convergence study with respect to grid spacing

To prove the advantage of small spacings of complex grids for getting converged results by following [136], for most of this appendix we choose the diagonal of the combination of the rectangular grids rather than the random choice of points from the rectangular grids which have been used in the main text. In diagonal grids, the parameters of the GCS lie in the exact same positions for every complex subgrid, for example,

$$\{\xi_{mn,1},\xi_{mn,2}\}=\left\{\frac{z_{mn,1}}{\sqrt{|z_{mn,1}|^2+|z_{mn,2}|^2}},\frac{z_{mn,2}}{\sqrt{|z_{mn,1}|^2+|z_{mn,2}|^2}}\right\}, \tag{C.1}$$

in the case of 2 modes, where m, n are the same(!) complex grid indices. We remind of the fact that in the random choice of the two-mode grid, a random combination of the points on the grid of the first mode with the points of the grid of the second mode is allowed! Although using diagonal grids is less optimal than the random ones (as will become obvious below), according to our numerical results, it can help us avoid the influence of randomness and compare the effects of different spacings directly at the same level. In the following, we will show some results for normalized population dynamics for different initial states with different photon and mode numbers.

For the two-mode case, we examine the results from a time-dependent Hamiltonian

$$\hat{H}=-J(t)(\hat{a}_1^\dagger\hat{a}_2+\hat{a}_2^\dagger\hat{a}_1)+\frac{U}{2}(\hat{a}_1^{\dagger 2}\hat{a}_1^2+\hat{a}_2^{\dagger 2}\hat{a}_2^2) \tag{C.2}$$

where $J(t)=J_0+J_1\cos(\omega t)$. The initial state is $|50,-\sqrt{0.7},\sqrt{0.3}\rangle$. The interaction strength is $U=0.1J_0$, and the driving frequency and strength are $\omega=2\pi/J_0$ and $J_1=0.5J_0$. We

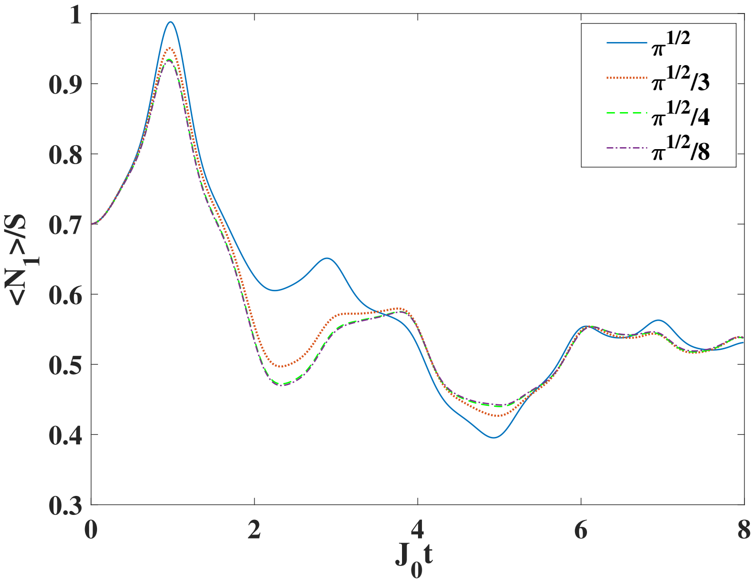

Fig. C.1 The dynamics of the population of the first mode in the two-mode case with 50 photons. The driving frequency and strength are $\omega = 2\pi/J_0$ and $J_1 = 0.5J_0$, and the on-site interaction energy $U = 0.1J$. The number of GCSs is 25. Different lines are results for different spacings of the complex grid. Solid: $\sqrt{\pi}$, dotted: $\sqrt{\pi}/3$, dash: $\sqrt{\pi}/4$, dash-dotted: $\sqrt{\pi}/8$.

constructed two identical complex 5×5 grids, and the number of GCS we used thus is just $N = 25$ (and not 625, as it would be if we would allow all combinations of the rectangular grid points). Fig. C.1 reveals that small spacings allow to arrive at the converged result more quickly. In the present case, $\sqrt{\pi}/4$ is enough to reproduce the exact result. For the second, more demanding initial state $|200, -\sqrt{0.7}, \sqrt{0.3}\rangle$ with 200 photons, the number of grid points is increased to 81. Fig. C.2 shows that the spacing with $\sqrt{\pi}/4$ does not yet work well and that for this initial condition $\sqrt{\pi}/8$ is a better choice.

Next we extend our results to the four-mode case with a constant in time hopping parameter $J = 1$. In Fig. C.3 results are shown for the initial state $|30, -\sqrt{0.7}, \sqrt{0.3}, 0, 0\rangle$. Although it has less photons than the in two-mode case above, the spacing$\sqrt{\pi}/4$ which performs well in Fig. C.1 does not give rise to converged results with 169 basis functions, and this kind of deviation for $\sqrt{\pi}/4$ also occurs for other states with larger numbers of photons or other initial state parameters (not shown). Thus the number of modes seems to be decisive, when choosing the optimal grid spacing.

In Fig. C.4, we present a study of the number of basis functions which is needed for getting converged results by optimizing the underlying grid spacing. This time, however, in order for faster convergence, we go back to the case of random grids employed in the main text. All results initially coincide to within line thickness and only for longer times the small spacing

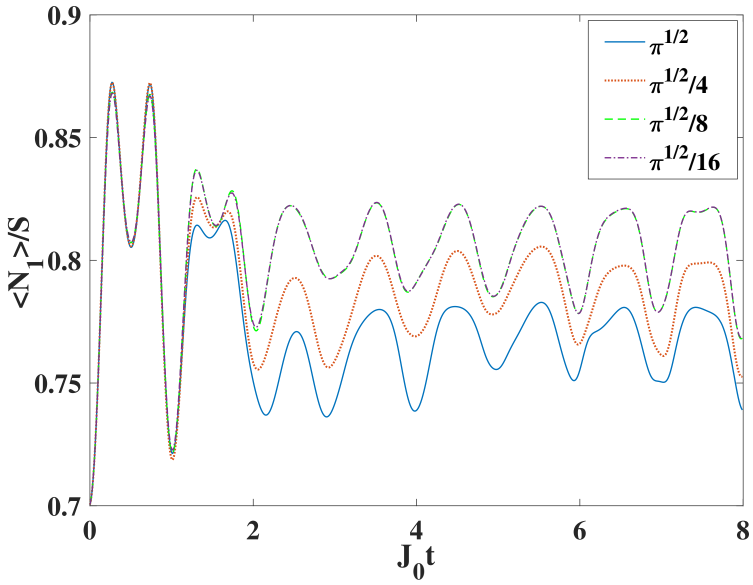

Fig. C.2 The population dynamics of the first mode in the two-mode case with 200 photons. The driving frequency and strength are $\omega = 2\pi/J_0$ and $J_1 = 0.5J_0$, and the on-site interaction energy $U = 0.1J$. The number of GCS is 81. Different lines are results for different spacings of the complex grid: solid: $\sqrt{\pi}$, dotted: $\sqrt{\pi}/4$, dash: $\sqrt{\pi}/8$, dash-dotted: $\sqrt{\pi}/16$.

turns out to be advantageous. Although small spacings make the calculation generally more efficient, decreasing the spacing indefinitely is not an option for improvement and we found an optimum value of $\sqrt{\pi}/32$ in the present case. The even smaller spacing $\sqrt{\pi}/64$ will not lead to a further promotion compared with $\sqrt{\pi}/32$ (the results are even slightly worse). Our final conclusion is that large numbers of photons and modes will increase the dimension of Hilbert space dramatically and make the dynamical process more complicated. As we have shown here, constructing complex grids with optimal spacings (smaller than $\sqrt{\pi}$) can help speeding up the convergence of numerical calculations, and for more complicated systems smaller spacing is needed for feasibility of the calculation, but there is no gain in decreasing the spacing indefinitely.

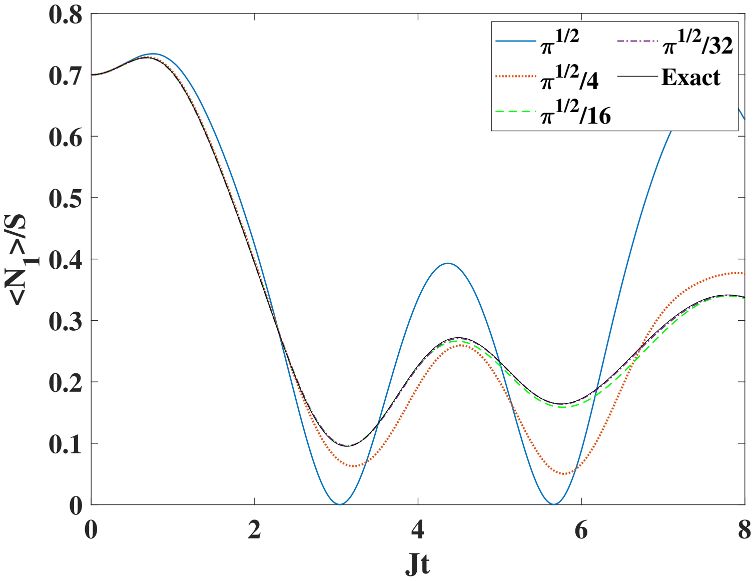

Fig. C.3 The dynamics of the population of the first mode in the four-mode case with 30 photons. The on-site interaction energy $U = 0.1J$. The number of GCSs used is 169. Different lines are results for different spacings of the complex grid: solid: $\sqrt{\pi}$, dotted: $\sqrt{\pi}/4$, dash: $\sqrt{\pi}/16$, dash-dotted: $\sqrt{\pi}/32$. The crosses display the exact results using the full Fock state basis.

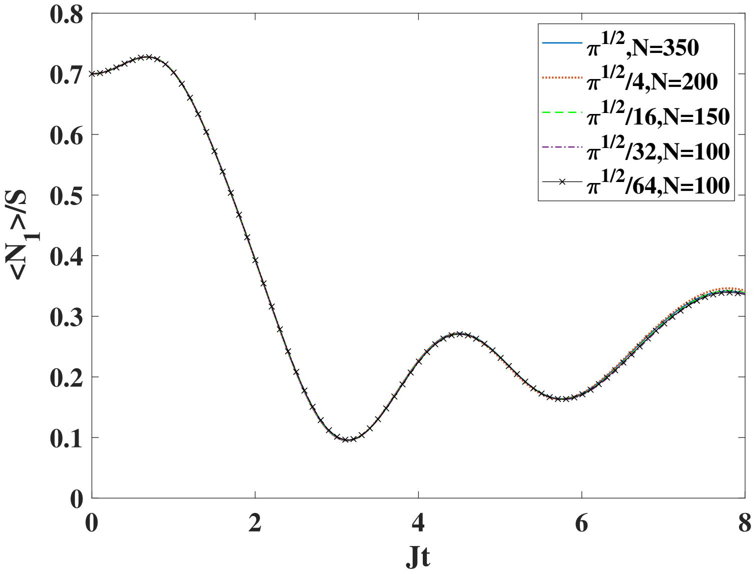

Fig. C.4 Convergence of the population dynamics in the four-mode case with 30 photons for different spacings and basis size N. The on-site interaction energy $U = 0.1J$. The different curves (solid: $\sqrt{\pi}$, dotted: $\sqrt{\pi}/4$, dash: $\sqrt{\pi}/16$, dash-dotted: $\sqrt{\pi}/32$, star: $\sqrt{\pi}/64$, circles: exact Fock results) coincide to within line thickness for most of the time interval shown.

Appendix D

Rederivation of Glynn's formula for the permanent

We verify the output wavefunction of Fock state boson sampling given in Eq. (6.21) by showing that it contains Glynn's formula for the permanent of a square matrix [184]. To this end, we stress that, in order to calculate the permanent of the unitary matrix $\mathbf{U}$, we can assume the input state to be the special Fock state $|11\cdots 1\rangle$. Then, from Eq. (6.15) the parameters of the GCSs are given by $\vec{\xi}_k = \frac{1}{\sqrt{M}}\vec{x}_k$, where $\vec{x}_k$ is a vector with M entries chosen from the set $\{-1,+1\}$, except for $k=1$, where the vector entries are fixed to be $+1$, and the corresponding amplitude from Eq. (6.14) is given by

$$A_k = \frac{M^{\frac{M}{2}}}{2^{M-1}\sqrt{M!}} \prod_{i=1}^{M} x_{ki}. \tag{D.1}$$

So the output state under the unitary transformation is (presently $S=M$)

$$|\Psi\rangle_{\text{out}} = \frac{M^{\frac{M}{2}}}{2^{M-1}\sqrt{M!}} \sum_{k=1}^{2^{M-1}} \left(\prod_{i=1}^{M} x_{ki}\right) \left| M, \frac{1}{\sqrt{M}}\vec{x}_k\cdot\vec{U}_1, \frac{1}{\sqrt{M}}\vec{x}_k\cdot\vec{U}_2, \cdots, \frac{1}{\sqrt{M}}\vec{x}_k\cdot\vec{U}_M \right\rangle, \tag{D.2}$$

where $\vec{U}_j$ denotes the j-th column of the matrix $\mathbf{U}$. The permanent of the unitary matrix can then be obtained by projecting the output state onto the Fock state $\langle 11\cdots 1|$, yielding

$$\begin{aligned} \text{per}(\mathbf{U}) &= \langle 11\cdots 1|\Psi\rangle_{\text{out}} \\ &= \frac{1}{2^{M-1}} \sum_{k=1}^{2^{M-1}} \left[\left(\prod_{i=1}^{M} x_{ki}\right) \prod_{m=1}^{M} \vec{x}_k\cdot\vec{U}_m \right], \end{aligned} \tag{D.3}$$

where we have used the multinomial theorem and the fact that only terms with unit powers of $a_i^\dagger$ do survive the projection. The resulting formula thus is Glynn's formula for the permanent of a square matrix [186, 201].

Our analytical manipulations based on Kan's formula for the expansion of a Fock state in terms of multiple GCS thus lead to an alternative derivation of Glynn's formula, which is considered to be a computational alternative to Ryser's formula [178]. A generalized formula for the permanent has been found along similar lines [202, 203]. Furthermore, it is worthwhile to note that different permanent identities have been proven in a quantum-inspired way in [204]. There the Glynn formula has, e.g., been proven using cat states.

Appendix E

Derivation of the purity in terms of the unitary

For the boson sampling problem, if the initial state is the Fock state $|11\cdots10\cdots0\rangle$, where only the first S modes are occupied by single photons, in close analogy to the rederivation of Glynn's formula in the main text, Kan's formula implies that the values of the amplitudes in the GCS expansion in Eq. (6.11) are $A_k = \frac{1}{\sqrt{S!}}\left(\frac{S}{4}\right)^{\frac{S-1}{2}}\prod_{i=1}^{S}x_{ki}$ where $\vec{x}_k$ is a vector with S entries from the set $\{-1,+1\}$, apart from $k=1$ (see main text), and the values of the GCS parameters are $\vec{\xi}_k = \frac{1}{\sqrt{S}}(x_{k1}, x_{k2}, \cdots, x_{kS}, 0, \cdots, 0)$.
In analogy to the case $S=M$ from Eq. (D.2), the output state after the rotation with the unitary matrix $\mathbf{U}$ is [184]

$$|\psi\rangle_{\text{out}} = \frac{1}{\sqrt{S!}}\left(\frac{S}{4}\right)^{\frac{S-1}{2}}\sum_{k=1}^{2^{S-1}}\left(\prod_{i=1}^{S}x_{ki}\right)\left|S, \frac{1}{\sqrt{S}}\vec{x}_k\vec{\mathscr{U}}_1, \frac{1}{\sqrt{S}}\vec{x}_k\vec{\mathscr{U}}_2, \cdots, \frac{1}{\sqrt{S}}\vec{x}_k\vec{\mathscr{U}}_M\right\rangle, \tag{E.1}$$

where $\vec{\mathscr{U}}_i$ is the truncated vector $\vec{U}_i$ with only the first S entries. Thus, we get (A coefficients are time-independent)

$$A_kA_j^* = \frac{1}{S!}\left(\frac{S}{4}\right)^{S-1}\prod_{i=1}^{S}(x_{ki}x_{ji}), \tag{E.2}$$

as well as

$$\begin{aligned}\langle S-n,\vec{\xi}_{j\tilde{L}}|S-n,\vec{\xi}_{k'\tilde{L}}\rangle_{\text{out}} &= (\vec{\xi}_{k'\tilde{L}}\vec{\xi}^{\dagger}_{j\tilde{L}})^{S-n}\\ &= \left[\frac{1}{\sqrt{S}}\vec{x}_{k'}\cdot(\vec{\mathscr{U}}_1,\vec{\mathscr{U}}_2,\cdots,\vec{\mathscr{U}}_{M_L})\cdot\frac{1}{\sqrt{S}}(\vec{\mathscr{U}}_1,\vec{\mathscr{U}}_2,\cdots,\vec{\mathscr{U}}_{M_L})^{\dagger}\cdot\vec{x}_j^T\right]^{S-n}\\ &= \frac{1}{S^{S-n}}(\vec{x}_{k'}\Lambda_L\vec{x}_j^T)^{S-n} \qquad \text{(E.3)}\end{aligned}$$

and

$$\begin{aligned}\langle n,\vec{\xi}_{j\tilde{R}}|n,\vec{\xi}_{k\tilde{R}}\rangle_{\text{out}} &= (\vec{\xi}_{k\tilde{R}}\vec{\xi}^{\dagger}_{j\tilde{R}})^{n}\\ &= \left[\frac{1}{\sqrt{S}}\vec{x}_{k}\cdot(\vec{\mathscr{U}}_{M_L+1},\vec{\mathscr{U}}_{M_L+2},\cdots,\vec{\mathscr{U}}_{M})\cdot\frac{1}{\sqrt{S}}(\vec{\mathscr{U}}_{M_L+1},\vec{\mathscr{U}}_{M_L+2},\cdots,\vec{\mathscr{U}}_{M})^{\dagger}\cdot\vec{x}_j^T\right]^{n}\\ &= \frac{1}{S^{n}}(\vec{x}_{k}\Lambda_R\vec{x}_j^T)^{n} \qquad \text{(E.4)}\end{aligned}$$

for the ingredients of Eq. (6.29). Here the Hermitian matrices $\Lambda_{L/R}$ are defined as

$$\Lambda_L = (\vec{\mathscr{U}}_1,\vec{\mathscr{U}}_2,\cdots,\vec{\mathscr{U}}_{M_L})\cdot(\vec{\mathscr{U}}_1,\vec{\mathscr{U}}_2,\cdots,\vec{\mathscr{U}}_{M_L})^{\dagger}, \qquad \text{(E.5)}$$

$$\Lambda_R = (\vec{\mathscr{U}}_{M_L+1},\vec{\mathscr{U}}_{M_L+2},\cdots,\vec{\mathscr{U}}_{M})\cdot(\vec{\mathscr{U}}_{M_L+1},\vec{\mathscr{U}}_{M_L+2},\cdots,\vec{\mathscr{U}}_{M})^{\dagger}. \qquad \text{(E.6)}$$

This leads to the final result

$$\begin{aligned}\mathrm{Tr}(\boldsymbol{\rho}_L^2) = \left(\frac{1}{2}\right)^{4(S-1)}&\sum_{n=0}^{S}\frac{1}{[(S-n)!n!]^2}\\ &\sum_{k,j,k',j'=1}^{2^{S-1}}\prod_{i=1}^{S}(x_{ki}x_{ji}x_{k'i}x_{j'i})(\vec{x}_{k'}\Lambda_L\vec{x}_j^T\vec{x}_k\Lambda_L\vec{x}_{j'}^T)^{S-n}(\vec{x}_k\Lambda_R\vec{x}_j^T\vec{x}_{k'}\Lambda_R\vec{x}_{j'}^T)^n \qquad \text{(E.7)}\end{aligned}$$

for the purity.

References

[1] P. Anderson. More is different: Broken symmetry and the nature of the hierarchical structure of science. *Science*, **177**:393–396, 1972.

[2] J. Orenstein and A. Millis. Advances in the physics of high-temperature superconductivity. *Science*, **288**:468–474, 2000.

[3] X. Qi and S. Zhang. Topological insulators and superconductors. *Rev. Mod. Phys.*, **83**:1057–1110, 2011.

[4] B. Yan and S. Zhang. Topological materials. *Rep. Prog. Phys.*, **75**:096501, 2012.

[5] M. Schreiber, S. Hodgman, P. Bordia, H. Lüschen, M. Fischer, R. Vosk, E. Altman, U. Schneider, and I. Bloch. Observation of many-body localization of interacting fermions in a quasirandom optical lattice. *Science*, **349**:842–845, 2015.

[6] J. Choi, S. Hild, J. Zeiher, P. Schauß, A. Rubio-Abadal, T. Yefsah, V. Khemani, D. Huse, I. Bloch, and C. Gross. Exploring the many-body localization transition in two dimensions. *Science*, **352**:1547–1552, 2016.

[7] J. Smith, A. Lee, P. Richerme, B. Neyenhuis, P. Hess, P. Hauke, M. Heyl, D. Huse, and C. Monroe. Many-body localization in a quantum simulator with programmable random disorder. *Nat. Phys.*, **12**:907–911, 2016.

[8] I. Bloch, J. Dalibard, and W. Zwerger. Many-body physics with ultracold gases. *Rev. Mod. Phys.*, **80**:885–964, 2008.

[9] C. Gross and I. Bloch. Quantum simulations with ultracold atoms in optical lattices. *Science*, **357**:995–1001, 2017.

[10] S. Boixo, S. Isakov, V. Smelyanskiy, R. Babbush, N. Ding, Z. Jiang, M. Bremner, J. Martinis, and H. Neven. Characterizing quantum supremacy in near-term devices. *Nat. Phys.*, **14**:595–600, 2018.

[11] J. Eisert, M. Cramer, and M. Plenio. Colloquium: Area laws for the entanglement entropy. *Rev. Mod. Phys.*, **82**:277–306, 2010.

[12] H. Bruus and K. Flensberg. *Many-body quantum theory in condensed matter physics: an introduction*. OUP Oxford, 2004.

[13] A. Wietek and A. Läuchli. Sublattice coding algorithm and distributed memory parallelization for large-scale exact diagonalizations of quantum many-body systems. *Phys. Rev. E.*, **98**:033309, 2018.

[14] W. Foulkes, L. Mitas, R. Needs, and G. Rajagopal. Quantum monte carlo simulations of solids. *Rev. Mod. Phys.*, **73**:33, 2001.

[15] S. White. Density matrix formulation for quantum renormalization groups. *Phys. Rev. Lett.*, **69**:2863, 1992.

[16] U. Schollwöck. The density-matrix renormalization group in the age of matrix product states. *Ann. Phys.*, **326**:96–192, 2011.

[17] J. Eisert. Entanglement and tensor network states. *arXiv preprint arXiv:1308.3318*, 2013.

[18] M. Vojta. Quantum phase transitions. *Rep. Prog. Phys.*, **66**:2069, 2003.

[19] A. Pelissetto and E. Vicari. Critical phenomena and renormalization-group theory. *Phys. Rep.*, **368**:549–727, 2002.

[20] A. Polkovnikov, K. Sengupta, A. Silva, and M. Vengalattore. Colloquium: Nonequilibrium dynamics of closed interacting quantum systems. *Rev. Mod. Phys.*, **83**:863, 2011.

[21] I. Georgescu, S. Ashhab, and F. Nori. Quantum simulation. *Rev. Mod. Phys.*, **86**:153, 2014.

[22] E. Heller. Time-dependent approach to semiclassical dynamics. *J. Chem. Phys.*, **62**:1544–1555, 1975.

[23] E. Heller. Frozen gaussians: A very simple semiclassical approximation. *J. Chem. Phys.*, **75**:2923–2931, 1981.

[24] M. Herman and E. Kluk. A semiclasical justification for the use of non-spreading wavepackets in dynamics calculations. *Chem. Phys.*, **91**:27–34, 1984.

[25] J. Frenkel et al. *Wave mechanics, advanced general theory*, volume **436**. Oxford, 1934.

[26] A. McLachlan. A variational solution of the time-dependent schrodinger equation. *Mol. Phys.*, **8**:39–44, 1964.

[27] P. Kramer and M. Saraceno. Geometry of the time-dependent variational principle in quantum mechanics. In *Group Theoretical Methods in Physics: Proceedings of the IX International Colloquium Held at Cocoyoc, México, June 23–27, 1980*, pages 112–121. Springer, 2005.

[28] G. Richings, I. Polyak, K. Spinlove, G. Worth, I. Burghardt, and B. Lasorne. Quantum dynamics simulations using gaussian wavepackets: the vmcg method. *Int. Rev. Phys. Chem.*, **34**:269–308, 2015.

[29] D. Shalashilin and M. Child. The phase space ccs approach to quantum and semiclassical molecular dynamics for high-dimensional systems. *Chem. Phys.*, **304**:103–120, 2004.

[30] D. Shalashilin and M. Child. Basis set sampling in the method of coupled coherent states: Coherent state swarms, trains, and pancakes. *J. Chem. Phys.*, **128**, 2008.

[31] P. Buonsante and V. Penna. Some remarks on the coherent-state variational approach to nonlinear boson models. *J. Phys. A: Math. Theor.*, **41**:175301, 2008.

[32] F. Trimborn, D. Witthaut, and H. Korsch. Beyond mean-field dynamics of small bose-hubbard systems based on the number-conserving phase-space approach. *Phys. Rev. A.*, **79**:013608, 2009.

[33] W. Zhang, D. Feng, and R. Gilmore. Coherent states: Theory and some applications. *Rev. Mod. Phys.*, **62**:867–927, 1990.

[34] M. Greiner, O. Mandel, T. Esslinger, T. Hänsch, and I. Bloch. Quantum phase transition from a superfluid to a mott insulator in a gas of ultracold atoms. *Nature*, **415**, 2002.

[35] R. Glauber. Coherent and incoherent states of the radiation field. *Phys. Rev.*, **131**:2766, 1963.

[36] A. Perelomov. On the completeness of a system of coherent states. *Theor. Math. Phys.*, **6**:156–164, 1971.

[37] V. Bargmann, P. Butera, L. Girardello, and J. Klauder. On the completeness of the coherent states. *Rep. Math. Phys.*, **2**:221–228, 1971.

[38] J. Neumann. *Mathematical Foundations of Quantum Mechanics*. Princeton University Press, Princeton, 1955.

[39] M. Boon and J. Zak. Discrete coherent states on the von Neumann lattice. *Phys. Rev. B.*, **18**:6744–6751, 1978.

[40] W. Ding and K. Yang. Entanglement entropy and mutual information in bose-einstein condensates. *Phys. Rev. A.*, **80**:012329, 2009.

[41] L. Dell'Anna. Entanglement properties and ground-state statistics of free bosons. *Phys. Rev. A.*, **105**:032412, 2022.

[42] I. Bengtsson and K. Życzkowski. *Geometry of quantum states: an introduction to quantum entanglement*. Cambridge university press, 2017.

[43] M. Greiner, O. Mandel, T. Esslinger, T. Hänsch, and I. Bloch. Quantum phase transition from a superfluid to a mott insulator in a gas of ultracold atoms. *Nature*, **415**:39–44, 2002.

[44] M. Greiner, O. Mandel, T. Hänsch, and I. Bloch. Collapse and revival of the matter wave field of a bose–einstein condensate. *Nature*, **419**:51–54, 2002.

[45] J. Schachenmayer, A. Daley, and P. Zoller. Atomic matter-wave revivals with definite atom number in an optical lattice. *Phys. Rev. A.*, **83**:043614, 2011.

[46] M. Lacki and M. Heyl. Dynamical quantum phase transitions in collapse and revival oscillations of a quenched superfluid. *Phys. Rev. B*, **99**:121107, 2019.

[47] H. Wilf. *generatingfunctionology*. CRC press, 2005.

[48] M. Heyl. Dynamical quantum phase transitions: a review. *Rep. Prog. Phys.*, **81**:054001, 2018.

[49] P. Jurcevic, H. Shen, P. Hauke, C. Maier, T. Brydges, C. Hempel, B. Lanyon, M. Heyl, R. Blatt, and C. Roos. Direct observation of dynamical quantum phase transitions in an interacting many-body system. *Phys. Rev. Lett.*, **119**:080501, 2017.

[50] J. Zhang, G. Pagano, P. Hess, A. Kyprianidis, P. Becker, H. Kaplan, A. Gorshkov, Z. Gong, and C. Monroe. Observation of a many-body dynamical phase transition with a 53-qubit quantum simulator. *Nature*, **551**:601–604, 2017.

[51] N. Fläschner, D. Vogel, M. Tarnowski, B. Rem, D. Lühmann, M. Heyl, J. Budich, L. Mathey, K. Sengstock, and C. Weitenberg. Observation of dynamical vortices after quenches in a system with topology. *Nat. Phys.*, **14**:265–268, 2018.

[52] H. Aoki, N. Tsuji, M. Eckstein, M. Kollar, T. Oka, and P. Werner. Nonequilibrium dynamical mean-field theory and its applications. *Rev. Mod. Phys.*, **86**:779–837, 2014.

[53] M. Suzuki. Fractal decomposition of exponential operators with applications to many-body theories and monte carlo simulations. *Phys. Lett. A*, **146**:319–323, 1990.

[54] G. Vidal. Efficient simulation of one-dimensional quantum many-body systems. *Phys. Rev. Lett.*, **93**:040502, 2004.

[55] R. Noack and S. Manmana. Diagonalization-and numerical renormalization-group-based methods for interacting quantum systems. In *AIP Conference Proceedings*, volume **789**, pages 93–163. American Institute of Physics, 2005.

[56] F. Grossmann. A hierarchy of semiclassical approximations based on Gaussian wavepackets. *Comm. At. Mol. Phys.*, **34**:141, 1999.

[57] W. Miller. The semiclassical initial value representation: A potentially practical way for adding quantum effects to classical molecular dynamics simulations. *J. Phys. Chem. A.*, **105**:2942–2955, 2001.

[58] M. Thoss and H. Wang. Semiclassical description of molecular dynamics based on initial-value representation methods. *Annu. Rev. Phys. Chem.*, **55**:299–332, 2004.

[59] K. Kay. Semiclassical initial value treatments of atoms and molecules. *Annu. Rev. Phys. Chem.*, **56**:255–280, 2005.

[60] M. Werther, S. Choudhury, and F. Großmann. Coherent state based solutions of the time-dependent schrödinger equation: hierarchy of approximations to the variational principle. *Int. Rev. Phys. Chem.*, **40**:81–125, 2021.

[61] Y. Zhao. The hierarchy of davydov's ansätze: From guesswork to numerically "exact" many-body wave functions. *J. Chem. Phys.*, **158**, 2023.

[62] D. Shalashilin and M. Child. Multidimensional quantum propagation with the help of coupled coherent states. *J. Chem. Phys.*, **115**:5367–5375, 2001.

[63] K. Lee and U. Fischer. Truncated many body dynamics of interacting bosons: A variational principle with error monitoring. *Int. J. Mod. Phys. B*, **28**:1550021, 2014.

[64] O. Alon, A. Streltsov, and L. Cederbaum. Multiconfigurational time-dependent hartree method for bosons: Many-body dynamics of bosonic systems. *Phys. Rev. A.*, **77**:033613, 2008.

[65] J. Haegeman, J. Cirac, T. Osborne, I. Pižorn, H. Verschelde, and F. Verstraete. Time-dependent variational principle for quantum lattices. *Phys. Rev. Lett.*, **107**:070601, 2011.

[66] J. Haegeman, C. Lubich, I. Oseledets, B. Vandereycken, and F. Verstraete. Unifying time evolution and optimization with matrix product states. *Phys. Rev. B.*, **94**:165116, 2016.

[67] C. Lubich, I. Oseledets, and B. Vandereycken. Time integration of tensor trains. *SIAM J. Numer. Anal.*, **53**:917–941, 2015.

[68] S. Paeckel, T. Köhler, A. Swoboda, S. Manmana, U. Schollwöck, and C. Hubig. Time-evolution methods for matrix-product states. *Ann. Phys.*, **411**:167998, 2019.

[69] L. Wang, Y. Fujihashi, L. Chen, and Y. Zhao. Finite-temperature time-dependent variation with multiple davydov states. *J. Chem. Phys.*, **146**, 2017.

[70] M. Werther and F. Grossmann. Apoptosis of moving, non-orthogonal basis functions in many-particle quantum dynamics. *Phys. Rev. B.*, **101**:174315, 2020.

[71] M. Werther and F. Grossmann. Stabilization of adiabatic population transfer by strong coupling to a phonon bath. *Phys. Rev. A*, **102**:063710, 2020.

[72] I. Burghardt, H. Meyer, and L. Cederbaum. Approaches to the approximate treatment of complex molecular systems by the multiconfiguration time-dependent hartree method. *J. Chem. Phys.*, **111**:2927–2939, 1999.

[73] G. Worth and I. Burghardt. Full quantum mechanical molecular dynamics using gaussian wavepackets. *Chem. Phys. letters*, **368**:502–508, 2003.

[74] G. Worth, M. Robb, and I. Burghardt. A novel algorithm for non-adiabatic direct dynamics using variational gaussian wavepackets. *Faraday discussions*, **127**:307–323, 2004.

[75] B. Lasorne, M. Robb, and G. Worth. Direct quantum dynamics using variational multi-configuration gaussian wavepackets. implementation details and test case. *Phys. Chem. Chem. Phys.*, **9**:3210–3227, 2007.

[76] I. Burghardt, K. Giri, and G. Worth. Multimode quantum dynamics using gaussian wavepackets: The gaussian-based multiconfiguration time-dependent hartree (g-mctdh) method applied to the absorption spectrum of pyrazine. *J. Chem. Phys.*, **129**, 2008.

[77] D. Shalashilin and M. Child. Time dependent quantum propagation in phase space. *J. Chem. Phys.*, **113**:10028–10036, 2000.

[78] D. Shalashilin and M. Child. Description of tunneling with the help of coupled frozen gaussians. *J. Chem. Phys.*, **114**:9296–9304, 2001.

[79] M. Child and D. Shalashilin. Locally coupled coherent states and herman–kluk dynamics. *J. Chem. Phys.*, **118**:2061–2071, 2003.

[80] J. Green and D. Shalashilin. Simulation of the quantum dynamics of indistinguishable bosons with the method of coupled coherent states. *Phys. Rev. A.*, **100**:013607, 2019.

[81] S. Rau, J. Main, and G. Wunner. Variational methods with coupled gaussian functions for bose-einstein condensates with long-range interactions. i. general concept. *Phys. Rev. A.*, **82**:023610, 2010.

[82] S. Rau, J. Main, H. Cartarius, P. Köberle, and G. Wunner. Variational methods with coupled gaussian functions for bose-einstein condensates with long-range interactions. ii. applications. *Phys. Rev. A.*, **82**:023611, 2010.

[83] A. Polkovnikov, S. Sachdev, and S. Girvin. Nonequilibrium gross-pitaevskii dynamics of boson lattice models. *Phys. Rev. A.*, **66**:053607, 2002.

[84] C. Brif and A. Mann. A general theory of phase-space quasiprobability distributions. *J. Phys. A: Math. Gen.*, **31**:L9–L17, 1998.

[85] C. Brif and A. Mann. Phase-space formulation of quantum mechanics and quantum-state reconstruction for physical systems with lie-group symmetries. *Phys. Rev. A.*, **59**:971–987, 1999.

[86] F. Trimborn, D. Witthaut, and H. Korsch. Exact number-conserving phase-space dynamics of the *m*-site bose-hubbard model. *Phys. Rev. A.*, **77**:043631, 2008.

[87] C. Gardiner and P. Zoller. *Quantum Noise: A Handbook of Markovian and Non-Markovian Quantum Stochastic Methods with Applications to Quantum Optics*. Springer-Verlag, Berlin, 3rd edition, 2004.

[88] F. Arecchi, E. Courtens, R. Gilmore, and H. Thomas. Atomic coherent states in quantum optics. *Phys. Rev. A.*, **6**:2211–2237, 1972.

[89] A. Klimov, J. Romero, and H. de Guise. GeneralizedSU(2) covariant Wigner functions and some of their applications. *J. Phys. A: Math. Theor.*, **50**:323001, 2017.

[90] K. Merkel, V. Link, K. Luoma, and W. Strunz. Phase space theory for open quantum systems with local and collective dissipative processes. *J. Phys. A: Math. Theor.*, **54**:035303, 2020.

[91] D. Jaksch, C. Bruder, J. Cirac, C. Gardiner, and P. Zoller. Cold bosonic atoms in optical lattices. *Phys. Rev. Lett.*, **81**:3108–3111, 1998.

[92] K. Sakmann, A. Streltsov, O. Alon, and L. Cederbaum. Quantum dynamics of attractive versus repulsive bosonic josephson junctions: Bose-hubbard and full-hamiltonian results. *Phys. Rev. A.*, **82**:013620, 2010.

[93] D. Jaksch, C. Bruder, J. Cirac, C. Gardiner, and P. Zoller. Cold bosonic atoms in optical lattices. *Phys. Rev. Lett.*, **81**:3108–3111, 1998.

[94] M. Lewenstein, A. Sanpera, V. Ahufinger, B. Damski, A. Sen, and U. Sen. Ultracold atomic gases in optical lattices: mimicking condensed matter physics and beyond. *Adv. Phys.*, **56**:243–379, 2007.

[95] C. Chin, R. Grimm, P. Julienne, and E. Tiesinga. Feshbach resonances in ultracold gases. *Rev. Mod. Phys.*, **82**:1225–1286, 2010.

[96] J. Sherson, C. Weitenberg, M. Endres, M. Cheneau, I. Bloch, and S. Kuhr. Single-atom-resolved fluorescence imaging of an atomic mott insulator. *Nature*, **467**:68–72, 2010.

[97] W. Bakr, A. Peng, M. Tai, R. Ma, J. Simon, J. Gillen, S. Foelling, L. Pollet, and M. Greiner. Probing the superfluid–to–mott insulator transition at the single-atom level. *Science*, **329**:547–550, 2010.

[98] A. Abadal. *Probing Quantum Thermalization and Localization in Bose-Hubbard Systems*. PhD thesis, Ludwig-Maximilians-Universität München, 2020.

[99] H. Zhai. *Ultracold Atomic Physics*. Cambridge University Press, 2021.

[100] M. Fisher, P. Weichman, G. Grinstein, and D. Fisher. Boson localization and the superfluid-insulator transition. *Phys. Rev. B.*, **40**:546, 1989.

[101] A. Sanpera, M. Lewenstein, V. Ahufinger, B. Damski, A. De, and U. Sen. Ultracold atomic gases in optical lattices: Mimicking condensed matter physics and beyond. *Adv. Phys.*, **56**:243, 2007.

[102] I. Bloch, J. Dalibard, and S. Nascimbene. Quantum simulations with ultracold quantum gases. *Nat. Phys.*, **8**:267–276, 2012.

[103] S. Trotzky, Y. Chen, A. Flesch, I. McCulloch, U. Schollwöck, J. Eisert, and I. Bloch. Probing the relaxation towards equilibrium in an isolated strongly correlated one-dimensional bose gas. *Nat. Phys.*, **8**:325–330, 2012.

[104] Y. Qiao and F. Grossmann. Exact variational dynamics of the multimode Bose-Hubbard model based on SU(M) coherent states. *Phys. Rev. A.*, **103**:042209, 2021.

[105] S. Habershon. Linear dependence and energy conservation in gaussian wavepacket basis sets. *J. Chem. Phys.*, **136**, 2012.

[106] L. Hackl, T. Guaita, T. Shi, J. Haegeman, E. Demler, and I. Cirac. Geometry of variational methods: dynamics of closed quantum systems. *SciPost Phys.*, **9**:048, 2020.

[107] D. Hennig and G. Tsironis. Wave transmission in nonlinear lattices. *Phys. Rep.*, **307**:333–432, 1999.

[108] K. Rasmussen, T. Cretegny, P. Kevrekidis, and N. Grønbech-Jensen. Statistical mechanics of a discrete nonlinear system. *Phys. Rev. Lett.*, **84**:3740, 2000.

[109] A. Trombettoni and A. Smerzi. Discrete solitons and breathers with dilute bose-einstein condensates. *Phys. Rev. Lett.*, **86**:2353, 2001.

[110] M. Werther. *The multi Davydov-Ansatz: Apoptosis of moving Gaussian basis functions with applications to open quantum system dynamics*. PhD thesis, Technische Universität Dresden, 2020.

[111] S. Tomsovic, P. Schlagheck, D. Ullmo, J. Urbina, and K. Richter. Post-ehrenfest many-body quantum interferences in ultracold atoms far out of equilibrium. *Phys. Rev. A.*, **97**:061606, 2018.

[112] C. Lee, T. Alexander, and Y. Kivshar. Melting of discrete vortices via quantum fluctuations. *Phys. Rev. Lett.*, **97**:180408, 2006.

[113] G. Arwas, A. Vardi, and D. Cohen. Triangular bose-hubbard trimer as a minimal model for a superfluid circuit. *Phys. Rev. A.*, **89**:013601, 2014.

[114] K. Nemoto, C. Holmes, G. Milburn, and W. Munro. Quantum dynamics of three coupled atomic bose-einstein condensates. *Phys. Rev. A.*, **63**:013604, 2000.

[115] R. Franzosi and V. Penna. Self-trapping mechanisms in the dynamics of three coupled bose-einstein condensates. *Phys. Rev. A.*, **65**:013601, 2001.

[116] L. Simon and W. Strunz. Time-dependent semiclassics for ultracold bosons. *Phys. Rev. A.*, **89**:052112, 2014.

[117] C. Khripkov, D. Cohen, and A. Vardi. Coherence dynamics of kicked bose-hubbard dimers: Interferometric signatures of chaos. *Phys. Rev. E.*, **87**:012910, 2013.

[118] G. Milburn, J. Corney, E. Wright, and D. Walls. Quantum dynamics of an atomic bose-einstein condensate in a double-well potential. *Phys. Rev. A.*, **55**:4318–4324, 1997.

[119] G. Santos, A. Tonel, A. Foerster, and J. Links. Classical and quantum dynamics of a model for atomic-molecular bose-einstein condensates. *Phys. Rev. A.*, **73**:023609, 2006.

[120] J. Javanainen. Nonlinearity from quantum mechanics: Dynamically unstable bose-einstein condensate in a double-well trap. *Phys. Rev. A.*, **81**:051602(R), 2010.

[121] K. Furutani, J. Tempere, and L. Salasnich. Quantum effective action for the bosonic josephson junction. *Phys. Rev. B.*, **105**:134510, 2022.

[122] M. Chuchem, K. Smith-Mannschott, M. Hiller, T. Kottos, A. Vardi, and D. Cohen. Quantum dynamics in the bosonic josephson junction. *Phys. Rev. A.*, **82**:053617, 2010.

[123] M. Herman and E. Kluk. A semiclassical justification for the use of non-spreading wavepackets in dynamics calculations. *Chem. Phys.*, **91**:27, 1984.

[124] P. Schlagheck, D. Ullmo, G. Lando, and S. Tomsovic. Resurgent revivals in bosonic quantum gases: A striking signature of many-body quantum interferences. *Phys. Rev. A.*, **106**:L051302, 2022.

[125] S. Ray, P. Ostmann, L. Simon, F. Grossmann, and W. Strunz. Dynamics of interacting bosons using the Herman-Kluk semiclassical initial value representation. *J. Phys. A*, **49**:165303, 2016.

[126] S. Wüster, B. Dabrowska-Wüster, and M. Davis. Macroscopic quantum self-trapping in dynamical tunneling. *Phys. Rev. Lett.*, **109**:080401, 2012.

[127] S. Wimberger, G. Manganelli, A. Brollo, and L. Salasnich. Finite-size effects in a bosonic josephson junction. *Phys. Rev. A.*, **103**:023326, 2021.

[128] M. Albiez, R. Gati, J. Fölling, S. Hunsmann, M. Cristiani, and M. Oberthaler. Direct observation of tunneling and nonlinear self-trapping in a single bosonic josephson junction. *Phys. Rev. Lett.*, **95**:010402, 2005.

[129] A. Leggett. Bose-einstein condensation in the alkali gases: Some fundamental concepts. *Rev. Mod. Phys.*, **73**:307–356, 2001.

[130] B. Josephson. Possible new effects in superconductive tunnelling. *Phys. Lett.*, **1**:251–253, 1962.

[131] A. Smerzi, S. Fantoni, S. Giovanazzi, and S. Shenoy. Quantum coherent atomic tunneling between two trapped bose-einstein condensates. *Phys. Rev. Lett.*, **79**:4950–4953, 1997.

[132] I. Bloch, J. Dalibard, and W. Zwerger. Many-body physics with ultracold gases. *Rev. Mod. Phys.*, **80**:885–964, 2008.

[133] M. Lewenstein, A. Sanpera, and V. Ahufinger. *Ultracold Atoms in Optical Lattices: Simulating quantum many-body systems*. OUP Oxford, 2012.

[134] M. Göppert-Mayer. Über elementarakte mit zwei quantensprüngen. *Ann. Phys.*, **401**:273–294, 1931.

[135] S. Wimberger. *Nonlinear dynamics and quantum chaos*, volume **10**. Springer, 2014.

[136] Y. Qiao and F. Grossmann. Revealing quantum effects in bosonic josephson junctions: a multi-configuration atomic coherent state approach. *Front. Phys.*, **11**, 2023.

[137] G. Mazzarella, L. Salasnich, A. Parola, and F. Toigo. Coherence and entanglement in the ground state of a bosonic josephson junction: From macroscopic schrödinger cat states to separable fock states. *Phys. Rev. A.*, **83**:053607, 2011.

[138] G. Nakerst and M. Haque. Chaos in the three-site bose-hubbard model: Classical versus quantum. *Phys. Rev. E.*, **107**:024210, 2023.

[139] V. Arnol'd. *Mathematical methods of classical mechanics*, volume **60**. Springer Science & Business Media, 2013.

[140] S. Tomsovic, P. Schlagheck, D. Ullmo, J. Urbina, and K. Richter. Post-ehrenfest many-body quantum interferences in ultracold atoms far out of equilibrium. *Phys. Rev. A.*, **97**:061606, 2018.

[141] A. Sinatra, C. Lobo, and Y. Castin. The truncated wigner method for bose-condensed gases: limits of validity and applications1. *J. Phys. B: At., Mol. Opt. Phys.*, **35**:3599, 2002.

[142] A. Sinatra, C. Lobo, and Y. Castin. Classical-field method for time dependent bose-einstein condensed gases. *Phys. Rev. Lett.*, **87**:210404, 2001.

[143] M. Hillery, R. O'Connell, M. Scully, and E. Wigner. Distribution functions in physics: Fundamentals. *Phys. Rep.*, **106**:121–167, 1984.

[144] H. Groenewold and H. Groenewold. *On the principles of elementary quantum mechanics*. Springer, 1946.

[145] M. Srednicki. The approach to thermal equilibrium in quantized chaotic systems. *J. Phys. A: Math. Gen.*, **32**:1163, 1999.

[146] L. D'Alessio, Y. Kafri, A. Polkovnikov, and M. Rigol. From quantum chaos and eigenstate thermalization to statistical mechanics and thermodynamics. *Adv. Phys.*, **65**:239–362, 2016.

[147] D. Abanin, E. Altman, I. Bloch, and M. Serbyn. Colloquium: Many-body localization, thermalization, and entanglement. *Rev. Mod. Phys.*, **91**:021001, 2019.

[148] A. Kaufman, M. Tai, A. Lukin, M. Rispoli, R. Schittko, P. Preiss, and M. Greiner. Quantum thermalization through entanglement in an isolated many-body system. *Science*, **353**:794–800, 2016.

[149] M. Ueda. Quantum equilibration, thermalization and prethermalization in ultracold atoms. *Nat. Rev. Phys.*, **2**:669–681, 2020.

[150] T. Mori, T. Ikeda, E. Kaminishi, and M. Ueda. Thermalization and prethermalization in isolated quantum systems: a theoretical overview. *J. Phys. B: At., Mol. Opt. Phys.*, **51**:112001, 2018.

[151] S. Aaronson and A. Arkhipov. The computational complexity of linear optics. In *Proceedings of the forty-third annual ACM symposium on Theory of computing*, pages 333–342, 2011.

[152] B. Gard, K. Motes, J. Olson, P. Rohde, and J. Dowling. An introduction to boson-sampling. In *From atomic to mesoscale: The role of quantum coherence in systems of various complexities*, pages 167–192. World Scientific, 2015.

[153] E. Schrödinger. Die gegenwärtige Situation in der Quantenmechanik. *Die Naturwissenschaften*, **48**:807, 1935.

[154] M. Nielsen and I. Chuang. *Quantum Computation and Quantum Information*. Cambridge University Press, Camdrige, 10th Anniversary edition, 2010.

[155] F. Mintert, A. Carvalho, M. Kuś, and A. Buchleitner. Measures and dynamics of entangled states. *Phys. Rep.*, **415**:207–259, 2005.

[156] P. Buonsante and A. Vezzani. Ground-State Fidelity and Bipartite Entanglement in the Bose-Hubbard Model. *Phys. Rev. Lett.*, **98**:110601, 2007.

[157] H. Huang, W. Bao, and C. Guo. Simulating the dynamics of single photons in boson sampling devices with matrix product states. *Phys. Rev. A.*, **100**:032305, 2019.

[158] S. Gopalakrishnan and A. Lamacraft. Unitary circuits of finite depth and infinite width from quantum channels. *Phys. Rev. B.*, **100**:064309, 2019.

[159] M. Cheng. Entanglement entropy spectrum for bosonic circuit with tensor network state. Master's thesis, Imperial College, London, 2021.

[160] L. Dell'Anna. Entanglement properties and ground-state statistics of free bosons. *Phys. Rev. A.*, **105**:032412, 2022.

[161] M. Tichy. Interference of identical particles from entanglement to boson-sampling. *J. Phys. B: At., Mol. Opt. Phys.*, **47**:103001, 2014.

[162] A. Chakraborty and R. Sensarma. Renyi entropy of interacting thermal bosons in the large-*N* approximation. *Phys. Rev. A.*, **104**:032408, 2021.

[163] A. Lukin, M. Rispoli, R. Schittko, M. Tai, A. Kaufman, S. Choi, V. Khemani, J. Leonard, and M. Greiner. Probing entanglement in a many-body–localized system. *Science*, **364**:256–260, 2019.

[164] G. Vidal. Efficient classical simulation of slightly entangled quantum computations. *Phys. Rev. Lett.*, **91**:147902, 2003.

[165] R. Islam, R. Ma, P. Preiss, M. Tai, A. Lukin, M. Rispoli, and M. Greiner. Measuring entanglement entropy in a quantum many-body system. *Nature*, **528**:77–83, 2015.

[166] R. Kan. From moments of sum to moments of product. *J. Multivar. Anal.*, **99**:542–554, 2008.

[167] P. Shor. Scheme for reducing decoherence in quantum computer memory. *Phys. Rev. A.*, **52**:R2493, 1995.

[168] J. Preskill. Reliable quantum computers. *Proceedings of the Royal Society of London. Series A: Mathematical, Physical and Engineering Sciences*, **454**:385–410, 1998.

[169] A. Kitaev. Quantum computations: algorithms and error correction. *Russian Mathematical Surveys*, **52**:1191, 1997.

[170] D. Aharonov and M. Ben-Or. Fault-tolerant quantum computation with constant error. In *Proceedings of the twenty-ninth annual ACM symposium on Theory of computing*, pages 176–188, 1997.

[171] E. Knill, R. Laflamme, and W. Zurek. Resilient quantum computation. *Science*, **279**:342–345, 1998.

[172] E. Campbell, B. Terhal, and C. Vuillot. Roads towards fault-tolerant universal quantum computation. *Nature*, **549**:172–179, 2017.

[173] L. Valiant. The complexity of computing the permanent. *Theoretical Computer Science*, **8**:189–201, 1979.

[174] H. Zhong, H. Wang, Y. Deng, M. Chen, L. Peng, Y. Luo, J. Qin, D. Wu, X. Ding, Y. Hu, et al. Quantum computational advantage using photons. *Science*, **370**:1460–1463, 2020.

[175] A. Neville, C. Sparrow, R. Clifford, E. Johnston, P. Birchall, A. Montanaro, and A. Laing. Classical boson sampling algorithms with superior performance to near-term experiments. *Nat. Phys.*, **13**:1153, 2017.

[176] D. Brod, E. Galvão, A. Crespi, R. Osellame, N. Spagnolo, and F. Sciarrino. Photonic implementation of boson sampling: a review. *Adv. Photonics.*, **1**:034001, 2019.

[177] S. Scheel. Permanents in linear optical networks, 2004.

[178] H. Ryser. *Combinatorial Mathematics*. The Carus Mathematical Monographs **14**. The Mathematical Association of America, 1963.

[179] H. Kiah, A. Vardy, and H. Yao. Computing permanents on a trellis. *CoRR*, **abs/2107.07377**, 2021.

[180] P. Lundow and K. Markström. Efficient computation of permanents, with applications to boson sampling and random matrices. *J. Comput. Phys.*, **455**:110990, 2022.

[181] X. Ma and W. Rhodes. Multimode squeeze operators and squeezed states. *Phys. Rev. A.*, **41**:4625, 1990.

[182] J. Sakurai. *Modern quantum mechanics*. Addison-Wesley Publishing Company, Reading, 1994.

[183] T. Cubitt. Matlab code. https://www.dr-qubit.org/matlab.html, 2013.

[184] Y. Qiao, J. Huh, and F. Grossmann. Entanglement in the full state vector of boson sampling. *SciPost Phys.*, **15**:007, 2023.

[185] Y. Nakagawa, M. Watanabe, H. Fujita, and S. Sugiura. Universality in volume-law entanglement of scrambled pure quantum states. *Nat. Commun.*, **9**:1635, 2018.

[186] D. Glynn. The permanent of a square matrix. *European Journal of Combinatorics*, **31**:1887–1891, 2010.

[187] C. Beck and F. Schlögl. *Thermodynamics of Chaotic Systems: An Introduction*. Cambridge University Press, Camdrige, 1993.

[188] J. Iosue, A. Ehrenberg, D. Hangleiter, A. Deshpande, and A. Gorshkov. Page curves and typical entanglement in linear optics. 2022.

[189] F. Franchini, A. Its, and V. Korepin. Renyi entropy of the XY spin chain. *J. Phys. A: Math. Theor.*, **41**:025302, 2007.

[190] H. Kwon, A. Paige, and M. Kim. Condition on the Rényi Entanglement Entropy under Stochastic Local Manipulation. *Phys. Rev. Lett.*, **125**:100502, 2020.

[191] A. Daley, H. Pichler, J. Schachenmayer, and P. Zoller. Measuring entanglement growth in quench dynamics of bosons in an optical lattice. *Phys. Rev. Lett.*, **109**:020505, 2012.

[192] D. Page. Average entropy of a subsystem. *Phys. Rev. Lett.*, **71**:1291–1294, 1993.

[193] C. Oh, K. Noh, B. Fefferman, and L. Jiang. Classical simulation of lossy boson sampling using matrix product operators. *Phys. Rev. A.*, **104**:022407, 2021.

[194] H. Li and F. Haldane. Entanglement Spectrum as a Generalization of Entanglement Entropy: Identification of Topological Order in Non-Abelian Fractional Quantum Hall Effect States. *Phys. Rev. Lett.*, **101**:010504, 2008.

[195] M. Regemortel, O. Shtanko, L. García-Pintos, A. Deshpande, H. Dehghani, A. Gorshkov, and M. Hafezi. Monitoring-induced entanglement entropy and sampling complexity. *Phys. Rev. Research*, **4**:L032021, 2022.

[196] S. Stanisic, N. Linden, A. Montanaro, and P. Turner. Generating entanglement with linear optics. *Phys. Rev. A.*, **96**:043861, 2017.

[197] H. Kim and D. Huse. Ballistic spreading of entanglement in a diffusive nonintegrable system. *Phys. Rev. Lett.*, **111**:127205, 2013.

[198] T. Padmanabhan. Thermodynamical aspects of gravity: new insights. *Rep. Prog. Phys.*, **73**:046901, 2010.

[199] J. Broeckhove, L. Lathouwers, E. Kesteloot, and P. Leuven. On the equivalence of time-dependent variational principles. *Chem. Phys. letters*, **149**:547–550, 1988.

[200] M. Werther. *The multi Davydov-Ansatz. Apoptosis of moving Gaussian basis functions with applications to open quantum system dynamics.* PhD thesis, Technische Universität Dresden, 2020.

[201] J. Huh. A fast quantum algorithm for computing matrix permanent. *arXiv preprint arXiv:2205.01328*, 2022.

[202] S. Chin and J. Huh. Generalized concurrence in boson sampling. *Sci. Rep.*, **8**:1–9, 2018.

[203] M. Yung, X. Gao, and J. Huh. Universal bound on sampling bosons in linear optics and its computational implications. *Nat. Sci. Rev.*, **6**:719–729, 2019.

[204] U. Chabaud, A. Deshpande, and S. Mehraban. Quantum-inspired permanent identities. *Quantum*, **6**:877, 2022.

I would like to express my sincere gratitude to the Center for Information Services and High Performance Computing in TU Dresden for providing the valuable computing resources that were crucial in completing the numerical calculations of my research.

List of publications

1. Y. Qiao and F. Grossmann. *Exact variational dynamics of the multimode Bose- Hubbard model based on SU(M) coherent states*. Phys. Rev. A., **103**: 042209, 2021.

2. Y. Qiao, J. Huh, and F. Grossmann. *Entanglement in the full state vector of boson sampling*. SciPost Phys., **15**: 007, 2023.

3. Y. Qiao and F. Grossmann. *Revealing quantum effects in bosonic josephson junctions: a multi-configuration atomic coherent state approach*. Front. Phys., **11**: 1221614, 2023

Acknowledgements

First and foremost, I would like to express my deepest gratitude to my supervisor, Prof. Frank Grossmann. He introduced me to the intriguing world of quantum many-body physics, opening the door to the research I am passionate about. His academic guidance deeply inspired me. The personal care and the warm-heart he has shown is very supportive for me. I am also immensely grateful to Prof. Walter Strunz for his essential financial support during the latter part of my Ph.D. program. His selfless support enables me to finish this thesis. I would also like to thank Prof. Jan Budich, Prof. Honghao Tu, and Prof. Arnd Bäcker in Dresden University of Technology for their insightful physics lectures that significantly expanded my understanding of various subjects.

My sincere appreciation goes to the Max Planck Institute for the Physics of Complex Systems for the financial backing during my Ph.D. This support was crucial for my focus on my research. Special thanks to Dr. Paul McClarty and Dr. Panos Giannakeas, the coordinators at the institute, for organizing valuable seminars and summer schools. These events provided an excellent platform for all the Ph.D. students. Dr. Paul McClarty was particularly helpful with my initial German visa application, and Dr. Panos Giannakeas offered an outstanding lecture on cold atom physics.

I also want to thank my colleagues and collaborators. Dr. Michael Werther, although he had already graduated when I arrived in Germany, was instrumental in helping me when I was new to the field. Working with Dr. Sreeja Choudhury, a colleague and friend, for two years was a pleasure, and she introduced me to the delights of Indian cuisine. My collaboration with Prof. Joonsuk Huh was a significant part of my Ph.D. research, and discussions with Dr. Gabriel Lando led to many rewarding outcomes. My thanks also go to many other colleagues who offered substantial help both in my personal and professional life during my Ph.D.

Lastly, I am eternally grateful to my family for their understanding and support while I was pursuing my Ph.D. abroad. A special mention to my girlfriend Ms. Zheng, whose love and support have been a significant motivation for me.

Once again, thank you to everyone who played a part in this important phase of my life. I will keep all these kindnesses I have encountered in mind and carry them forward to my next journey.

Declaration

Diese Arbeit wurde am Institut für Theoretische Physik der Technischen Universität Dresden unter der wissenschaftlichen Betreuung von Prof. Dr. Frank Großmann durchgeführt. Hiermit versichere ich, dass ich die vorliegende Arbeit ohne unzulässige Hilfe Dritter und ohne Benutzung anderer als der angegebenen Hilfsmittel angefertigt habe; die aus fremden Quellen direkt oder indirekt übernommenen Gedanken sind als solche kenntlich gemacht. Die Arbeit wurde bisher weder im Inland noch im Ausland in gleicher oder ähnlicher Form einer anderen Prüfungsbehörde vorgelegt. Darüber hinaus erkenne ich die Promotionsordnung der Fakultät Mathematik und Naturwissenschaften der Technischen Universität Dresden vom 23. Februar 2011 an.

Yulong Qiao
geboren am 01.08.1994 in Linyi, China
June 2024